12-18-2020

Investigating the Accumulation, Sub-Organ Distribution, And Biochemical Effects of Nanomaterials Using Mass Spectrometry

Kristen Nicole Sikora

Recommended Citation

Sikora, Kristen Nicole, "Investigating the Accumulation, Sub-Organ Distribution, And Biochemical Effects of Nanomaterials Using Mass Spectrometry" (2020). *Doctoral Dissertations*. 2081.
https://doi.org/10.7275/2g5w-rj85 https://scholarworks.umass.edu/dissertations_2/2081

University of Massachusetts Amherst

ScholarWorks@UMass Amherst

Investigating the Accumulation, Sub-Organ Distribution, And Biochemical Effects of Nanomaterials Using Mass Spectrometry

Kristen Nicole Sikora

INVESTIGATING THE ACCUMULATION, SUB-ORGAN DISTRIBUTION, AND BIOCHEMICAL EFFECTS OF NANOMATERIALS USING MASS SPECTROMETRY

A Dissertation Presented

by

KRISTEN NICOLE SIKORA

Submitted to the Graduate School of the

University of Massachusetts Amherst in partial fulfillment

of the requirements for the degree of

DOCTOR OF PHILOSOPHY

SEPTEMBER 2020

Chemistry

INVESTIGATING THE ACCUMULATION, SUB-ORGAN DISTRIBUTION, AND BIOCHEMICAL EFFECTS OF NANOMATERIALS USING MASS SPECTROMETRY

A Dissertation Presented

By

KRISTEN NICOLE SIKORA

Approved as to style and content by:

_____

Richard W. Vachet, Chair

_____

Vincent M. Rotello, Member

_____

Ricardo B. Metz, Member

_____

Professor D. Joseph Jerry, Member

_____

Ricardo B. Metz, Department Head

Department of Chemistry

DEDICATION

To my sister Alli, my mom Cheryl, and my dad Robert for being my greatest support system and giving me everything I have ever needed to achieve my dreams.

ACKNOWLEDGEMENTS

I would like to take the time to express immense gratitude to all the individual people who helped support and guide me on my path to completing this dissertation.

First, I would like to sincerely thank my research advisor, Professor Richard Vachet. I am so grateful for the opportunity I have had to work under his guidance during my graduate career. Richard is an incredibly compassionate leader both in and out of the laboratory. As a research advisor, he is creative, patient, and dedicated to his students' progress. As a mentor, he has always been positive, empathetic, and a true guiding light for his students. Graduate school is filled with many trails and successes, but no matter how small the moment, Richard has always stood behind his students to support them. I aspire to be the kind of leader, scientist, and person that he is. I cannot thank him enough for everything he has done to help me develop into the scientist and person that I am today.

I would like to thank my committee members: Professor Vincent M. Rotello, Professor Ricardo B. Metz, and Professor Joseph Jerry for their many hours of attention, constructive critique, and suggestions during each of my candidacy milestones. I attribute a great deal of my success as a scientist to the feedback and positive encouragement you have each given me over the years. I would also like to thank Professor Stephen Eyles who has helped me in countless ways to progress my dissertation. Whether it was feedback on presentations or troubleshooting my experiments, I am incredibly grateful for the time Steve always made to help me.

 I was lucky enough to work with amazing people in the Vachet laboratory and I cannot thank the members, both past and present, enough for their support. I am so appreciative of the collaborative, engaging, entertaining, and sincerely kind environment that we were

able to cultivate together. I attribute a lot of my success to all of you. I have to give a special thanks to Professor Alyssa Marsico and Professor Sukru Gokhan Elçi for helping to train me and guide me in my early years as a grad student and to Laura Castellanos for helping me immensely advance my projects in my later years. Without them I never would have been able to accomplish as much as I have in my research. I also want to thank Dheeraj Agrohia and Jeerapat "Ping" Doungchawee for being incredibly patient students as I passed my knowledge on to them. I wish the best for both of you continuing this project. I would also like to thank the undergraduate students I had the privilege of mentoring. Liam Jackson, Biidaaban Reinhardt, and Andrea Bucknam all saved me countless hours and headaches by working tirelessly to help me on my projects.

I also need to thank my amazing group of labmates who have come before me: Professor Nick Borotto and Drs. Zhe Zhang, M.A.C. Serrano, Tyler Marcinko, Meizhe Wang, Bo Zhao, and Tianying Liu. Thank you all for welcoming me into the group years ago and always being available for help when needed. I also want to thank Dr. Patanachai (Kong) Limpikirati and Blaise Arden who I have shared many moments of my candidacy milestones with. Thank you both for being such supportive lab and cohort-mates Finally, thank you to the current Vachet lab members: Xiao Pan, Catherine Tremblay, Stacey Nash, Zack Kirsh, and Jack Bell. It has been such a pleasure to work beside you all, and I cannot wait to see what you all accomplish in your own graduate careers.

I would also like to thank the members of the Rotello lab who contributed immensely to my dissertation work. Thank you to Dr. Joseph Hardie who not only provided me with ideas and materials, but truly cared about helping to progress my projects alongside his

own. Yi-Wei "Bill" Lee, Yuanchang Liu, David Luther, thank you all for working many long hours on our shared work. I appreciate all of you immensely.

I would like to thank the Chemistry Biology Interface (CBI) program for mentorship, funding, and many opportunities for scientific and personal growth during my doctoral study. I extend a special thank you to Professor Lynmarie Thompson, without whom the CBI program would not be possible. To the entire Chemistry department staff, including Bob Sabola, Ryan Feyrer, jms, Kay Fenlason, and Chandra Hardy, thank you for making our lives as graduate students so much easier. We would not be able to do any of this without you all.

I was lucky enough to befriend many amazing people during my time at UMass. I thank all of them for their unwavering support. I want to especially thank Dr. Sarah Marques, Dr. Jill Graham, Francesca Anson, Michael Mingroni, and Dr. Keith Lehuta, for their friendship throughout every exciting and challenging moment I have gone through.

I also have an incredible amount of gratitude towards my friends who supported me from afar throughout this entire process. Christina Bryan, I could not have done this without your constant support and generosity. Thank you for always being such a rock in my life. Kate Petty, Ashley Barcikowski, and Jennifer Nogay, thank you all for being so incredibly encouraging through every milestone, and patient with me for the moments I have missed over the years.

Finally, I would like to give the biggest thank-you to my family. My sister, Alli, has been literally and figuratively by my side through every milestone in my life leading up to this point. She is the brightest, strongest, and most compassionate person I know, and I am so lucky to have her as my sister and best friend. My parents, Cheryl and Robert Sikora,

have always been unwaveringly generous and encouraging. They provided me with the plethora of books, movies, and math problems that sparked my interest in science as a child, and also gave me the unconditional love and support to help me grow into the person I am today. I am so proud to be their daughter. I cannot thank the three of you enough for the roles that you have played in my life before and during my doctoral process. I am the person I am today because of all that you have done for me. I dedicate this work to you.

ABSTRACT

INVESTIGATING THE ACCUMULATION, SUB-ORGAN DISTRIBUTION, AND

BIOCHEMICAL EFFECTS OF NANOMATERIALS USING MASS

SPECTROMETRY

SEPTEMBER 2020

KRISTEN NICOLE SIKORA

B.S., UNIVERSITY OF PITTSBURGH

Ph.D., UNIVERSITY OF MASSACHUSETTS AMHERST

Directed by: Professor Richard W. Vachet

Gold nanoparticles (AuNPs) are attractive materials for use in various biomedical applications, such as therapeutic delivery, due to their unique chemical properties and modular tunability. Mass spectrometry methods, including laser desorption/ionization mass spectrometry (LDI-MS) and inductively coupled plasma mass spectrometry (ICP-MS) have been successfully used to evaluate the distribution of AuNPs in complex biological systems. As new AuNP-based materials are developed for applications in therapeutic delivery, it is essential to simultaneously develop analytical techniques that can comprehensively assess their behavior *in vivo*. In this dissertation, novel mass spectrometric methods have been developed and utilized to evaluate the uptake, distribution, and biochemical effects of AuNPs and AuNP-based delivery materials. First, a dual-mode mass spectrometry imaging method was developed to 1) track the distribution of inorganic nanodelivery vehicles containing a deliverable therapeutic and 2) correlate the distribution of the subsequent biochemical effects with the carrier when injected into mice. Next, the correlation of the distribution of the inorganic carrier and biochemical effects

were examined and quantified for specific sub-organ regions of tissues. These predicted changes were further evaluated for their biochemical relevance. Additionally, unexpected biochemical changes were evaluated by injecting mice with nanodelivery vehicles lacking an active therapeutic. Finally, a MS method was developed to quantitatively assess NP uptake into various cell types.

TABLE OF CONTENTS

Page

LIST OF TABLES

LIST OF FIGURES

CHAPTER 1

INTRODUCTION

1.1 Nanomaterials for Biomedical Applications

Scientists are continually striving to synthesize novel compounds to improve human quality of life. One of the greatest efforts in modern science is the development of materials to advance biomedical detection, therapeutic delivery, and disease treatment. Nanotechnology, in particular, has been a prime focus of researchers in these fields due to the attractive chemical properties of nanomaterials such as high surface-to-volume ratios, tailorable core materials, and modular surface properties.[1,2] Over the last few decades, scientist have made great strides in developing a variety of nanomaterials with variable size, shape, morphology, and surface-chemistry tunability.[3,4] Due to the chemical and physical variety of these compounds, nanomaterials provide countless platforms for improving drug delivery,[5–10] molecular detection,[11] imaging,[12–14] sensing,[15] and therapy.[16–18]

Monolayer-protected nanoparticles (NPs) have the benefit of being functionalized with self-assembling monolayers (SAMs). These modular SAMs provide NPs with additional stability, solubility, biocompatibility, and chemical diversity.[1,19–23] There are a variety of NP cores that are used in conjunction with these SAMs for various applications (Table 1.1),[19] however, gold is the most promising in biological applications due to its low toxicity in vitro and in vivo, as well as its strong affinity for ligands containing a thiol group.[24,25] The unique chemical properties allow for gold nanoparticles (AuNPs) to be utilized

Table 1.1. Characteristics, ligands, and exemplary applications of various inorganic and semiconductor materials as nanomaterials. Figure reproduced from reference 19.

Core Material	Characteristics	Ligands	Applications
Au	Optical absorption, Fluorescence and fluorescence quenching, stability	Thiol, disulfide, phosphine, amine	Biomolecular recognition, delivery, sensing
Ag	Surface-enhanced fluorescence	Thiol	Sensing
Pt	Catalytic property	Thiol, phosphine, isocyanide	Bio-catalyst sensing
CdSe	Luminescence, photo-stability	Thiol, phosphine, pyridine	Imaging and sensing
Fe_2O_3	Magnetic property	Diol, dopamine derivative, amine	MR imaging and biomolecule purification
SiO_2	Biocompatibility	Alkoxysilane	Biocompatible by surface coating

successfully in drug delivery, imaging, sensing, and therapeutics. A representation of the AuNPs utilized in this dissertation can be found in Figure 1.1.

1.2 Characterization of Monolayer-Protected Gold Nanoparticles

Monolayer-protected nanomaterials have become ubiquitous in biomedical applications, creating a great need for improved analytical techniques to detect, characterize, track, and quantify them. To ensure efficacy and safety of these materials, the chemical properties of both the NP core and SAMs must be thoroughly evaluated. Atomic force microscopy (AFM),[26] transmission electron microscopy (TEM),[1,27] and scanning tunneling microscopy (STM)[28] are often utilized to confirm NP core size and shape, but they are limited in characterizing the composition of the NP SAMs. X-ray diffraction (XRD)[29] and small angle X-ray scattering (SAXS)[30,31] have also been utilized for
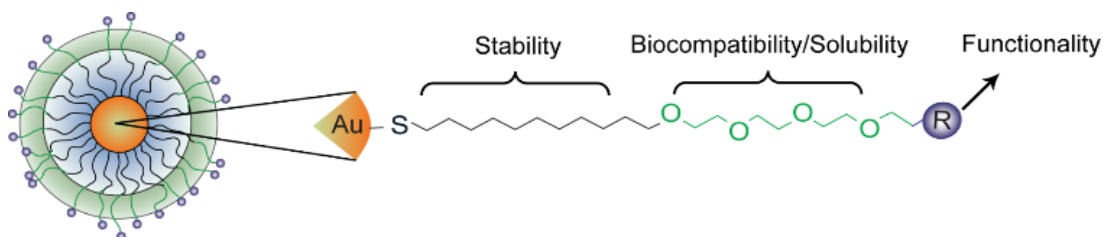
Figure 1.1. AuNP monolayer structure used in this dissertation. The R group represents the tunable portion of the monolayer. Specific structures will be discussed in later chapters. Figure reproduced from reference 19.

characterizing NPs, but there are still limitations to evaluating the SAMs using these techniques.

NMR is commonly utilized for the analysis of AuNP SAMs,[1,32] however, the large sample size required, and potential peak broadening limit this method from being useful for all NPs. Alternatively, UV-Vis[33] and Fourier transform infrared spectroscopy (FT-IR)[34] can be used to obtain some information about the SAMs of NPs, although they cannot readily resolve information for ligands near the NP core due to peak broadening.

1.3 Mass Spectrometric Characterization and Detection of Gold Nanoparticles

Mass spectrometry (MS) is an attractive analytical tool for assessing nanomaterials due to the fact that all materials have an innate mass that can be used as an intrinsic barcode for detection purposes. Utilizing the universality of this technique to characterize NPs has been previously observed through MS methods such as laser desorption/ionization (LDI-MS),[35–41] matrix assisted laser desorption/ionization (MALDI-MSI),[42,43] electrospray ionization (ESI-MS),[44,45] fast atom bombardment (FAB),[46] direct analysis in real time (DART-MS),[47,48] and ion mobility (IM-MS).[49–51] Mass spectrometry has also been utilized to detect and track gold nanoparticles in complex samples such as cells,[37,52,53] plants,[54] and tissue samples.[40,53,55–57]
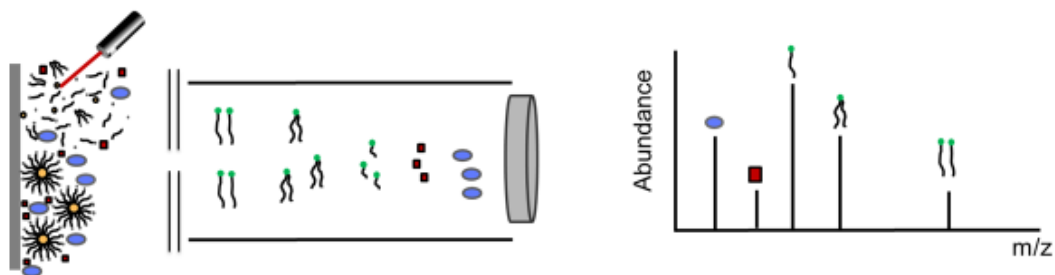
Figure 1.2. Matrix assisted laser desorption/ionization mass spectrometry schematic.

Our group has previously demonstrated the power of using LDI-MSI to obtain the information regarding in-tact AuNP ligands.[55,58–60] In LDI-MS, a laser, with a wavelength typically at 337 or 355 nm, irradiates the sample of interest. For AuNPs, that laser energy is absorbed by the gold core and subsequently transferred to desorb and ionize the surface-bound ligands. It is this process that allows only in-tact AuNP ligands to be observed. Once the ligands are ionized, the analytes are accelerated with the same amount of kinetic energy towards a time-of-flight (TOF) mass analyzer where they are separated based on their velocities. Based on the equation KE=½mv, smaller ions will reach the detector before larger ions. Through this process, m/z values of analytes are determined.[61] A visual representation of this process can be seen in Figure 1.2

The multiplex nature of MS allows for the simultaneous detection of multiple AuNP species in LDI-MS analysis.[37,40,62] This demonstrates the benefits of this method over other detection techniques where only single analytes can be measured at a time. Conversely, inductively coupled plasma mass spectrometry (ICP-MS) has been utilized by our group to obtain elemental information regarding AuNPs in complex biological samples.[40,63,64] In ICP-MS analysis, total elemental composition is measured by digesting the sample of interest into its elemental components. Although specific ligand information is lost, ICP-

MS is extremely sensitive and quantitative and, therefore, allows for the accurate measurement of NP distribution, uptake, and accumulation. LDI-MS and ICP-MS have been used in tandem by our group to obtain information regarding the stability of naomaterials.[40,65,66] By comparing elemental information of the gold from ICP-MS with the in-tact ligand information from LDI-MSI, quantitative measurements regarding AuNP ligand stability can be readily made.

1.4 Mass Spectrometric Imaging of Gold Nanoparticles

The promise of nanomaterials being injected into and circulating within biological systems creates the need to develop analytical tools capable of tracking NPs in site-specific ways. Utilizing imaging techniques is essential for evaluating nanomaterial efficacy as well as biodistribution patterns. Mass spectrometry imaging (MSI) methods provide many benefits over other tools utilized to gain site-specific information regarding nanomaterials. Unlike methods such as fluorescence[67] and radiolabeling,[68] mass spectrometry requires no labels for NP detection. Magnetic resonance imaging (MRI), Raman spectroscopy, and surface plasmon resonance (SPR) have also been previously utilized to monitor NP distributions, however they all have limitations in making quantitative and multiplexed measurements.

MSI provides multiplexed, site-specific information of analytes by generating molecular images from individual mass spectra (Figure 1.3). Both LDI and LA-ICP-MS are capable of providing mas spectrometric images of nanomaterials as our group[40,65,69,70] and others[53,71–73] have previously shown. These imaging techniques work by exploiting the intrinsic chemical properties of the AuNPs, mentioned above, to successfully evaluate the quantitative sub-organ distribution and stability of nanomaterials in tissues. These mass
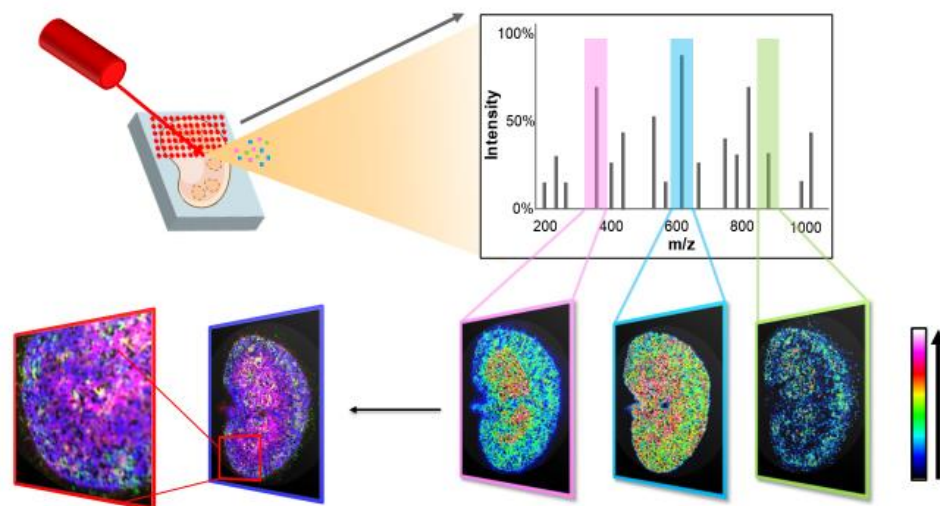
Figure 1.3. Mass spectrometry imaging workflow. From the top left corner: an ionization source is rastered across a sample, producing an individual mass spectrum at each spot. Analytes of interest at specific m/z values can be selected for and molecular images are formed. Each m/z produces an individual image indicating the site-specific information of the analyte which can then be overlaid with other analytes to obtain colocalization information.

spectrometry imaging methods are powerful and comprehensive analytical platforms for the evaluation of AuNPs *in vivo*.

1.5 Mass Spectrometric Imaging of Nanoparticle-Based Delivery Vehicles

Nanoparticle-based delivery vehicles have been a focal point of drug research since the 1960s (Figure 1.4).[74] The development of targeted nano-based drug delivery systems has been shown to vastly improve the efficacy of various therapies based on the ability to control the distribution pattern, dosage, and rate of therapeutic delivery.[74,75] The modular nature of monolayer-protected nanomaterials provides a platform for exponential tunability and control as can be seen in Figure 1.5. This tunability has been exploited for the controlled delivery of therapeutics such as siRNA,[6,76,77] hydrophobic drugs,[78,79] and proteins[80] in vehicles such as liposomes[81,82] and nanoparticle complexes.[6] These particles are promising systems for controlled and efficacious therapeutic delivery, however, due to

6
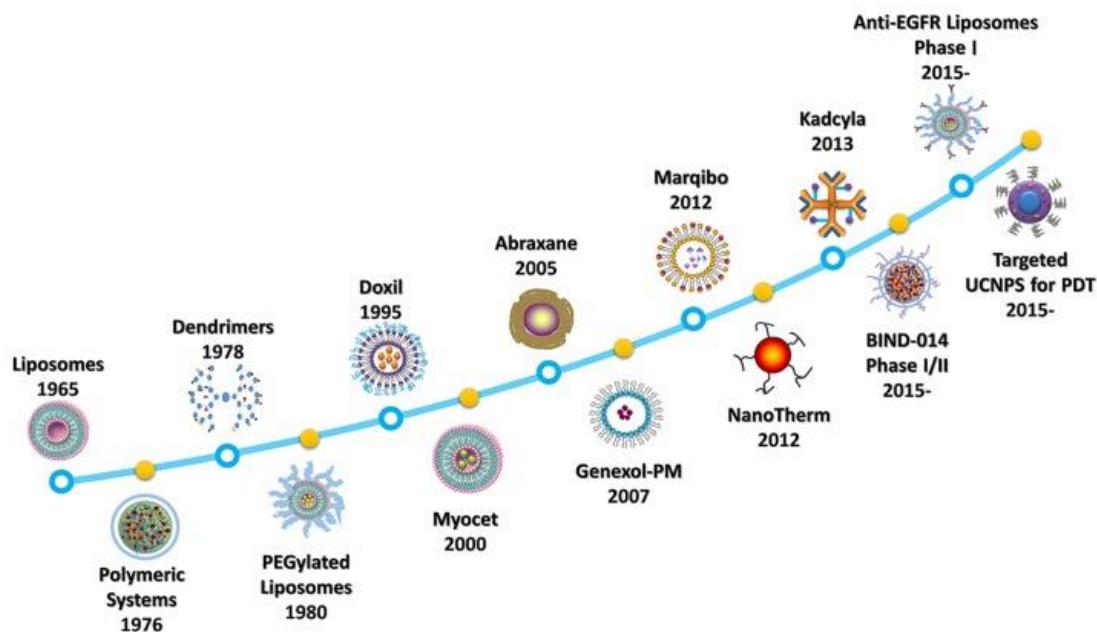
Figure 1.4. The development of nanodelivery vehicles over time. Figure reproduced with permission from reference 71.

their multifaceted nature, it is necessary to develop detection methods that can comprehensively assess where the vehicles accumulate, where the therapeutics function, and where the various working components might generate any unpredicted side-effects.

Tissues are differentiated into sub-organ regions composed of various cell types that play different functional roles in shuttling and processing therapeutics. For instance, the spleen and liver both have distinguishable sub-organ regions involved in the mononuclear phagocyte system which is related to an organism's immune response.[83] Therefore, providing sub-organ spatial distinctions to the accumulation of the delivery vehicles, the effects of the therapeutics, and the unexpected biological impacts is imperative.

Current techniques to evaluate the site-specific information of nanodelivery vehicles most commonly utilize fluorescent microscopy due to its ability to provide accurate spatial resolution of these nanomaterials.[76] However, this method is limited in that the materials need to be intrinsically fluorescent or otherwise modified in order to be tracked by

fluorescence. This method of analysis also is limited in the number of analytes that can be tracked simultaneously. When monitoring the accumulation and biochemical effects of nano-delivery vehicles, utilizing a platform capable of monitoring these sub-organ distributions in a multiplex manner is crucial. Liquid chromatography coupled with mass spectrometry (LC-MS) has been used to monitor the biochemical changes that arise upon the injection of nano-based delivery systems,[84] however, this technique lacks the ability to provide spatial context to these changes.

MSI has been frequently used to evaluate the distributions of many biomedically relevant compounds, including small molecules,[85,86] lipids,[87] drugs and their metabolites,[88] as well as peptides and proteins;[89] however, using these techniques to evaluate complex
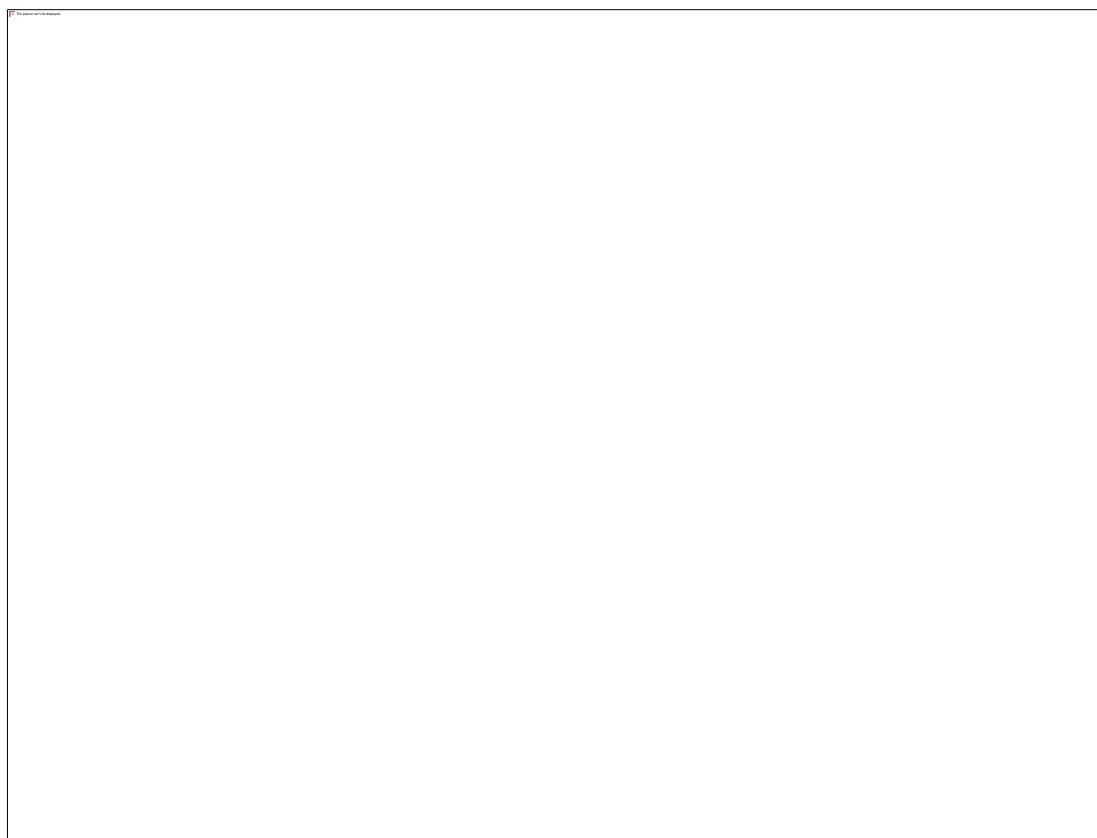
Figure 1.5. Representation of multifunctional nano-based delivery vehicles. Figure reprinted with permission from reference 72.

nanodelivery systems has been limited. MALDI-MSI has been utilized to evaluate liposomal carriers,[90,91] but observations were made solely regarding the cargo delivery, and not the effects of the entire nanodelivery complex. Utilizing our group's previous imaging techniques, we seek to implore MSI to evaluate complex nanodelivery systems *in vivo*. Dual-mode imaging has been previously implored for evaluating combination inorganic and organic therapeutics[92] as well as biological molecules containing inorganic substituents,[93,94] but has yet to be exploited for the evaluation of nanodelivery systems.

MALDI-MSI, unlike LDI and LA-ICP-MS, can be used to evaluate components of nanodelivery vehicles that are not readily ionizable, such as biological molecules. MALDI-MS utilizes the same physical principles of LDI-MS, but in addition, samples are co-crystalized with a matrix, generally a weak acid, that allows for the absorbance of the 337 or 355 nm laser wavelength.[61,95] The mixture is then irradiated by the pulsed laser which catalyzes the desorption of the matrix-analyte mixture into a gaseous plume.[96] This additional step allows molecules that are not conductive (as AuNPs are) to accept the laser energy and successfully ionize. The matrix additionally protects analyte molecules from the laser energy and subsequently keeps them intact, dubbing MALDI a "soft ionization technique."

In this dissertation, I will demonstrate the development of a dual-mode mass spectrometry imaging method to investigate the distribution of nanoparticle-based delivery vehicles and their biochemical changes in treated mouse tissues. I will further demonstrate how this method can be used to evaluate the efficacy and side effects of nanodelivery vehicles upon delivering its cargo. Because this method is based on mass spectrometry

methods, it will be applicable for evaluating other nanodelivery systems with a variety of cargos in the future.

1.6 Dissertation Overview

Nanoparticle-based systems have become extremely prevalent in biomedically relevant applications.[19] It is therefore important to develop analytical tools that can assess the distribution, accumulation, stability, and side effects of these materials along with their efficacy as therapeutics. Mass spectrometry has been used to successfully monitor the uptake and distribution of AuNPs in a variety of biological systems. LDI-MS is used to detect the intact ligands of AuNPs,[65] while ICP-MS provides quantitative information regarding the gold core. Both of these technique can additionally be used to evaluate the same information about AuNPs in a spatially-relevant context via mass spectrometry imaging.[40,55,58] In this dissertation, new analytical techniques combing MALDI, LDI, and ICP-MS will be designed to monitor the uptake, accumulation, excretion, and biochemical effects of AuNPs and AuNP-based nanodelivery vehicles.

First, in Chapter 2, I will illustrate the development of a dual-mode imaging method to track the distribution of a nanocarrier system and the biochemical effects of its deliverable cargo. LA-ICP-MS imaging along with MALDI-MSI imaging has been utilized to evaluate organic and inorganic constituents of biologically relevant molecules.[80,85] Applying this methodology, we designed an imaging workflow utilizing both MSI techniques to evaluate the distribution of a nanodelivery vehicle containing an AuNP carrier and an siRNA cargo in a mouse spleen tissue. Our method utilizes the strong correlation between Fe signals in LA-ICP-MS and heme B signals in MALDI-MS to overlay the images from the two modalities for comparison. We observed via MALDI-MSI that the majority of the predicted

biochemical changes were occurring as expected in in the white pulp of the spleen. However, we found through LA-ICP-MS analyses the AuNP carrier was accumulating in the red pulp of the spleen, indicating the biochemical changes are occurring independently of the carrier distribution. This information is only accessible by combining the imaging modalities.

In Chapter 3, I will further employ this method to evaluate the correlation between NPSC carrier and cargo delivery in different tissue types. Upon ICP-MS analysis, NPSCs are found to accumulate mostly in tissues involved in the mononuclear phagocyte system (MPS), i.e. the liver and spleen. We evaluated these tissues by MALDI-MSI to determine how many predicted biochemical changes are occurring and in what sub-organ regions. In contrast we evaluated NPSCs with non-interfering siRNA to confirm that biochemical changes were arising from the active siRNA cargo. Based on these results, we determined NPSCs successfully deliver an siRNA cargo and subsequently knock down a pathway with known biochemical responses. We then evaluated the tissues by LA-ICP-MS to determine which sub-organ regions the gold carrier distributes to. Utilizing both qualitative and quantitative measures, we found that the majority of the observed changes in both the liver and spleen are occurring where the carrier is not. Conversely, some unexpected biochemical changes were found to be correlated with the gold carrier.

In Chapter 4, we further evaluate the implications of these biochemical changes by exploring the lipid fluctuations that arise from the various NPSC components. Using MALDI-MS, we evaluated the lipid changes that were occurring in tissues upon injection with NPSCs containing an active siRNA, NPSCs containing an inactive siRNA, and pure AuNPs with no other constituents. Trends were observed for each of the nanomaterial-

injected tissues. These results demonstrate the power of our dual-mode imaging method to evaluate nanodelivery vehicles comprehensively. Additional evaluations will be conducted to determine the specific biological meaning and origins of these unpredicted changes.

In Chapter 5, I will discuss a method developed to quantitatively measure the cellular uptake and adhesion of AuNPs in cells. Utilizing LDI-MS, we found optimal laser fluencies that can be used to selectively desorb surface-bound AuNPs in in-tact cells. Comparing these signals to total NP signals obtained by LDI-MS or ICP-MS, we quantified the amount of cell-surface bound versus internalized AuNPs. This method was found to be applicable to many different cell types and in theory could be utilized to determine the internalization of any LDI- active NPs.

Finally, in Chapter 6, I will summarize the work that was completed towards my dissertation and discuss the possibilities for future experiments focusing on: 1) the advancement of analytical techniques to evaluate nanodelivery vehicles and 2) the role surface charge plays in distribution, accumulation, and excretion of AuNPs.

1.7 References

(1) Templeton, A. C.; Wuelfing, W. P.; Murray, R. W. Monolayer-Protected Cluster Molecules. *Acc. Chem. Res.* **2000**, *33* (1), 27–36.

(2) Sapsford, K. E.; Algar, W. R.; Berti, L.; Gemmill, K. B.; Casey, B. J.; Oh, E.; Stewart, M. H.; Medintz, I. L. Functionalizing Nanoparticles with Biological Molecules: Developing Chemistries That Facilitate Nanotechnology. *Chem. Rev.* **2013**, *113* (3), 1904–2074.

(3) Alkilany, A. M.; Lohse, S. E.; Murphy, C. J. The Gold Standard: Gold Nanoparticle Libraries To Understand the Nano–Bio Interface. *Acc. Chem. Res.* **2013**, *46* (3), 650–661.

(4) Jain, P. K.; Huang, X.; El-Sayed, I. H.; El-Sayed, M. A. Noble Metals on the Nanoscale: Optical and Photothermal Properties and Some Applications in Imaging, Sensing, Biology, and Medicine. *Acc. Chem. Res.* **2008**, *41* (12), 1578–1586.

(5)   Duncan, B.; Kim, C.; Rotello, V. M. Gold Nanoparticle Platforms as Drug and Biomacromolecule Delivery Systems. *J. Control. Release* **2010**, *148* (1), 122–127.

(6)   Jiang, Y.; Hardie, J.; Liu, Y.; Ray, M.; Luo, X.; Das, R.; Landis, R. F.; Farkas, M. E.; Rotello, V. M. Nanocapsule-Mediated Cytosolic SiRNA Delivery for Anti-Inflammatory Treatment. *J. Control. Release* **2018**, *283* (May), 235–240.

(7)   Hardie, J.; Jiang, Y.; Tetrault, E. R.; Ghazi, P. C.; Tonga, G. Y.; Farkas, M. E.; Rotello, V. M. Simultaneous Cytosolic Delivery of a Chemotherapeutic and SiRNA Using Nanoparticle-Stabilized Nanocapsules. *Nanotechnology* **2016**, *27* (37), 374001.

(8)   Mattoussi, H.; Rotello, V. M. Inorganic Nanoparticles in Drug Delivery. *Adv. Drug Deliv. Rev.* **2013**, *65* (5), 605–606.

(9)   Veiseh, O.; Gunn, J. W.; Zhang, M. Design and Fabrication of Magnetic Nanoparticles for Targeted Drug Delivery and Imaging. *Adv. Drug Deliv. Rev.* **2010**, *62* (3), 284–304.

(10)   Zhang, J.; Yuan, Z.-F.; Wang, Y.; Chen, W.-H.; Luo, G.-F.; Cheng, S.-X.; Zhuo, R.-X.; Zhang, X.-Z. Multifunctional Envelope-Type Mesoporous Silica Nanoparticles for Tumor-Triggered Targeting Drug Delivery. *J. Am. Chem. Soc.* **2013**, *135* (13), 5068–5073.

(11)   You, C.-C.; Chompoosor, A.; Rotello, V. M. The Biomacromolecule-Nanoparticle Interface. *Nano Today* **2007**, *2* (3), 34–43.

(12)   Mahmoudi, M.; Hosseinkhani, H.; Hosseinkhani, M.; Boutry, S.; Simchi, A.; Journeay, W. S.; Subramani, K.; Laurent, S. Magnetic Resonance Imaging Tracking of Stem Cells in Vivo Using Iron Oxide Nanoparticles as a Tool for the Advancement of Clinical Regenerative Medicine. *Chem. Rev.* **2011**, *111* (2), 253–280.

(13)   Chan, W. C. W. Quantum Dot Bioconjugates for Ultrasensitive Nonisotopic Detection. *Science (80-.).* **1998**, *281* (5385), 2016–2018.

(14)   Smith, A. M.; Duan, H.; Mohs, A. M.; Nie, S. Bioconjugated Quantum Dots for in Vivo Molecular and Cellular Imaging. *Adv. Drug Deliv. Rev.* **2008**, *60* (11), 1226–1240.

(15)   You, C.-C.; Miranda, O. R.; Gider, B.; Ghosh, P. S.; Kim, I.-B.; Erdogan, B.; Krovi, S. A.; Bunz, U. H. F.; Rotello, V. M. Detection and Identification of Proteins Using Nanoparticle–Fluorescent Polymer 'Chemical Nose' Sensors. *Nat. Nanotechnol.* **2007**, *2* (5), 318–323.

(16)   Kievit, F. M.; Zhang, M. Surface Engineering of Iron Oxide Nanoparticles for Targeted Cancer Therapy. *Acc. Chem. Res.* **2011**, *44* (10), 853–862.

(17)   Peer, D.; Karp, J. M.; Hong, S.; Farokhzad, O. C.; Margalit, R.; Langer, R. Nanocarriers as an Emerging Platform for Cancer Therapy. *Nat. Nanotechnol.* **2007**, *2* (12), 751–760.

(18)   Li, Z.; Barnes, J. C.; Bosoy, A.; Stoddart, J. F.; Zink, J. I. Mesoporous Silica Nanoparticles in Biomedical Applications. *Chem. Soc. Rev.* **2012**, *41* (7), 2590.

(19)   De, M.; Ghosh, P. S.; Rotello, V. M. Applications of Nanoparticles in Biology. *Adv. Mater.* **2008**, *20* (22), 4225–4241.

(20)   Daniel, M.-C.; Astruc, D. Gold Nanoparticles: Assembly, Supramolecular Chemistry, Quantum-Size-Related Properties, and Applications toward Biology, Catalysis, and Nanotechnology. *Chem. Rev.* **2004**, *104* (1), 293–346.

(21)   Boisselier, E.; Astruc, D. Gold Nanoparticles in Nanomedicine: Preparations, Imaging, Diagnostics, Therapies and Toxicity. *Chem. Soc. Rev.* **2009**, *38* (6), 1759.

(22)   Liu, W.; Howarth, M.; Greytak, A. B.; Zheng, Y.; Nocera, D. G.; Ting, A. Y.; Bawendi, M. G. Compact Biocompatible Quantum Dots Functionalized for Cellular Imaging. *J. Am. Chem. Soc.* **2008**, *130* (4), 1274–1284.

(23)   Susumu, K.; Uyeda, H. T.; Medintz, I. L.; Pons, T.; Delehanty, J. B.; Mattoussi, H. Enhancing the Stability and Biological Functionalities of Quantum Dots via Compact Multifunctional Ligands. *J. Am. Chem. Soc.* **2007**, *129* (45), 13987–13996.

(24)   Love, J. C.; Estroff, L. A.; Kriebel, J. K.; Nuzzo, R. G.; Whitesides, G. M. Self-Assembled Monolayers of Thiolates on Metals as a Form of Nanotechnology. *Chem. Rev.* **2005**, *105* (4), 1103–1170.

(25)   Whitesides, G. M.; Laibinis, P. E. Wet Chemical Approaches to the Characterization of Organic Surfaces: Self-Assembled Monolayers, Wetting, and the Physical-Organic Chemistry of the Solid-Liquid Interface. *Langmuir* **1990**, *6* (1), 87–96.

(26)   Jensen, T. R.; Malinsky, M. D.; Haynes, C. L.; Van Duyne, R. P. Nanosphere Lithography: Tunable Localized Surface Plasmon Resonance Spectra of Silver Nanoparticles. *J. Phys. Chem. B* **2000**, *104* (45), 10549–10556.

(27)   Nie, S. Probing Single Molecules and Single Nanoparticles by Surface-Enhanced Raman Scattering. *Science (80-.).* **1997**, *275* (5303), 1102–1106.

(28)   Jackson, A. M.; Hu, Y.; Silva, P. J.; Stellacci, F. From Homoligand- to Mixed-Ligand- Monolayer-Protected Metal Nanoparticles: A Scanning Tunneling Microscopy Investigation. *J. Am. Chem. Soc.* **2006**, *128* (34), 11135–11149.

(29)   Sun, S. Monodisperse FePt Nanoparticles and Ferromagnetic FePt Nanocrystal Superlattices. *Science (80-.).* **2000**, *287* (5460), 1989–1992.

(30)   Jadzinsky, P. D.; Calero, G.; Ackerson, C. J.; Bushnell, D. A.; Kornberg, R. D. Structure of a Thiol Monolayer-Protected Gold Nanoparticle at 1.1 A Resolution. *Science (80-.).* **2007**, *318* (5849), 430–433.

(31)   Heaven, M. W.; Dass, A.; White, P. S.; Holt, K. M.; Murray, R. W. Crystal Structure of the Gold Nanoparticle [N(C 8 H 17) 4][Au 25 (SCH 2 CH 2 Ph) 18]. *J. Am. Chem. Soc.* **2008**, *130* (12), 3754–3755.

(32)   Hostetler, M. J.; Wingate, J. E.; Zhong, C. J.; Harris, J. E.; Vachet, R. W.; Clark, M. R.; Londono, J. D.; Green, S. J.; Stokes, J. J.; Wignall, G. D.; et al. Alkanethiolate Gold Cluster Molecules with Core Diameters from 1.5 to 5.2 Nm: Core and Monolayer Properties as a Function of Core Size. *Langmuir* **1998**, *14* (1), 17–30.

(33)   Haiss, W.; Thanh, N. T. K.; Aveyard, J.; Fernig, D. G. Determination of Size and Concentration of Gold Nanoparticles from UV−Vis Spectra. *Anal. Chem.* **2007**, *79* (11), 4215–4221.

(34)   Zhou, H.; Li, X.; Lemoff, A.; Zhang, B.; Yan, B. Structural Confirmation and Quantification of Individual Ligands from the Surface of Multi-Functionalized Gold Nanoparticles. *Analyst* **2010**, *135* (6), 1210.

(35)   Whetten, R. L.; Khoury, J. T.; Alvarez, M. M.; Murthy, S.; Vezmar, I.; Wang, Z. L.; Stephens, P. W.; Cleveland, C. L.; Luedtke, W. D.; Landman, U. Nanocrystal Gold Molecules. *Adv. Mater.* **1996**, *8* (5), 428–433.

(36)   Nagahori, N.; Nishimura, S.-I. Direct and Efficient Monitoring of Glycosyltransferase Reactions on Gold Colloidal Nanoparticles by Using Mass Spectrometry. *Chem. - A Eur. J.* **2006**, *12* (25), 6478–6485.

(37)   Zhu, Z. J.; Ghosh, P. S.; Miranda, O. R.; Vachet, R. W.; Rotello, V. M. Multiplexed Screening of Cellular Uptake of Gold Nanoparticles Using Laser Desorption/Ionization Mass Spectrometry. *J. Am. Chem. Soc.* **2008**, *130* (43), 14139–14143.

(38)   Schaaff, T. G. Laser Desorption and Matrix-Assisted Laser Desorption/Ionization Mass Spectrometry of 29-KDa Au:SR Cluster Compounds. *Anal. Chem.* **2004**, *76* (21), 6187–6196.

(39)   Yan, B.; Jeong, Y.; Mercante, L. A.; Tonga, G. Y.; Kim, C.; Zhu, Z. J.; Vachet, R. W.; Rotello, V. M. Characterization of Surface Ligands on Functionalized Magnetic Nanoparticles Using Laser Desorption/Ionization Mass Spectrometry (LDI-MS). *Nanoscale* **2013**.

(40)   Elci, S. G.; Yesilbag Tonga, G.; Yan, B.; Kim, S. T.; Kim, C. S.; Jiang, Y.; Saha, K.; Moyano, D. F.; Marsico, A. L. M.; Rotello, V. M.; et al. Dual-Mode Mass Spectrometric Imaging for Determination of in Vivo Stability of Nanoparticle Monolayers. *ACS Nano* **2017**, *11* (7), 7424–7430.

(41)   Exner (Little Bear), F. Advances in Knowledge Discovery and Data Mining. *J. Am. Soc. Inf. Sci.* **1998**, *49* (4), 386–387.

(42)   Dass, A.; Holt, K.; Parker, J. F.; Feldberg, S. W.; Murray, R. W. Mass Spectrometrically Detected Statistical Aspects of Ligand Populations in Mixed Monolayer Au 25 L 18 Nanoparticles. *J. Phys. Chem. C* **2008**, *112* (51), 20276–20283.

(43) Dass, A.; Stevenson, A.; Dubay, G. R.; Tracy, J. B.; Murray, R. W. Nanoparticle MALDI-TOF Mass Spectrometry without Fragmentation: Au 25 (SCH 2 CH 2 Ph) 18 and Mixed Monolayer Au 25 (SCH 2 CH 2 Ph) 18− x (L) X. *J. Am. Chem. Soc.* **2008**, *130* (18), 5940–5946.

(44) Tracy, J. B.; Crowe, M. C.; Parker, J. F.; Hampe, O.; Fields-Zinna, C. A.; Dass, A.; Murray, R. W. Electrospray Ionization Mass Spectrometry of Uniform and Mixed Monolayer Nanoparticles: Au 25 [S(CH 2) 2 Ph] 18 and Au 25 [S(CH 2) 2 Ph] 18 - x (SR) X. *J. Am. Chem. Soc.* **2007**, *129* (51), 16209–16215.

(45) Tracy, J. B.; Kalyuzhny, G.; Crowe, M. C.; Balasubramanian, R.; Choi, J. P.; Murray, R. W. Poly(Ethylene Glycol) Ligands for High-Resolution Nanoparticle Mass Spectrometry. *J. Am. Chem. Soc.* **2007**, *129* (21), 6706–6707.

(46) Dass, A.; Dubay, G. R.; Fields-Zinna, C. A.; Murray, R. W. FAB Mass Spectrometry of Au 25 (SR) 18 Nanoparticles. *Anal. Chem.* **2008**, *80* (18), 6845–6849.

(47) Kpegba, K.; Spadaro, T.; Cody, R. B.; Nesnas, N.; Olson, J. A. Analysis of Self-Assembled Monolayers on Gold Surfaces Using Direct Analysis in Real Time Mass Spectrometry. *Anal. Chem.* **2007**, *79* (14), 5479–5483.

(48) Manova, R. K.; Joshi, S.; Debrassi, A.; Bhairamadgi, N. S.; Roeven, E.; Gagnon, J.; Tahir, M. N.; Claassen, F. W.; Scheres, L. M. W.; Wennekes, T.; et al. Ambient Surface Analysis of Organic Monolayers Using Direct Analysis in Real Time Orbitrap Mass Spectrometry. *Anal. Chem.* **2014**, *86* (5), 2403–2411.

(49) Angel, L. A.; Majors, L. T.; Dharmaratne, A. C.; Dass, A. Ion Mobility Mass Spectrometry of Au 25 (SCH 2 CH 2 Ph) 18 Nanoclusters. *ACS Nano* **2010**, *4* (8), 4691–4700.

(50) Harkness, K. M.; Cliffel, D. E.; McLean, J. A. Characterization of Thiolate-Protected Gold Nanoparticles by Mass Spectrometry. *Analyst* **2010**, *135* (5), 868.

(51) Harkness, K. M.; Balinski, A.; McLean, J. A.; Cliffel, D. E. Nanoscale Phase Segregation of Mixed Thiolates on Gold Nanoparticles. *Angew. Chemie Int. Ed.* **2011**, *50* (45), 10554–10559.

(52) Kang, S.; Mauter, M. S.; Elimelech, M. Microbial Cytotoxicity of Carbon-Based Nanomaterials: Implications for River Water and Wastewater Effluent. *Environ. Sci. Technol.* **2009**, *43* (7), 2648–2653.

(53) Drescher, D.; Zeise, I.; Traub, H.; Guttmann, P.; Seifert, S.; Büchner, T.; Jakubowski, N.; Schneider, G.; Kneipp, J. In Situ Characterization of SiO 2 Nanoparticle Biointeractions Using BrightSilica. *Adv. Funct. Mater.* **2014**, *24* (24), 3765–3775.

(54) Lin, S.; Reppert, J.; Hu, Q.; Hudson, J. S.; Reid, M. L.; Ratnikova, T. A.; Rao, A. M.; Luo, H.; Ke, P. C. Uptake, Translocation, and Transmission of Carbon Nanomaterials in Rice Plants. *Small* **2009**, *5* (10), 1128–1132.

(55)   Yan, B.; Kim, S. T.; Kim, C. S.; Saha, K.; Moyano, D. F.; Xing, Y.; Jiang, Y.; Roberts, A. L.; Alfonso, F. S.; Rotello, V. M.; et al. Multiplexed Imaging of Nanoparticles in Tissues Using Laser Desorption/Ionization Mass Spectrometry. *J. Am. Chem. Soc.* **2013**, *135* (34), 12564–12567.

(56)   Elci, S. G.; Yan, B.; Kim, S. T.; Saha, K.; Jiang, Y.; Klemmer, G. A.; Moyano, D. F.; Tonga, G. Y.; Rotello, V. M.; Vachet, R. W. Quantitative Imaging of 2 Nm Monolayer-Protected Gold Nanoparticle Distributions in Tissues Using Laser Ablation Inductively-Coupled Plasma Mass Spectrometry (LA-ICP-MS). *Analyst* **2016**, *141* (8), 2418–2425.

(57)   Elci, S. G.; Jiang, Y.; Yan, B.; Kim, S. T.; Saha, K.; Moyano, D. F.; Yesilbag Tonga, G.; Jackson, L. C.; Rotello, V. M.; Vachet, R. W. Surface Charge Controls the Suborgan Biodistributions of Gold Nanoparticles. *ACS Nano* **2016**, *10* (5), 5536–5542.

(58)   Yan, B.; Zhu, Z. J.; Miranda, O. R.; Chompoosor, A.; Rotello, V. M.; Vachet, R. W. Laser Desorption/Ionization Mass Spectrometry Analysis of Monolayer-Protected Gold Nanoparticles. *Anal. Bioanal. Chem.* **2010**.

(59)   Yan, B.; Jeong, Y.; Mercante, L. a; Tonga, G. Y.; Kim, C.; Zhu, Z. J.; Vachet, R. W.; Rotello, V. M. Characterization of Surface Ligands on Functionalized Magnetic Nanoparticles Using Laser Desorption/Ionization Mass Spectrometry (LDI-MS). *Nanoscale* **2013**, *5* (11), 5063–5066.

(60)   Marsico, A. L. M.; Elci, G. S.; Moyano, D. F.; Yesilbag Tonga, G.; Duncan, B.; Landis, R. F.; Rotello, V. M.; Vachet, R. W. Enhanced Laser Desorption/Ionization Mass Spectrometric Detection of Gold Nanoparticles in Biological Samples Using the Synergy between Added Matrix and the Gold Core. *Anal. Chem.* **2015**, *87* (24), 12145–12150.

(61)   Glish, G. L.; Vachet, R. W. The Basics of Mass Spectrometry in the Twenty-First Century. *Nat. Rev. Drug Discov.* **2003**, *2* (2), 140–150.

(62)   Yan, B.; Kim, S. T.; Kim, C. S.; Saha, K.; Moyano, D. F.; Xing, Y.; Jiang, Y.; Roberts, A. L.; Alfonso, F. S.; Rotello, V. M.; et al. Multiplexed Imaging of Nanoparticles in Tissues Using Laser Desorption/Ionization Mass Spectrometry. *J. Am. Chem. Soc.* **2013**, *135* (34), 12564–12567.

(63)   Zhu, Z. J.; Carboni, R.; Quercio, M. J.; Yan, B.; Miranda, O. R.; Anderton, D. L.; Arcaro, K. F.; Rotello, V. M.; Vachet, R. W. Surface Properties Dictate Uptake, Distribution, Excretion, and Toxicity of Nanoparticles in Fish. *Small* **2010**, *6* (20), 2261–2265.

(64)   Saha, K.; Kim, S. T.; Yan, B.; Miranda, O. R.; Alfonso, F. S.; Shlosman, D.; Rotello, V. M. Surface Functionality of Nanoparticles Determines Cellular Uptake Mechanisms in Mammalian Cells. *Small* **2013**, *9* (2), 300–305.

(65)   Zhu, Z. J.; Tang, R.; Yeh, Y.-C.; Miranda, O. R.; Rotello, V. M.; Vachet, R. W. Determination of the Intracellular Stability of Gold Nanoparticle Monolayers Using Mass Spectrometry. *Anal. Chem.* **2012**, *84* (10), 4321–4326.

(66) Zhu, Z. J.; Yeh, Y.-C.; Tang, R.; Yan, B.; Tamayo, J.; Vachet, R. W.; Rotello, V. M. Stability of Quantum Dots in Live Cells. *Nat. Chem.* **2011**, *3* (12), 963–968.

(67) Medintz, I. L.; Uyeda, H. T.; Goldman, E. R.; Mattoussi, H. Quantum Dot Bioconjugates for Imaging, Labelling and Sensing. *Nat. Mater.* **2005**, *4* (6), 435–446.

(68) Cheng, Y.; Meyers, J. D.; Broome, A.-M.; Kenney, M. E.; Basilion, J. P.; Burda, C. Deep Penetration of a PDT Drug into Tumors by Noncovalent Drug-Gold Nanoparticle Conjugates. *J. Am. Chem. Soc.* **2011**, *133* (8), 2583–2591.

(69) Yan, B.; Kim, S. T.; Kim, C. S.; Saha, K.; Moyano, D. F.; Xing, Y.; Jiang, Y.; Roberts, A. L.; Alfonso, F. S.; Rotello, V. M.; et al. Multiplexed Imaging of Nanoparticles in Tissues Using Laser Desorption/Ionization Mass Spectrometry. *J. Am. Chem. Soc.* **2013**, *135* (34), 12564–12567.

(70) Creran, B.; Yan, B.; Moyano, D. F.; Gilbert, M. M.; Vachet, R. W.; Rotello, V. M. Laser Desorption Ionization Mass Spectrometric Imaging of Mass Barcoded Gold Nanoparticles for Security Applications. *Chem. Commun.* **2012**, *48* (38), 4543.

(71) Li, M.; Luo, Z.; Yan, Y.; Wang, Z.; Chi, Q.; Yan, C.; Xing, B. Arsenate Accumulation, Distribution, and Toxicity Associated with Titanium Dioxide Nanoparticles in Daphnia Magna. *Environ. Sci. Technol.* **2016**, *50* (17), 9636–9643.

(72) Wu, B.; Becker, J. S. Imaging of Elements and Molecules in Biological Tissues and Cells in the Low-Micrometer and Nanometer Range. *Int. J. Mass Spectrom.* **2011**, *307* (1–3), 112–122.

(73) Mahmoud, N. N.; Alkilany, A. M.; Dietrich, D.; Karst, U.; Al-Bakri, A. G.; Khalil, E. A. Preferential Accumulation of Gold Nanorods into Human Skin Hair Follicles: Effect of Nanoparticle Surface Chemistry. *J. Colloid Interface Sci.* **2017**, *503*, 95–102.

(74) Li, Z.; Tan, S.; Li, S.; Shen, Q.; Wang, K. Cancer Drug Delivery in the Nano Era: An Overview and Perspectives. *Oncol. Rep.* **2017**, *38* (2), 611–624.

(75) Babu, A.; Templeton, A. K.; Munshi, A.; Ramesh, R. Nanodrug Delivery Systems: A Promising Technology for Detection, Diagnosis, and Treatment of Cancer. *AAPS PharmSciTech* **2014**, *15* (3), 709–721.

(76) Abrams, M. T.; Koser, M. L.; Seitzer, J.; Williams, S. C.; DiPietro, M. A.; Wang, W.; Shaw, A. W.; Mao, X.; Jadhav, V.; Davide, J. P.; et al. Evaluation of Efficacy, Biodistribution, and Inflammation for a Potent SiRNA Nanoparticle: Effect of Dexamethasone Co-Treatment. *Mol. Ther.* **2010**, *18* (1), 171–180.

(77) Whitehead, K. A.; Langer, R.; Anderson, D. G. Knocking down Barriers: Advances in SiRNA Delivery. *Nat. Rev. Drug Discov.* **2009**, *8* (2), 129–138.

(78) Hofmann, D.; Messerschmidt, C.; Bannwarth, M. B.; Landfester, K.; Mailänder, V. Drug Delivery without Nanoparticle Uptake: Delivery by a Kiss-and-Run Mechanism on the Cell Membrane. *Chem. Commun.* **2014**, *50* (11), 1369–1371.

(79)   Yang, X.-C.; Samanta, B.; Agasti, S. S.; Jeong, Y.; Zhu, Z. J.; Rana, S.; Miranda, O. R.; Rotello, V. M. Drug Delivery Using Nanoparticle-Stabilized Nanocapsules. *Angew. Chemie Int. Ed.* **2011**, *50* (2), 477–481.

(80)   Tang, R.; Kim, C. S.; Solfiell, D. J.; Rana, S.; Mout, R.; Velázquez-Delgado, E. M.; Chompoosor, A.; Jeong, Y.; Yan, B.; Zhu, Z. J.; et al. Direct Delivery of Functional Proteins and Enzymes to the Cytosol Using Nanoparticle-Stabilized Nanocapsules. *ACS Nano* **2013**, *7* (8), 6667–6673.

(81)   Liu, J.; Stace-Naughton, A.; Jiang, X.; Brinker, C. J. Porous Nanoparticle Supported Lipid Bilayers (Protocells) as Delivery Vehicles. *J. Am. Chem. Soc.* **2009**, *131* (4), 1354–1355.

(82)   Rodenak-Kladniew, B.; Islan, G. A.; de Bravo, M. G.; Durán, N.; Castro, G. R. Design, Characterization and in Vitro Evaluation of Linalool-Loaded Solid Lipid Nanoparticles as Potent Tool in Cancer Therapy. *Colloids Surfaces B Biointerfaces* **2017**, *154*, 123–132.

(83)   García, K. P.; Zarschler, K.; Barbaro, L.; Barreto, J. A.; O'Malley, W.; Spiccia, L.; Stephan, H.; Graham, B. Zwitterionic-Coated "Stealth" Nanoparticles for Biomedical Applications: Recent Advances in Countering Biomolecular Corona Formation and Uptake by the Mononuclear Phagocyte System. *Small* **2014**, *10* (13), 2516–2529.

(84)   Hofmann, D.; Tenzer, S.; Bannwarth, M. B.; Messerschmidt, C.; Glaser, S.-F.; Schild, H.; Landfester, K.; Mailänder, V. Mass Spectrometry and Imaging Analysis of Nanoparticle-Containing Vesicles Provide a Mechanistic Insight into Cellular Trafficking. *ACS Nano* **2014**, *8* (10), 10077–10088.

(85)   Svatoš, A. Mass Spectrometric Imaging of Small Molecules. *Trends Biotechnol.* **2010**, *28* (8), 425–434.

(86)   Esquenazi, E.; Yang, Y. L.; Watrous, J.; Gerwick, W. H.; Dorrestein, P. C. Imaging Mass Spectrometry of Natural Products. *Nat. Prod. Rep.* **2009**, *26* (12), 1521–1534.

(87)   Zemski Berry, K. A.; Hankin, J. A.; Barkley, R. M.; Spraggins, J. M.; Caprioli, R. M.; Murphy, R. C. MALDI Imaging of Lipid Biochemistry in Tissues by Mass Spectrometry. *Chem. Rev.* **2011**, *111* (10), 6491–6512.

(88)   Stoeckli, M.; Staab, D.; Schweitzer, A. Compound and Metabolite Distribution Measured by MALDI Mass Spectrometric Imaging in Whole-Body Tissue Sections. *Int. J. Mass Spectrom.* **2007**, *260* (2–3), 195–202.

(89)   Cillero-Pastor, B.; Heeren, R. M. A. Matrix-Assisted Laser Desorption Ionization Mass Spectrometry Imaging for Peptide and Protein Analyses: A Critical Review of On-Tissue Digestion. *J. Proteome Res.* **2014**, *13* (2), 325–335.

(90)   Lukowski, J. K.; Weaver, E. M.; Hummon, A. B. Analyzing Liposomal Drug Delivery Systems in Three-Dimensional Cell Culture Models Using MALDI Imaging Mass Spectrometry. *Anal. Chem.* **2017**, *89* (16), 8453–8458.

(91) Fülöp, A.; Sammour, D. A.; Erich, K.; von Gerichten, J.; van Hoogevest, P.; Sandhoff, R.; Hopf, C. Molecular Imaging of Brain Localization of Liposomes in Mice Using MALDI Mass Spectrometry. *Sci. Rep.* **2016**, *6* (1), 33791.

(92) Holzlechner, M.; Bonta, M.; Lohninger, H.; Limbeck, A.; Marchetti-Deschmann, M. Multisensor Imaging—From Sample Preparation to Integrated Multimodal Interpretation of LA-ICPMS and MALDI MS Imaging Data. *Anal. Chem.* **2018**, *90* (15), 8831–8837.

(93) de Vega, R. G.; Sanchez, M. L. F.; Eiro, N.; Vizoso, F. J.; Sperling, M.; Karst, U.; Medel, A. S. Multimodal Laser Ablation/Desorption Imaging Analysis of Zn and MMP-11 in Breast Tissues. *Anal. Bioanal. Chem.* **2018**, *410* (3), 913–922.

(94) Niehoff, A.-C.; Schulz, J.; Soltwisch, J.; Meyer, S.; Kettling, H.; Sperling, M.; Jeibmann, A.; Dreisewerd, K.; Francesconi, K. A.; Schwerdtle, T.; et al. Imaging by Elemental and Molecular Mass Spectrometry Reveals the Uptake of an Arsenolipid in the Brain of Drosophila Melanogaster. *Anal. Chem.* **2016**, *88* (10), 5258–5263.

(95) Lewis, J. K.; Wei, J.; Siuzdak, G. Matrix-Assisted Laser Desorption/Ionization Mass Spectrometry in Peptide and Protein Analysis. In *Encyclopedia of Analytical Chemistry*; John Wiley & Sons, Ltd: Chichester, UK, 2006; pp 5880–5894.

(96) Knochenmuss, R.; Zenobi, R. MALDI Ionization: The Role of In-Plume Processes. *Chem. Rev.* **2003**, *103* (2), 441–452.

(97) Elci, S. G.; Yan, B.; Kim, S. T.; Saha, K.; Jiang, Y.; Klemmer, G. A.; Moyano, D. F.; Tonga, G. Y.; Rotello, V. M.; Vachet, R. W. Quantitative Imaging of 2 Nm Monolayer-Protected Gold Nanoparticle Distributions in Tissues Using Laser Ablation Inductively-Coupled Plasma Mass Spectrometry (LA-ICP-MS). *Analyst* **2016**, *141* (8), 2418–2425.

(98) Wallace, M.; Morris, C.; O'Grada, C. M.; Ryan, M.; Dillon, E. T.; Coleman, E.; Gibney, E. R.; Gibney, M. J.; Roche, H. M.; Brennan, L. Relationship between the Lipidome, Inflammatory Markers and Insulin Resistance. *Mol. BioSyst.* **2014**, *10* (6), 1586–1595.

CHAPTER 2

DUAL MASS SPECTROMETRIC TISSUE IMAGING OF NANOCARRIER DISTRIBUTIONS AND THEIR BIOCHEMICAL EFFECTS

Abstract:

Nanomaterial-based drug delivery vehicles are able to deliver therapeutics in a controlled, targeted manner. Currently, however, there are limited analytical methods that can detect both nanomaterial distributions and their biochemical effects concurrently. In this study, we demonstrate that matrix assisted laser desorption/ionization mass spectrometry imaging (MALDI-MSI) and laser ablation inductively coupled plasma mass spectrometry imaging (LA-ICP-MSI) can be used together to obtain nanomaterial distributions and biochemical consequences. These studies employ nanoparticle-stabilized capsules (NPSCs) loaded with siRNA as a testbed. MALDI-MSI experiments on spleen tissues from intravenously injected mice indicate that NPSCs loaded with TNF-α-specific siRNA cause changes to lipid composition in white pulp regions of the spleen, as anticipated, based on pathways known to be affected by TNF-α, whereas NPSCs loaded with scrambled siRNA do not cause the predicted changes. Interestingly, LA-ICP-MSI experiments reveal that the NPSCs primarily localize in the red pulp, suggesting that the observed changes in lipid composition are due to diffusive rather than localized effects on TNF-α production. Such information is only accessible by combining data from the two

modalities, which we accomplish by using the heme signals from MALDI-MSI and Fe signals from LA-ICP-MSI to overlay the images. Several unexpected changes in lipid composition also occur in regions where the NPSCs are found, suggesting that the NPSCs themselves can influence tissue biochemistry as well.

2.1 Introduction

Nanomaterials have been widely employed over the past two decades for therapeutic delivery[1] due to their tunable size, structure, and physical properties.[2] Nanomaterial-based drug delivery systems, generally directed by macromolecular self-assembly, provide a great deal of tunability for delivery purposes.[3] Nanoparticles (NPs) can be designed to carry drugs/cargo either on their surfaces or in their interiors.[4] Other molecules, such as lipids, can be incorporated to improve cargo loading.[5,6] The versatility of these systems allows for delivery of a range of therapeutic cargos, including siRNA,[7–9] hydrophobic drugs,[10,11] proteins,[12] and combination therapies,[13,14] often at safer and more effective dosages than those used for the corresponding therapeutics alone.[4] While nano-based delivery systems have great potential, there is a need for analytical tools to map their biodistributions and the biochemical changes they may cause *in vivo* to fully assess their effectiveness.

Obtaining site-specific information about carriers and their biochemical effects is challenging. Fluorescence microscopy is the most commonly utilized technique for evaluating the biodistribution of nano-based delivery vehicles because of its accessibility and excellent spatial resolution. This technique, however, is limited in its ability to identify biochemical changes, and some nanomaterials do not readily lend themselves to being tracked by fluorescence. Liquid chromatography coupled with mass spectrometry (LC-MS) is a powerful tool to determine biochemical changes that arise upon injection of nano-

based drug delivery systems,[15] but LC-MS does not readily provide spatial information. Spatial context is essential for understanding the direct and indirect biochemical effects of the nanocarrier in relation to its distribution. Sub-organ distributions in the liver and spleen, for example, can reveal how the reticuloendothelial system responds to the presence of nanomaterials.[16,17]

Mass spectrometry imaging (MSI) has the potential to provide needed site-specific information for nano-based drug delivery systems and their biochemical effects due to its 'universal' detection capability. MALDI-based MSI has emerged as a powerful tool for determining the distributions of a wide range of compounds, including small molecules,[18,19] lipids,[20] drugs and their metabolites,[21] and peptides and proteins[22] in biological samples such as tissues, cell cultures, and even whole organisms.[21,23,24] Using MALDI-MSI to study the biodistributions of nano-based delivery vehicles, however, has been quite limited. In one example the distribution of a liposomal carrier, loaded with a fluorophore, was monitored by MALDI-MSI,[25] and in another, MALDI-MSI was used to determine the distribution of liposomal-conjugated doxorubicin in 3D cell culture.[26] In no instances have nano-based drug delivery carriers and their corresponding biochemical effects been site-specifically monitored together in the same tissue.

While MALDI-MSI techniques have not been commonly applied to monitor the distribution of nano-based delivery systems, laser ablation inductively coupled plasma (LA-ICP) MSI[16,17,27,28] and laser desorption ionization MSI techniques[29–31] have been used for inorganic-based NP systems. Together, MALDI-MSI and LA-ICP-MSI can provide complementary information about the biodistributions of molecules that have both inorganic and organic components. Recent work has demonstrated the benefits of

23

combining MALDI-MS and LA-ICP-MS imaging techniques to evaluate the inorganic and organic portions of small molecule drugs,[32] enzymes and their potential regulators,[33] as well as uptake of arsenic-containing lipids in a fruit fly model.[34] When used together, the two techniques have even greater potential to reveal the sub-organ biodistributions of nano-based drug delivery systems while at the same time monitoring any biochemical effects caused by the presence of these systems.

Here, we describe a dual-mode imaging approach based on MALDI-MS and LA-ICP-MS for monitoring the distributions and biochemical effects of a nano-based drug-delivery system. For proof of concept, we use NP stabilized capsules (NPSCs) loaded with tumor necrosis factor alpha (TNF-α)-targeting small interfering RNA (siRNA) as a test-bed material (Figure 2.1). NPSCs are gold NP-based nanocarriers that have been used to deliver proteins, small molecules, and siRNA directly to the cytoplasm of cells.[7,11,12,14,35] NPSCs bearing anti-TNF-α siRNA have been shown to result in knock-down *in vitro* and *in vivo*.[7] Separate studies show that the reduction of TNF-α results in predictable biochemical responses, specifically lipid changes.[36] Hence, NPSCs loaded with anti-TNF-α are excellent system for mapping the relationship between these biochemical changes and NP
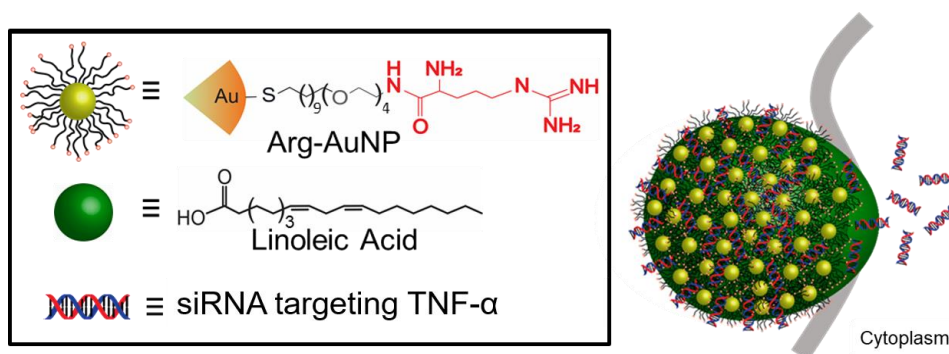
Figure 2.1. NPSC composition and AuNP-ligand structure. Arginine-based ligands (arginine shown in red) are conjugated to the AuNPs. The Arg-AuNPs are emulsified with linoleic acid and allowed to associate with the siRNA cargo.

carrier distributions. By utilizing MALDI-MSI to monitor the predicted, altered lipid composition and LA-ICP-MS to monitor the NP carrier, we can determine whether biochemical changes occur only at sites of delivery agent accumulation or more broadly. When used together, the two imaging techniques reveal both local and systemic changes caused by anti-TNF-α-loaded NPSCs, highlighting the power of this dual-mode imaging approach.

2.2 Results and Discussion

2.2.1 MALDI-MS imaging of spleen tissues from control mice and mice injected with NPSCs

The spleen was chosen for imaging because high concentrations of gold are measured by ICP-MS in this organ after injection of the NPSCs into mice (Table 2.1). In addition, this tissue has three distinct sub-organ regions with different cell types, including the white pulp that is rich in macrophages that produce TNF-α. We focused on the analysis of lipids because dysregulation of the lipidome is an indicator of variations in TNF-α production.[37,38]

Table 2.1. ICP-MS analyses of TNF-α and scrambled NPSC-injected mouse tissues. All concentrations are reported as the average among three mice. Error is reported as standard deviation.

Tissue Type	Gold Concentration for TNF-α NPSC mice (ppb)	Gold Concentration for Scrambled NPSC mice (ppb)
Spleen	26000 ± 2000	20000 ± 3000
Liver	23000 ± 3000	20000 ± 3000
Kidney	220 ± 20	310 ± 10
Lung	3500 ± 900	3000 ± 400
Heart	900 ± 500	890 ± 200
Blood	150 ± 40	70 ± 40
Small Intestine	90 ± 20	160 ± 20
Brain	10 ± 1	20 ± 10

Table 2.2. Characteristic lipid ions in the spleen of anti-TNF-α NPSC-injected mice.

Lipid I.D.[a]	Detected m/z	Ion(s)	Increased (+) or Decreased (-)in NPSC-Injected Mouse Tissues	Change as Predicted?[b]	ROC AUC[c]	Spleen Region
LPC (16:0)	496.3 518.4	[M + H⁺] [M + Na⁺]	(+)	Yes	0.745 0.684	White Pulp
LPC (18:0)	524.4	[M + H⁺]	(+)	Yes	0.682	White Pulp
LPC (p-18:0)	508.6	[M + H⁺]	(-)	No	0.306	Red Pulp
LPC (18:2)	520.2	[M + H⁺]	None	Yes	0.501	White Pulp
LPC (20:4)	544.3	[M + H⁺]	(-)	No	0.345	Red Pulp
PC (30:0)	706.6	[M + H⁺]	None	Yes	0.550	White Pulp
PC (32:0)	734.5 772.5	[M + H⁺] [M + K⁺]	(+)	No	0.724	White Pulp
PC (p-32:0)	756.5	[M + Na⁺]	(+)	Yes	0.706	White Pulp
PC (34:0)	762.6	[M + H⁺]	(+)	Yes	0.785	White Pulp
PC (p-34:0)	746.6	[M + H⁺]	(+)	Yes	0.692	White Pulp
PC (34:1)	760.6 798.6	[M + H⁺] [M + K⁺]	None	Yes	0.418 0.616	White Pulp
PC (p-34:1)	744.6	[M + H⁺]	None	Yes	0.446	White Pulp
PC (34:2)	780.5	[M + Na⁺]	None	Yes	0.450	White Pulp
PC (34:3)	756.6	[M + H⁺]	(+)	No	0.718	White Pulp
PC (p-36:5)	786.6 802.5	[M + Na⁺] [M + K⁺]	(+)	Yes	0.721 0.733	White Pulp
PC (p-36:4)	788.6 804.5	[M + Na⁺] [M + K⁺]	(+)	Yes	0.684	White Pulp
PC (p-36:2)	770.6 792.6 808.5	[M + H⁺] [M + Na⁺] [M + K⁺]	(+)	Yes	0.730 0.754 0.733	White Pulp
PC (36:0)[d]	790.6 812.6 828.5	[M + H⁺] [M + Na⁺] [M + K⁺]	(+)	Yes	0.695 0.752 0.704	White Pulp
PC (p-38:6)[d]	790.6 812.6 828.5	[M + H⁺] [M + Na⁺] [M + K⁺]	(+)	Yes	0.695 0.752 0.704	White Pulp
PC (p-38:5)	792.5 830.5	[M + H⁺] [M + K⁺]	(+)	Yes	0.754 0.786	White Pulp
PC (p-38:4)	794.7 816.6 832.5	[M + H⁺] [M + Na⁺] [M + K⁺]	(+)	Yes	0.737 0.682 0.733	White Pulp
PC (p-40:5)	820.6, 858.6	[M + H⁺], [M + K⁺]	(+)	Yes	0.715 0.716	White Pulp
2H OH Cer (d18:1/20:0)	632.5 650.5	[M – H₂O + K⁺] [M + K⁺]	(-)	Yes	0.258 0.343	Red Pulp

Lipid	m/z	Adduct	Change[b]	Correlated[?]	ROC AUC[c]	Location
2H Cer (d18:1/25:1)	681.7	[M + NH$_4^+$]	(-)	Yes	0.331	Red Pulp
2H Cer (d18:1/20:1)	632.5	[M + K$^+$]	(-)	No	0.343	Red Pulp
SM (d18:1/17:0)	741.6 757.6	[M + Na$^+$] [M + K$^+$]	(+)	Yes	0.714 0.759	White Pulp
SM (d18:1/20:0)	759.6	[M + H$^+$]	(+)	Yes	0.767	White Pulp
SM (d18:1/21:1)	771.6 809.6	[M + H$^+$] [M + K$^+$]	(+)	Yes	0.734 0.709	Both
SM (d18:1/23:2)	819.6	[M + Na$^+$]	(-)	Yes	0.283	White Pulp
SM (d18:1/24:0)	853.7	[M + K$^+$]	(+)	Yes	0.740	White Pulp
SM (d18:1/24:3)	809.6 847.6	[M + H$^+$] [M + K$^+$]	(+)	No	0.709 0.703	Both
PE (26:4)	497.2	[M – HG + K$^+$]	(+)	Yes	0.745	Both
PE (p-34:3)	557.5	[M – HG + H$^+$]	(+)	Yes	0.664	Red Pulp
PE (p-34:2)	559.5 581.5	[M – HG + H$^+$] [M – HG + Na$^+$]	None	No	0.476	Both
PE (p-34:1)d	583.5	[M – HG + H$^+$]	(-)	No	0.324	Red Pulp
PE (p-36:4)[d]	583.5	[M – HG + Na$^+$]	(-)	No	0.324	Red Pulp
PE (p-34:1)[d]	732.5	[M + H$^+$]	(+)	Yes	0.661	White Pulp
PE (p-36:4)[d]	724.5	[M + Na$^+$]	(+)	Yes	0.661	White Pulp
PE (p-36:3)	585.5	[M – HG + H$^+$]	(+)	Yes	0.693	Red Pulp
PE (38:2)	669.5	[M – HG + K$^+$]	(+)	Yes	0.653	Red Pulp
PE (38:1)[d]	671.5	[M – HG + K$^+$]	None	No	0.546	Red Pulp
PE (p-40:5)[d]	671.5	[M – HG + K$^+$]	None	No	0.546	Red Pulp
CAR (16:0)	400.4	[M + H$^+$]	(-)	Yes	0.293	White Pulp
CAR (18:1)	426.6	[M + H$^+$]	(-)	Yes	0.318	White Pulp

[a] The included lipids were measured in separate imaging experiments of spleen tissue slices from three different mice. A combination of exact mass determination from post-acquisition calibration, LIPIDMAPS, and MS/MS were used to identify each lipid. (Abbreviations: LPC – lysophosphatidylcholine; PC – phosphatidylcholine; Cer – ceramide; SM – sphingomyelin; PE – phosphatidylethanolamine; CAR – carnitine; "p-" – plasmalogen; HG – headgroup) [b] Changes correlated to previously reported lipidomics data.[36] [c] ROC AUCs were determined using SCiLS lab software. Values represent anti-TNF-α NPSC tissues vs. control tissues. Values greater than 0.65 and less than 0.35 were considered significantly different. [d] These lipids are not distinguishable by MS/MS.

Using MALDI-MSI, 52 identifiable lipids were detected in positive mode in separate imaging experiments (a complete list of lipids can be found in Table A.1 in the Appendix), with 44 of these having been previously shown to correlate with TNF-α levels (Table 2.2).[36] Relative to tissues from control mice, some lipid levels from NPSC-injected mice undergo statistically significant increases (e.g. Figures 2.2a & 2.2d) or decreases (e.g. Figures 2.2b & 2.2e), while others remain the same (e.g. Figures 2.2c & 2.2f) according to both ROC curves and box-and-whisker plots (Figures 2.3-2.5). As an example, relative ion abundances for phosphatidylcholine (PC) (p-40:5), where "p" indicates a plasmalogen species (Figure 2.2a), results in an AUC of 0.715 when comparing tissues from control and NPSC-treated mice (Figure 2.3), indicating that the level of this lipid increases significantly. A similar conclusion is obtained from ion abundance box-and-whisker plots
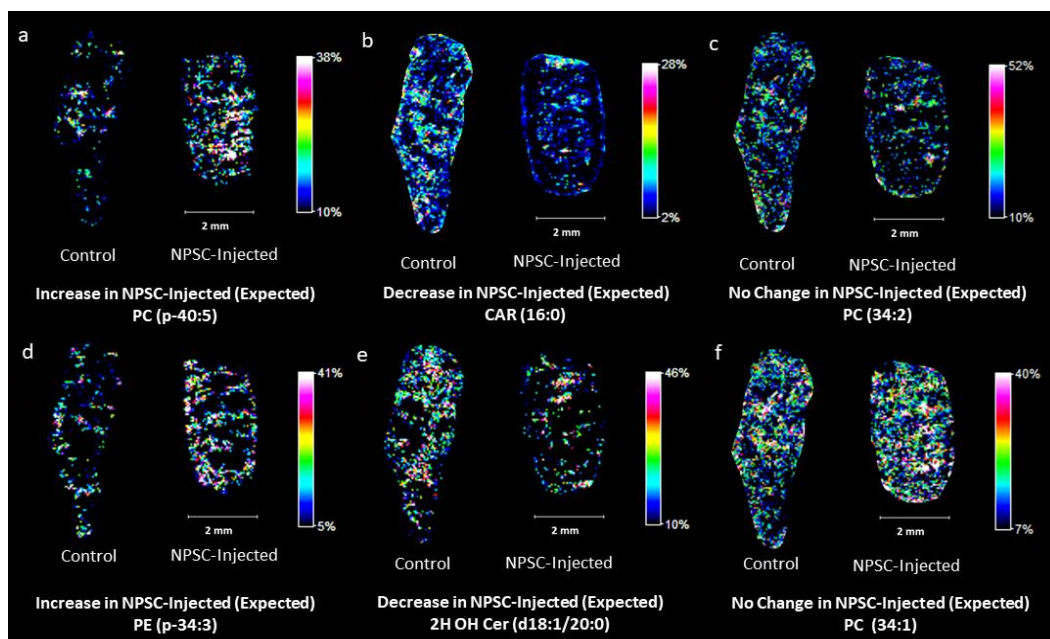
Figure 2.2. Representative images of lipid responses in NPSC-injected mouse spleen tissues (right in each image pair) compared to control tissues (left in each image pair). Panels (a) and (d) are examples of lipids predicted to increase in the spleen upon TNF-α knockdown. Panels (b) and (e) are examples of lipids predicted to decrease in the spleen upon TNF-α knockdown. Panels (c) and (f) are examples of lipids predicted to retain consistent levels upon TNF-α knockdown.[36]

(Figure 2.5). In contrast, carnitine (CAR) (16:0) (Figure 2.2b) has an AUC value of 0.293, indicating a significant decrease in the level of this lipid between the control and NPSC-treated tissues. To check if the AuNPs themselves were affecting lipid ionization efficiencies in the MALDI experiments, control experiments were performed with biologically relevant concentrations of AuNPs. Lipid levels were found to be relatively unaffected by the presence of AuNPs even at concentrations above those detected in mouse tissues (Figure 2.6).

Of the 44 measured lipids that have known responses in serum to TNF-α knockdown, we find that 75% respond as predicted in the spleen tissues (Table 2.2), indicating that MALDI-MSI can provide data that are consistent with previous lipidomics experiments from serum samples.[36] The concentration of phosphatidylethanolamine (PE) (p-34:3), for example, has been shown to increase when TNF-α is knocked down, and indeed, we observe a clear increase in the signal of this lipid (Figure 2.2d). Likewise, the concentration of ceramide (Cer) (d18:1/20:0) decreases upon TNF-α knockdown, and we observe the same effect in our MALDI-MSI data (Figure 2.2e). Other lipids, such as PC (34:2), were
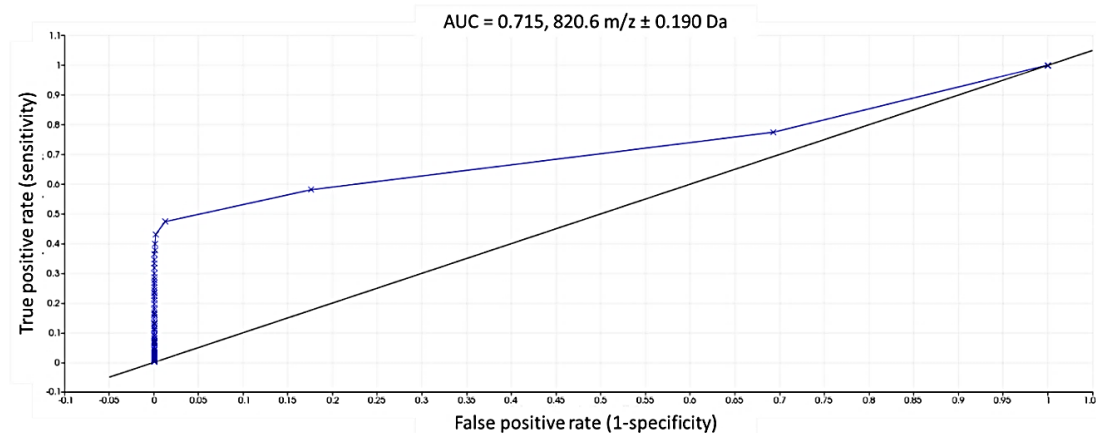
Figure 2.3 Acquired ROC curve for m/z 820.6 (PC (p-40:5) + H$^+$). An ROC AUC of 0.715 indicates that m/z 820.6 is significantly different in intensity between the control and NPSC-injected mouse tissues.

29
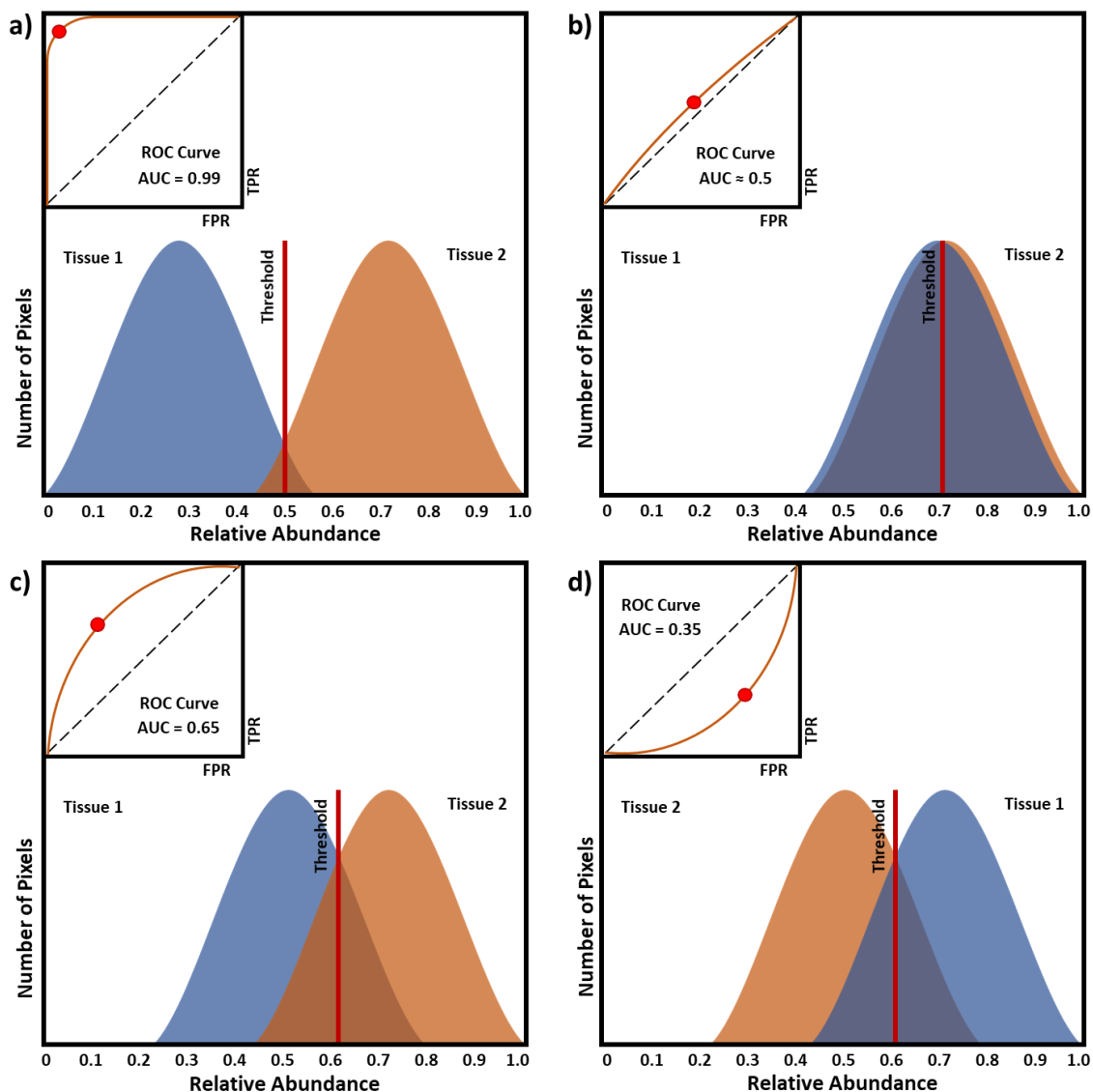
Figure 2.4. Example ROC curves for theoretical data, illustrating the statistical meaning of the area under the curve (AUC) values. Tissue 1 and 2 are arbitrarily selected; for our analyses, "Tissue 1" represents the control tissue and "Tissue 2" represents the NPSC-treated tissue. The Gaussians represent the signal abundance distributions for each tissue type (x-axis) at a selected m/z value. The y-axis represents the number of pixels found at each abundance threshold. For example, in (a) if the threshold is set to 50% relative abundance, there are approximately half of the total pixels correlated to Tissue 1 below the threshold and half of the total pixels correlated to Tissue 2 above the threshold, making this particular m/z value is a successful classifier for the two tissue types. In (b), at a threshold of 70% relative abundance, there are almost an equal number of pixels correlated to Tissue 1 and Tissue 2 both above and below the threshold, indicating that this m/z value is not a viable classifier for the two tissue types. The ROC curve is formed by plotting the coordinates for the true positive rates (TPR) (i.e. the number of Tissue 2 pixels found above the threshold, divided by the total number of Tissue 2 pixels) versus the false positive rates (FPR) (i.e. the number of Tissue 1 pixels found above the threshold, divided by the total number of Tissue 1 pixels)

30

for every threshold (red line in each graph) across the relative signal abundancies ranging from 0% to 100% Each point on an ROC curve is the result of the FPR vs. TPR for each set threshold point. The area under the ROC curve (AUC) that results from this analysis is used to assess the validity of the m/z as a distinctive biomarker between the two tissue types. (a) For tissues with distinguishable Gaussian distributions, the false positive rate (FPR) will remain low as the true positive rate (TPR) increases because there is very little overlap in their relative abundancies. An ROC AUC close to 1 indicates that a given m/z value is able to successfully classify Tissue 2 when compared to Tissue 1. (b) An ROC AUC close to 0.5 indicates that the m/z value is not able to distinguish Tissue 2 from Tissue 1 and cannot be used as a binary classifier. (c) An ROC AUC greater than 0.65 typically indicates that the abundance distribution of a given m/z value is significantly increased in Tissue 2 as compared to Tissue 1. (d) An ROC AUC less than 0.35 typically indicates that the abundance distribution of a given m/z value is significantly decreased in Tissue 2 as compared to Tissue 1.
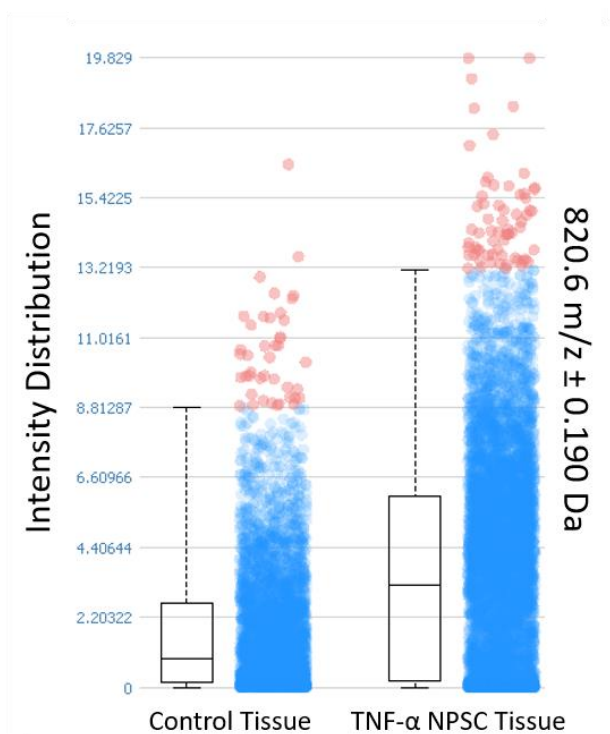
Figure 2.5. Example ion abundance box-and-whisker plot of m/z 820.6 (PC (p-40:5) + H$^+$). The highest and lowest bars represent the maximum distribution, while the upper, middle, and lower lines of the box represent first quartile, median, and third quartile, respectively. Analytes that have greater medians for NPSC-injected mice were considered significantly different.
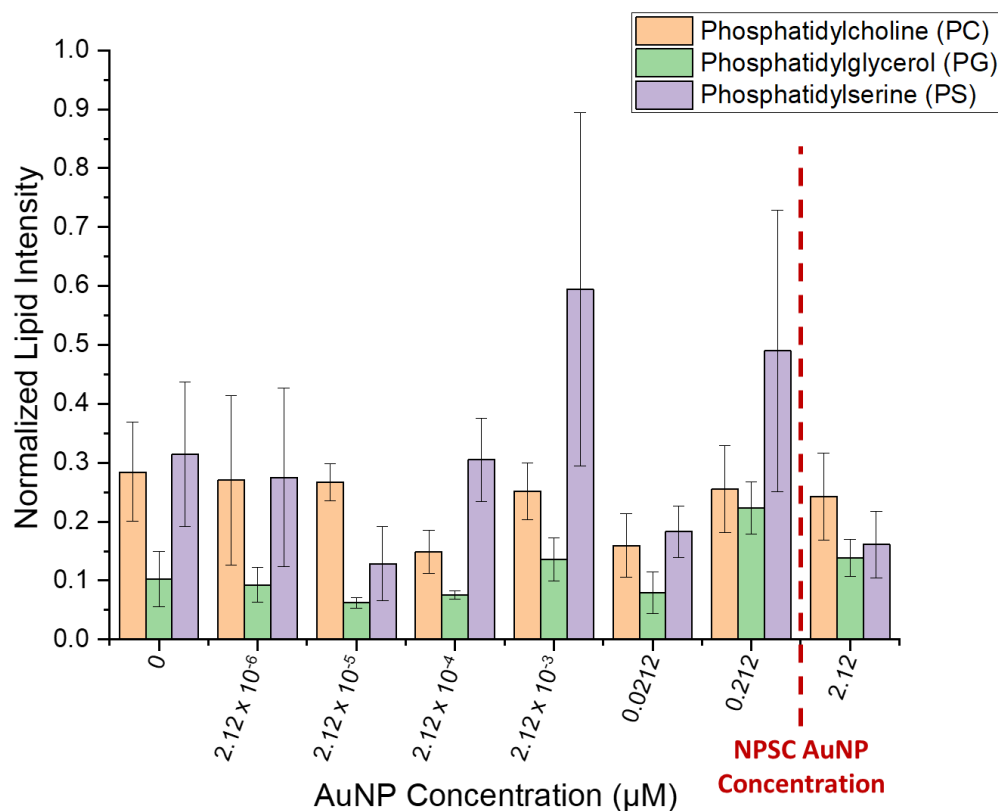
Figure 2.6. MALDI-MS signal of lipids in the presence of AuNPs. Representative lipids of different polarities (positive – PC; neutral – PG; negative – PS) were measured in combination with DHB as a matrix and increasing concentrations of AuNPs. Lipid intensities were normalized to the intensity of the $[M+H]^+$ peak of the DHB matrix in each spectrum. Each lipid intensity was calculated from the average of ten measurements acquired from three sample replicates. Error bars represent the standard deviation of 30 measurements. AuNP concentration was calculated by dividing Au concentrations (measured by ICP-MS) by the average number of Au atoms in each NP (~200).[97] Even at AuNP concentrations 10-fold higher than those detected in NPSC spleen tissue (represented by the red line at ~600 nM, calculated from Table S1) the particles did not significantly affect lipid ionization, suggesting that all lipid level increases are unrelated to the presence of AuNPs.

not expected to change, and that is what we observe (Figure 2.2c). Of the remaining 11

lipids that do not respond as expected (e.g. PC (32:0), LPC p-18:0, and PE p-34:2 in Figure

2.7), their changes could be due to relatively low signal, differences between spleen and

serum biochemistry, or the NPSC carrier itself.

To validate that our imaging method successfully monitors lipid changes caused by

TNF-α knockdown from the NPSC injection, we also imaged tissues from mice injected
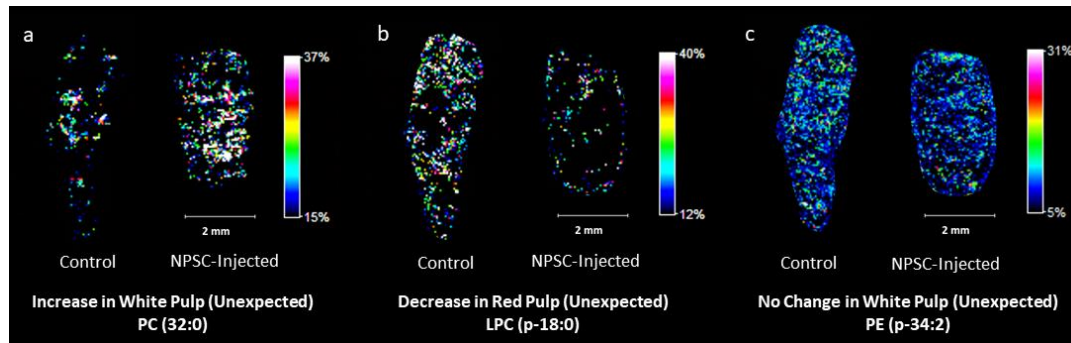
Figure 2.7. Example images of lipids that exhibit unexpected changes between the NPSC-injected mouse spleen (in the right of each image set) compared to the control tissue (in the left of each image set).[98] Panel (a) represents an unexpected increase, (b) an unexpected decrease, and (c) and unexpected lack of change between tissues types.

with NPSCs containing scrambled siRNA that does not knock-down TNF-α. Of the detected lipids in the scrambled siRNA experiments, only eight change in a manner predicted for TNF-α knockdown (Table 2.3), as opposed to the 33 observed to change in the NPSCs with siRNA specific for TNF-α. A majority of the lipids have no significant changes between control mice and those injected with scrambled siRNA containing NPSCs (Table 2.3 & Figure 2.8). This control experiment indicates that the lipid changes observed after injecting the NPSCs with TNF-α specific siRNA (Table 2.2) are caused by TNF-α knockdown. The differences in lipid signals after TNF-α knockdown also highlight the fact that the AuNPs themselves are not influencing lipid signal as the total amount of gold in the spleen is comparable for mice injected with the TNF-α specific NPSCs and those injected with scrambled siRNA (Table 2.1). Interestingly, five of the 11 unexpected lipid changes that are observed upon TNF-α knockdown are also observed in the mice treated with scrambled siRNA, perhaps suggesting that the NPSC carrier itself is causing a biochemical response in the spleen tissue. The origin of these lipid changes will be further explored in future experiments.

Table 2.3. Characteristic lipid ions in the spleen of scrambled NPSC-injected mice.

Lipid I.D.[a]	Detected m/z	Ion(s)	(+) or (-) in Scrambled NPSC-Injected Mouse Tissue	ROC AUC[c]	Change a Predicted Increase/Decrease for TNF NPSCs?
LPC (16:0)	496.3 518.4	[M + H+] [M + Na+]	None	0.484 0.542	No
LPC (18:0)	524.4	[M + H+]	None	0.515	No
LPC (p-18:0)	508.6	[M + H+]	-	-	N/A
LPC (18:2)	520.2	[M + H+]	None	0.553	No
LPC (20:4)	544.3	[M + H+]	None	0.488	No
PC (30:0)	706.6	[M + H+]	None	0.515	No
PC (32:0)	734.5 772.5	[M + H+] [M + K+]	None	0.590 0.504	No
PC (p-32:0)	756.5	[M + Na+]	(+)	0.652	Yes
PC (34:0)	762.6	[M + H+]	(+)	0.773	Yes
PC (p-34:0)	746.6	[M + H+]	(+)	0.686	Yes
PC (34:1)	760.6 798.6	[M + H+] [M + K+]	None	0.501	No
PC (p-34:1)	744.6	[M + H+]	(+)	0.683	No
PC (34:2)	780.5	[M + Na+]	None	0.478	No
PC (34:3)	756.6	[M + H+]	(+)	0.682	No
PC (p-36:5)	786.6 802.5	[M + Na+] [M + K+]	None	0.482 0.604	No
PC (p-36:4)	788.6 804.5	[M + Na+] [M + K+]	(+)	0.689 0.688	Yes
PC (p-36:2)	770.6 792.6 808.5	[M + H+] [M + Na+] [M + K+]	None	N/A N/A 0.510	No
PC (36:0)[d]	790.6 812.6 828.5	[M + H+] [M + Na+] [M + K+]	(+)	0.785 0.708 0.652	Yes
PC (p-38:6)[d]	790.6 812.6 828.5	[M + H+] [M + Na+] [M + K+]	(+)	0.785 0.708 0.652	Yes
PC (p-38:5)	792.5 830.5	[M + H+] [M + K+]	None	N/A 0.490	No
PC (p-38:4)	794.7 816.6 832.5	[M + H+] [M + Na+] [M + K+]	-	-	N/A
PC (p-40:5)	820.6 858.6	[M + H+], [M + K+]	None	0.426	No
2H OH Cer (d18:1/20:0)	632.5 650.5	[M – H2O + K+] [M + K+]	None	0.575 0.437	No

2H Cer (d18:1/25:1)	681.7	[M + NH$_4$$^+$]	None	0.527	No
2H Cer (d18:1/20:1)	632.5	[M + K$^+$]	None	0.565	No
SM (d18:1/17:0)	741.6 757.6	[M + Na$^+$] [M + K$^+$]	None	0.479 0.635	No
SM (d18:1/20:0)	759.6	[M + H$^+$]	None	0.627	No
SM (d18:1/21:1)	771.6 809.6	[M + H$^+$] [M + K$^+$]	(+)	0.689 0.673	Yes
SM (d18:1/23:2)	819.6	[M + Na$^+$]	None	0.627	No
SM (d18:1/24:0)	853.7	[M + K$^+$]	-	-	N/A
SM (d18:1/24:3)	809.6 847.6	[M + H$^+$] [M + K$^+$]	(+)	0.798 0.777	No
PE (26:4)	497.2	[M – HG + K$^+$]	(+)	0.669	Yes
PE (p-34:3)	557.5	[M – HG + H$^+$]	None	0.531	No
PE (p-34:2)	559.5 581.5	[M – HG + H$^+$] [M – HG + Na$^+$]	None	N/A 0.583	No
PE (p-34:1)^d	583.5	[M – HG + H$^+$]	None	0.468	No
PE (p-36:4)^d	583.5	[M – HG + Na$^+$]	None	0.468	No
PE (p-34:1)	732.5	[M + H$^+$]	None	0.523	No
PE (p-36:4)	724.5	[M + Na$^+$]	None	0.469	No
PE (p-36:3)	585.5	[M – HG + H$^+$]	None	0.626	No
PE (38:2)	669.5	[M – HG + K$^+$]	-	-	N/A
PE (38:1)^d	671.5	[M – HG + K$^+$]	None	0.583	No
PE (p-40:5)^d	671.5	[M – HG + K$^+$]	None	0.583	No
CAR (16:0)	400.4	[M + H$^+$]	None	0.508	No
CAR (18:1)	426.6	[M + H$^+$]	None	0.420	No

While lipid levels largely correspond with previous results, completely new information is obtained about the locations of these lipid level changes, highlighting the value of MALDI-MSI. MALDI-MSI of heme B distributions (Figure 2.9) allow us to readily distinguish between the red pulp and white pulp of the spleen, which are sub-organ regions that were confirmed by traditional histology (Figure 2.10). Heme B signals, which are a proxy for hemoglobin, are high in the vascularized red pulp and very low in the immune-cell rich white pulp. The sub-organ distributions of the measured lipid changes

35

provide new insight about the cell types that undergo changes upon TNF-α knockdown. The levels of 26 of the 44 lipids increase in the NPSC-treated mice (Table 2.2), and the vast majority (77%) of these increases are found in the white pulp (e.g. Figure 2.9a).

Of the 8 lipids that show no change in abundance, 63% of these are in the white pulp (e.g. Figure 2.9c and 2.9f). In contrast, of the 10 lipids that decrease in abundance, only 30% of these are found exclusively in the white pulp as illustrated in Figure 2.9b. More interestingly, of the 33 lipids that respond to TNF-α as predicted, 79% of these responses occur exclusively in the white pulp, whereas 15% occur in the red pulp (e.g. Figures 2.9d & 2.9e) and 6% occur in both regions. This prevalence of lipid level changes in the white
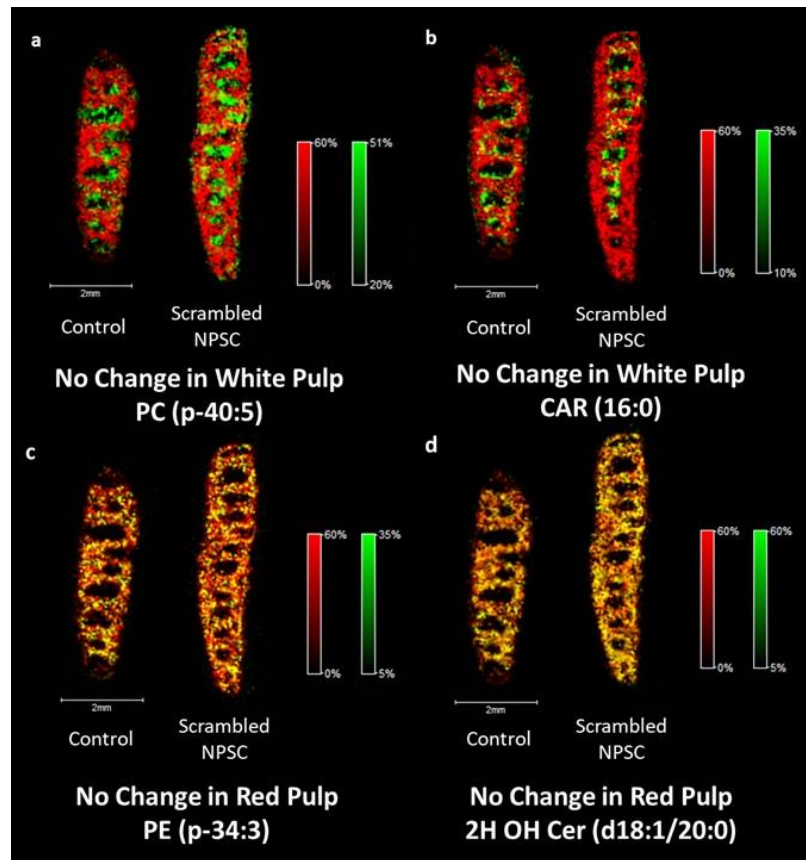
Figure 2.8. Example images for scrambled siRNA NPSC-injected mouse spleen tissues. The same lipids that exhibit changes between the TNF-α siRNA NPSC-injected mouse spleen compared to the control tissue in Figure 2 & 3, exhibit no changes between the scrambled siRNA NPSC-injected mouse spleen (in the right of each image set) compared to the control (in the left of each image set).
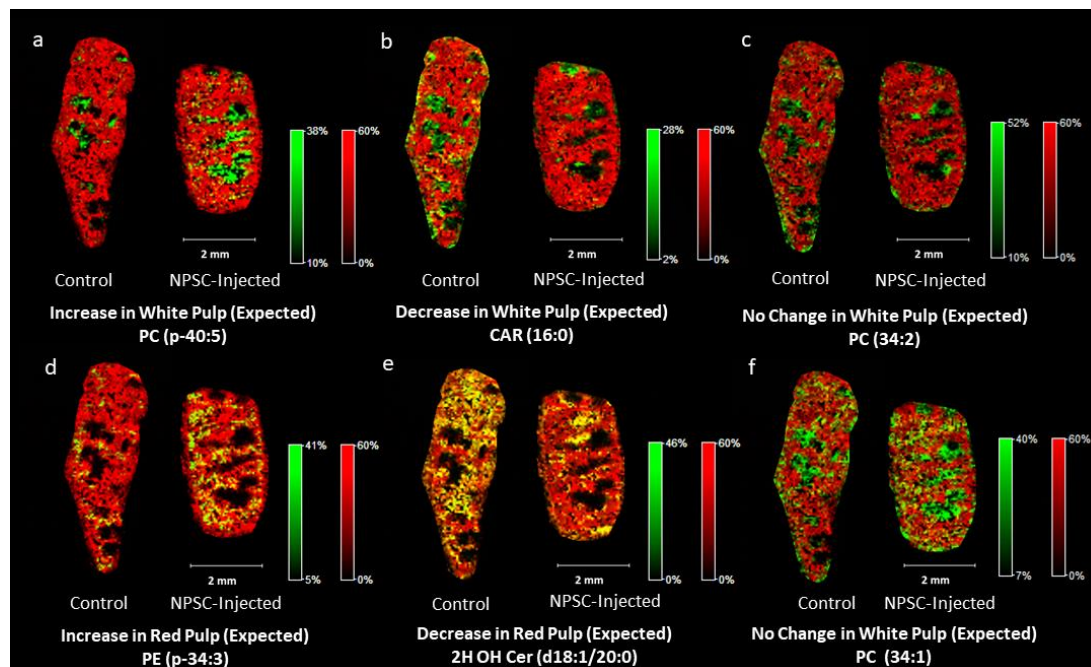
Figure 2.9. Example images of lipid responses in NPSC-injected mouse spleen tissues (right in each image pair) compared to control tissues (left in each image pair) with heme B overlays to determine sub-organ distribution. Heme B is indicated by red. Regions of high co-localization between the lipid and heme signals appear in yellow, whereas those with low or no co-localization appear in green. Panels (a), (b), (c), and (f) are example images of lipids that respond to the NPSCs in the white pulp of the spleen tissues, as indicated by their intense green color. In panel (f), only 22% of the control tissue lipids and 23% of the NPSC-injected lipids overlap with the heme peaks. Panels (d) and (e) are example images of lipids that respond to NPSCs in the red pulp of the spleen as indicated by their intense yellow color. In panel (d), 76% of the control tissue lipids and 85% of the NPSC-injected tissue lipids overlap with the heme peaks. In panel (e), 76% of the control tissue lipids and 71% of the NPSC-injected tissue lipids overlap with the heme peaks.

pulp likely reflects the fact that TNF-α is produced by immune-related macrophages, which are a primary component of the white pulp. Of the 11 lipids that do not respond to TNF-α knockdown as expected, only two are exclusively found in the white pulp, whereas the remainder are found in the red pulp or both regions (Figure 2.11). Together, these data provide new sub-organ locational information about lipid responses to TNF-α knockdown and hint at other intriguing changes that occur when TNF-α knockdown is accomplished using nano-based delivery agents.
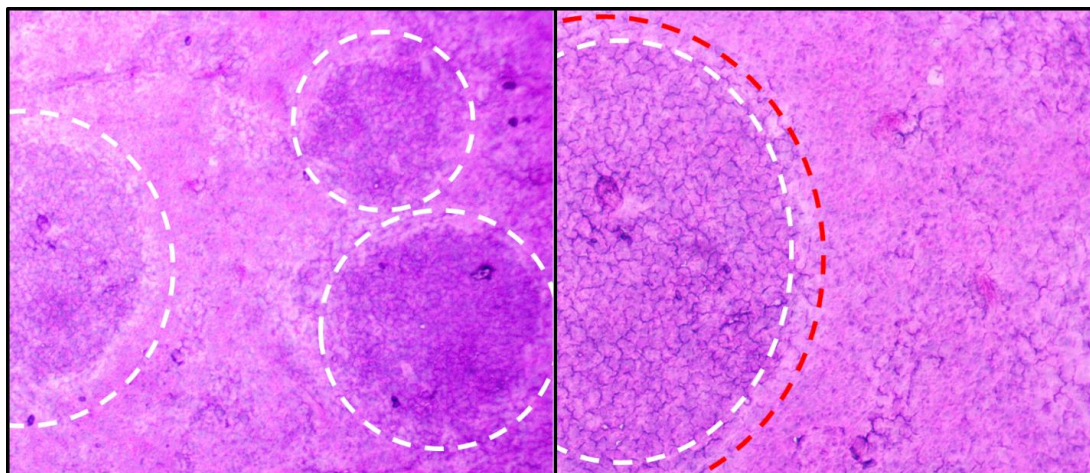
Figure 2.10. H&E stain of a mouse spleen tissue, indicating red and white pulp regions. The figure on the left is a representative image of the red and white pulp of a spleen. The white pulp regions are circled in a white dotted outline and the red pulp is the region outside of the dotted lines. The figure on the right is a zoomed in portion of the same spleen tissue shown on the left. The white dotted outline is representative of the white pulp. The region between the red and white dotted outline is the marginal zone. Everything outside of the red dotted line is the red pulp.
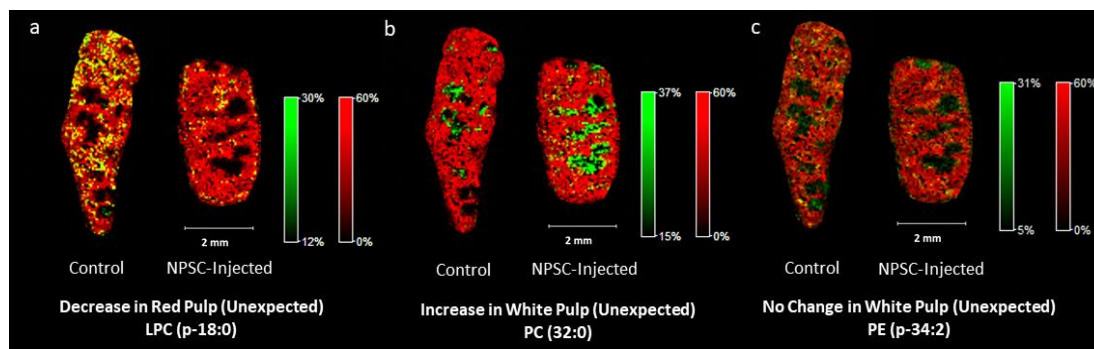
Figure 2.11. Example images of lipid responses in NPSC-injected mouse spleen tissues (right in each image pair) compared to control tissues (left in each image pair) with heme B overlays to determine sub-organ distribution. Heme B is indicated by red. Regions of high co-localization between the lipid and heme signals appear in yellow, whereas with low or no co-localization appear in green. Panel (a) is a representative image of lipids that respond to NPSCs in the red pulp of the spleen as indicated by the intense yellow color. In panel (a), 76% of control lipids and 72% of NPSC-injected lipids were colocalized with the heme peaks.

2.2.2 LA-ICP-MS imaging of spleen tissues from control mice and mice injected with NPSCs

To determine whether the observed lipid changes are systemic or co-localized with regions of NPSC accumulation, we also measured the distribution of gold in the tissue

slices using LA-ICP-MSI. Previous work from our group has shown that AuNPs similar to those present in the NPSCs are stable for up to 48 h *in vivo* and in spleen tissues,[16,17,39,40] making gold a good marker for these nanomaterials. A spleen tissue slice, immediately adjacent to the one used for MALDI-MSI analysis, was used for LA-ICP-MSI analysis. Fe levels in LA-ICP-MS images provide a convenient means of distinguishing between the red and white pulp regions of the spleen because blood flow is very different in these regions (Figure 2.12). When the LA-ICP-MS images of Fe and Au are overlaid, we find that Au is primarily found in the red pulp (Figure 2.12). When the Au and Fe levels are considered on a pixel-by-pixel basis, we find that about 90% of the Au is found in the red pulp. This distribution of Au is similar to what was found in previous LA-ICP-MS imaging results for AuNPs with positively-charged surface coatings.[16,17,39]
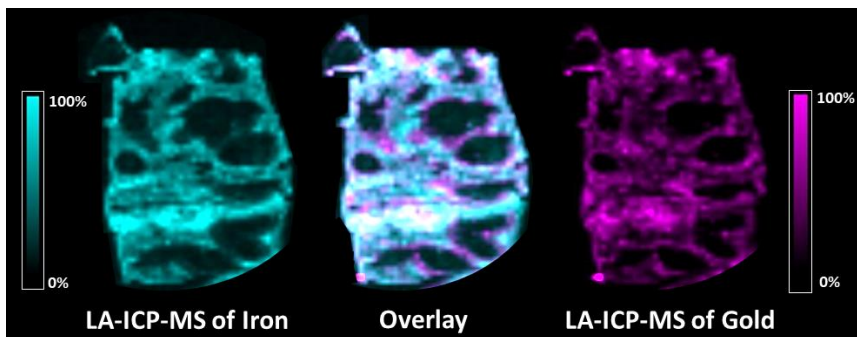
Figure 2.12. LA-ICP-MS images showing the distributions of iron (left) and gold (right) in a spleen tissue slice from an NPSC-injected mouse. The overlaid image (center) contains 83% co-registered (white) pixels, indicating that gold is primarily distributed in the red pulp region of the spleen where iron signals are high.

Because the majority of Fe in blood is associated with hemoglobin, Fe distributions in LA-ICP-MS images can be correlated with heme distributions from MALDI-MSI images, enabling an overlay of images from the two modalities (Figure 2.13). Such correlations allow us to compare the distributions of Au and lipid signals to determine if the lipid changes co-localize with the NPSCs. From these comparisons, we find that the majority of lipid changes occur in regions that have low gold concentrations. As an example, the
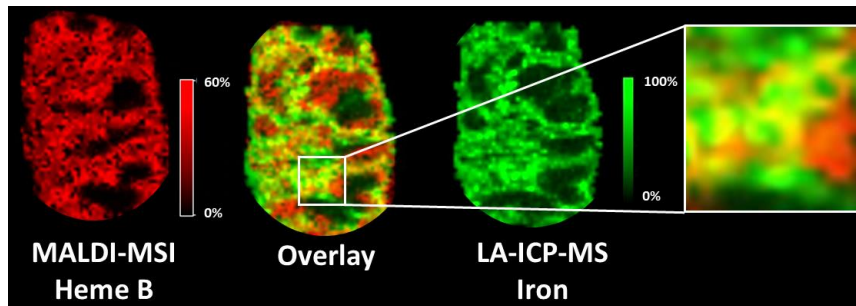
Figure 2.13. LA-ICP-MSI and MALDI-MSI image overlays of iron and heme B distributions to correlate the two imaging modalities. These analytes are markers for hemoglobin, which has a high concentration in the vascularized red pulp of the spleen. In the overlaid images, 70% of the signal pixels are yellow, indicating the expected high co-localization of iron and heme B in the red pulp.

distribution of the lipid PC (36:0) has minimal overlap with the gold distribution (Figure 2.14). Indeed, as indicated earlier, almost 80% of the predicted lipid changes occur in the white pulp where the gold content is almost 10-fold lower than in the red pulp. In many cases, predicted lipid changes that do occur in the red pulp, such as PE (p-34:3), also appear not to be dependent on gold levels, based on the poor overlap of lipid signal increases and Au signals (Figure 2.15). These observations suggest that the TNF-α-induced lipid changes are systemic and are not occurring where the NPSCs ultimately localize. This systemic effect likely arises because the NPSCs circulate for 48 h before the mice are sacrificed, providing ample time for siRNA to result in TNF-α knock-down and cause the observed changes in lipid levels. The ability to draw correlations between nanomaterial location and
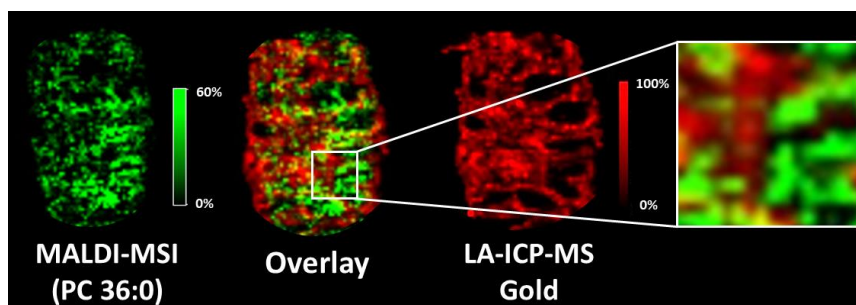
Figure 2.14. MALDI-MSI and LA-ICP-MSI image overlays of a lipid (i.e. PC 36:0) that changes upon NPSC injection and gold from the NPSCs, illustrating that the lipid changes occur in regions low in gold. In the overlaid images, only 34% of the signal pixels are yellow, indicating relatively how co-localization between the lipid of interest and gold.
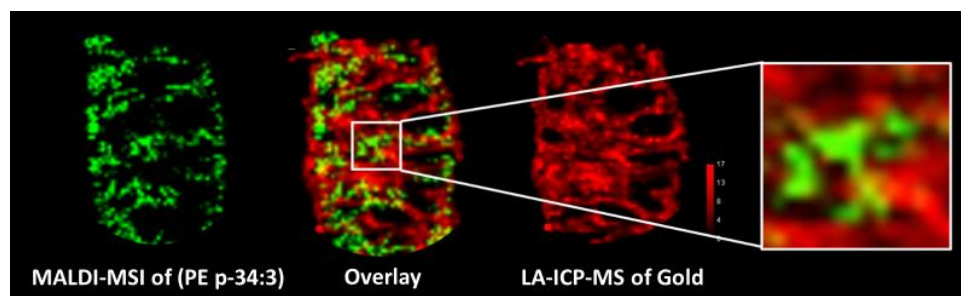
Figure 2.15. MALDI-MSI and LA-ICP-MSI overlays of a lipid that is primarily in the red pulp and gold. The low number of yellow pixels indicates that the gold increases are not correlated with the lipid increases in the red pulp.

the resulting biochemical effect is uniquely possible with the combined imaging approach described here.

Another important feature of combining the two imaging modalities is that we obtain intriguing site-specific information about lipids that do not change as predicted upon TNF-α knockdown. Of the 11 lipids whose levels change in an unexpected fashion, seven exclusively undergo changes in the red pulp, which has high concentrations of NPSCs (Figure 2.11a), and two more undergo changes in the red and white pulp. When These observations suggest that the unexpected changes may arise from the presence of the NPSCs themselves. Future work will seek to further understand these biochemical changes by evaluating the inflammatory properties/effects of the NPSC carrier components themselves.

2.3 Conclusions

We have developed a powerful method to monitor and correlate the sub-organ distributions of a NP-based delivery system and its cargo-induced biochemical effects. Our approach relies on LA-ICP-MSI to track the inorganic components of a nano-based delivery system and MALDI-MS to examine changes in biochemistry caused by the delivery system. When the two imaging modalities are used together, we are able to

evaluate if the biochemical effects are localized with the delivery vehicle or occur more diffusively. A key feature of our described approach utilizes the strong correlation between Fe signals in LA-ICP-MS and heme signals in MALDI-MS that allow images from the two modalities to be overlaid and directly compared. Upon using this new approach to image spleen tissues from mice injected with TNF-α siRNA-bearing NPSCs, we also obtain new biological information. Specifically, we observe that changes in the lipidome that occur with decreased TNF-α levels are primarily localized in the white pulp of the spleen. In addition, we find that several lipids have unexpected changes in their abundances, the vast majority of which occur in the red pulp where concentrations of NPSCs are highest, suggesting that changes to these lipids are caused by the NPSCs themselves. Control experiments with NPSCs containing scrambled siRNA are consistent with the NPSCs themselves having an effect on lipid levels. Future work will investigate how the individual components of the NPSCs influence lipid levels. We predict that the dual-mode imaging approach described here will be beneficial for the development of nano-based drug delivery systems by providing access to sub-organ biodistributions for carriers and their biochemical effect. Such information should facilitate the design of systems that target desired tissues while minimizing unwanted side effects.

2.4 Experimental

2.4.1 Chemicals and Materials.

2,5-dihydroxybenzoic acid (DHB), arginine, 1-pentanthiol, and linoleic acid were purchased from Sigma-Aldrich (St. Louis, MO). Chloroauric acid for gold nanoparticle synthesis was bought from Strem Chemicals Inc. (Newburyport, MA). siRNA targeting TNF-α with the sequence: 5′-GUCUCAGCCUCUUCUCAUUCCUGct-3′ (sense strand)

was synthesized by Sigma-Aldrich. Scramble siRNA with the sequence: 5′-UUCUCCGAACGUGUCACGU-3′ (sense strand) was purchased from Life Technologies (Carlsbad, CA). Phosphate-buffered saline (PBS) was purchased from Fisher Scientific. Indium tin oxide (ITO) conductive slides were purchased from Delta Technologies (Loveland, CO). All other chemicals were purchased from Sigma-Aldrich or Fisher Scientific and used as received unless otherwise specified.

2.4.2 Nanoparticle and Nanocapsule Synthesis

Arginine-functionalized AuNPs (Arg-AuNPs) and NPSCs were synthesized according to a previous report.[11] In brief, 1-pentanethiol protected AuNPs (Au-C5) with ~2 nm core diameters were synthesized using the Brust-Sciffrin two-phase synthesis.[41] Arginine-functionalized thiol ligands were synthesized based on a previous report.[42] They were then conjugated to the AuNP core by the Murray place-exchange method.[43] To form the NPSCs, 1 µL linoleic acid was combined with 1 µM Arg-AuNPs in PBS. Emulsions were formed by using an amalgamator at 5000 rpm for 100 s. 10 µL of the emulsion was combined with a mixture of 2.5 µM Arg-AuNPs and 1 µM siRNA (90 µL in 5 mM phosphate buffer). The mixture was incubated for 10 min at room temperature.

2.4.3 Mouse Experiments

All animal protocols were approved by the University of Massachusetts Amherst Institutional Animal Care and Use Committee (IACUC), which is guided by the U.S. Animal Welfare Act and U.S. Public Health Service Policy. Female Balb/c mice (8-week-old) were obtained from Charles River Laboratories, Inc. (Wilmington, MA) and housed in controlled climates (22 ± 2 °C temperature, 12 h light/dark daily cycle) with free access to food and water. The mice were randomly divided into control and treated groups. Each

was injected with 200 µL of either PBS or 2.5 µM of NPSCs via the tail vein. After 48 h, mice were sacrificed via carbon dioxide inhalation and cervical dislocation. Mouse tissues were immediately extracted, flash frozen in liquid nitrogen, and then kept at -80 °C until used for MS imaging. Using a LEICA CM1850 cryostat, flash-frozen spleen tissues were sliced to 12 µm, thaw-mounted onto ITO slides (MALDI-MS) or glass slides (LA-ICP-MS) and desiccated under vacuum for 1 h. For the MALDI-MS imaging experiments, a Bruker ImagePrep apparatus was used to spray a 25 mg/mL 2,5-DHB solution (1:1 methanol:water) onto the tissues.

2.4.4 MALDI Imaging

MALDI-MS imaging experiments were conducted on a Bruker ultrafleXtreme MALDI-TOF/TOF at 50 µm resolution. The laser offset was set to 60%. All experiments were performed on at least three different sets of tissue sections to ensure reproducibility. MS/MS experiments were conducted using the LIFT cell with collision-induced dissociation. Compound identification was performed using MS/MS and/or accurate m/z measurements after internal standard alignment post-acquisition. Internal standards of m/z 273.04 (2DHB − 2H_2O + H^+) and m/z 772.57 (PC (32:0) + K^+) were used.

2.4.5 LA-ICP-MS Imaging

LA-ICP-MS experiments were conducted on a PerkinElmer NEXION 300 ICP-MS using a Teledyne CETAC LSX-213 G2 laser ablation system attached to the ICP-MS via Teflon tubing. Tissues were ablated via line scanning with a spot size of 50 µm, scan rate of 15 µm/s, 10 Hz laser frequency, 10 seconds of shutter delay, and a carrier He gas flow of 0.6 L/min. Images were reconstructed, as described in our previous work,[16,17] by performing data reduction to produce an image with 50 µm resolution. In short, raw data
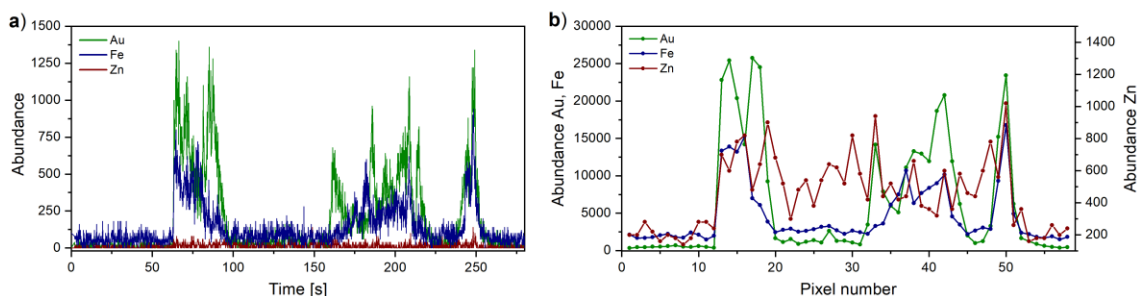
Figure 2.16. Data reduction process to produce pixels for each line of data obtained from LA-ICP-MS experiments. (a) Example raw LA-ICP-MS data for gold (Au), iron (Fe), and zinc (Zn) obtained from a single line scan of the tissue of interest, with the indicated time representing the time after the 15 µm/s laser scan begins. (b) The raw data is converted into pixelated data by binning 33 data points to generate a single 50 µm x 50 µm pixel, as represented by each data point. Tissue edges can be identified by the shift from noise to signal at ~60 seconds and the shift from signal to noise at ~260 seconds.

were binned into pixelated data by averaging the 33 data points needed to create a single 50 x 50 µm pixel (see Figure 2.16 for details and Figure 2.17 for an example). These raw data were analyzed and reconstructed using a custom script written in Python. Because the zinc signal is relatively constant throughout spleen tissues (e.g. Figures 2.16 & 2.17), each metal of interest (i.e. iron, gold) was normalized to zinc distributions to account for folds or tears in the tissues that could give rise to "hot spots."

2.4.6 Pixel Counting and Analysis for Overlaid Images

All overlaid images (Figures 2.8, 2.9, 2.11-2.15) were uploaded to ImageJ where they were converted into their RGB components. Each filter (red, green blue) was then converted into a text file. On an RGB scale of 0-255, we found that the background cutoff was at 40 for all tissues at all filters, based on the intensity of the pixel regions that were clearly located outside of the tissue area. Therefore, signals were found to be within the 40-255 region for every filter. Each individual red pixel was then multiplied by each individual green pixel to produce the results for the yellow overlay (red x green = yellow). To determine the number of pixels that were overlaid in yellow we counted those with a
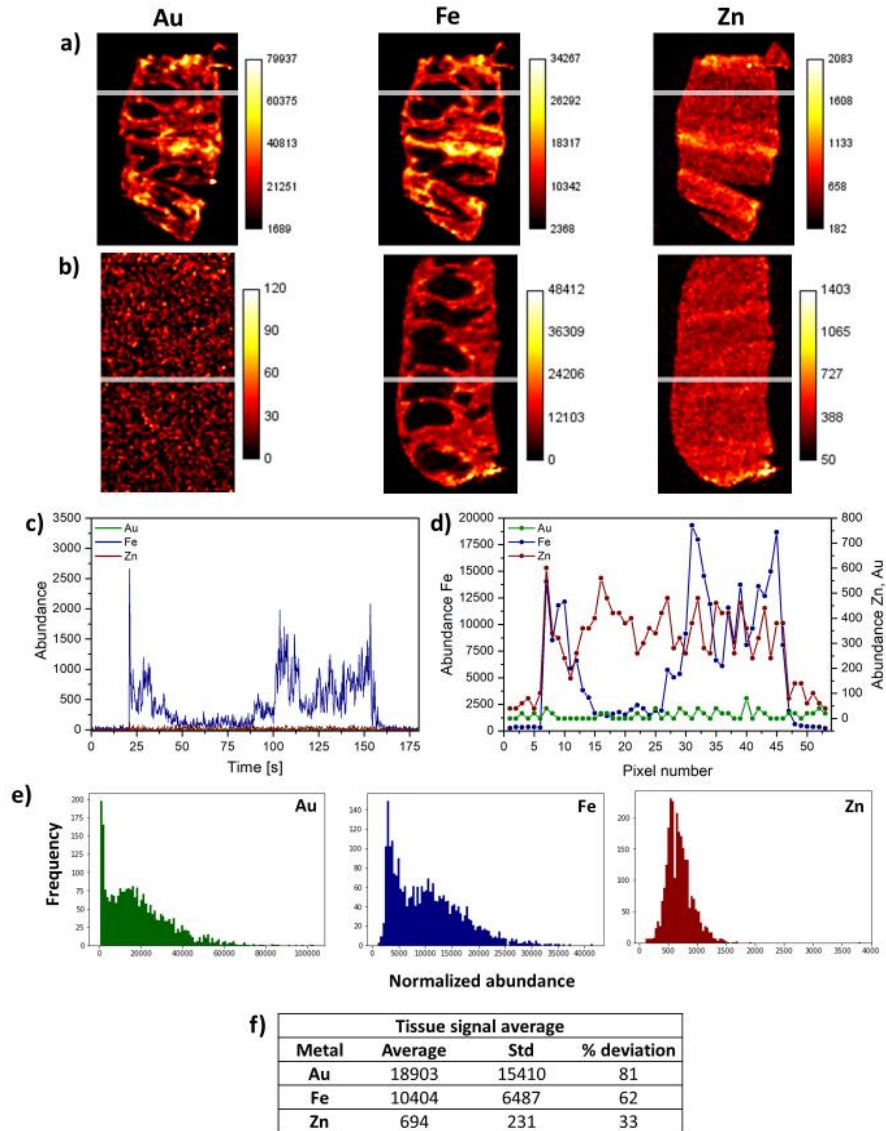
Figure 2.17. LA-ICP-MS image generation and signal analysis for NPSC-injected and control mouse spleen. Raw images obtained for Au, Fe, and Zn for (a) NPSC-injected and (b) control mouse spleen tissues were generated using the method described in the main text and in Figure S-1. (c) Example raw data for the line indicated in the control tissue shown in (b), displaying the signals for Au, Fe, and Zn as function of time after beginning the laser scan. (d) Example binned data from the same control tissue in (c). It can be seen from the abundances of elements in both Figures 2.16 and (c & d) that Zn remains relatively constant over the entirety of the tissue. (e) Example histograms for the intensity distributions for Au, Fe, and Zn throughout the entire tissue for the NPSC-injected tissue slice shown in (a). Au and Fe both have two broad distributions, whereas Zn only has one narrow one, which is consistent with it having a relatively constant distribution across the tissue. (f) Averages and standard deviations for the Au, Fe, and Zn signals shown in (e).

46

value above the threshold of the background (40) times the highest possible intensity (255) for a minimum value of 10,200. The maximum was then set at 65,025 (255 x 255). Anything below the threshold of 10,200 was considered a non-colocalized pixel. The total number of yellow (overlaid) pixels were then divided by the number of red or green pixels, depending which was smaller (the smaller number of pixels is the greatest number of total pixels that could be overlapped between the two filters) to determine the percent of overlap between the analytes of interest.

2.4.7 Statistical Analysis

SCiLS Lab 2015b was used to determine significant differences between tissue images. Baseline subtraction was conducted using the TopHat method, which is an operator used in mathematical morphology for image analysis.[44] Baseline subtraction is followed by total ion count (TIC) normalization, peak picking, and discriminative value determination using both receiver operating characteristic (ROC) curves (Figure 2.4) and ion abundance box-and-whisker plots (Figure 2.5). ROC curves are used to assess the performance of particular m/z values as binary classifiers for comparative tissues. ROC curves of the pooled data from given images were used to identify significant changes in ion signals between control and treated tissues. An ROC area under the curve (AUC) threshold of greater than 0.65 or lower than 0.35 was used to identify significant differences between tissues (see Figures 2.16 & 2.17),[45–47] and differences for a given lipid are indicated if the AUC thresholds are surpassed for tissue images from three separate mice. Ion abundance box plots were also used in combination with ROCs to determine the degree of difference between pooled sets of data from given tissue images by comparing both the range and median points of the compared lipid peaks (Figure 2.5).

2.5 References

(1)   De, M.; Ghosh, P. S.; Rotello, V. M. Applications of Nanoparticles in Biology. *Adv. Mater.* **2008**, *20* (22), 4225–4241.

(2)   Dreaden, E. C.; Alkilany, A. M.; Huang, X.; Murphy, C. J.; El-Sayed, M. a. The Golden Age: Gold Nanoparticles for Biomedicine. *Chem. Soc. Rev.* **2012**, *41* (7), 2740.

(3)   Yu, X.; Trase, I.; Ren, M.; Duval, K.; Guo, X.; Chen, Z. Design of Nanoparticle-Based Carriers for Targeted Drug Delivery. *J. Nanomater.* **2016**, 1087250.

(4)   Kumar, B.; Jalodia, K.; Kumar, P.; Gautam, H. K. Recent Advances in Nanoparticle-Mediated Drug Delivery. *J. Drug Deliv. Sci. Technol.* **2017**, *41* (6), 260–268.

(5)   Liu, J.; Stace-Naughton, A.; Jiang, X.; Brinker, C. J. Porous Nanoparticle Supported Lipid Bilayers (Protocells) as Delivery Vehicles. *J. Am. Chem. Soc.* **2009**, *131* (4), 1354–1355.

(6)   Rodenak-Kladniew, B.; Islan, G. A.; de Bravo, M. G.; Durán, N.; Castro, G. R. Design, Characterization and in Vitro Evaluation of Linalool-Loaded Solid Lipid Nanoparticles as Potent Tool in Cancer Therapy. *Colloids Surfaces B Biointerfaces* **2017**, *154*, 123–132.

(7)   Jiang, Y.; Hardie, J.; Liu, Y.; Ray, M.; Luo, X.; Das, R.; Landis, R. F.; Farkas, M. E.; Rotello, V. M. Nanocapsule-Mediated Cytosolic SiRNA Delivery for Anti-Inflammatory Treatment. *J. Control. Release* **2018**, *283* (May), 235–240.

(8)   Abrams, M. T.; Koser, M. L.; Seitzer, J.; Williams, S. C.; Dipietro, M. A.; Wang, W.; Shaw, A. W.; Mao, X.; Jadhav, V.; Davide, J. P.; et al. Evaluation of Efficacy, Biodistribution, and Inflammation for a Potent SiRNA Nanoparticle: Effect of Dexamethasone Co-Treatment. *Mol. Ther.* **2010**, *18* (1), 171–180.

(9)   Whitehead, K. A.; Langer, R.; Anderson, D. G. Knocking down Barriers: Advances in SiRNA Delivery. *Nat. Rev. Drug Discov.* **2009**, *8* (2), 129–138.

(10)   Hofmann, D.; Messerschmidt, C.; Bannwarth, M. B.; Landfester, K.; Mailänder, V. Drug Delivery without Nanoparticle Uptake: Delivery by a Kiss-and-Run Mechanism on the Cell Membrane. *Chem. Commun.* **2014**, *50* (11), 1369–1371.

(11)   Yang, X. C.; Samanta, B.; Agasti, S. S.; Jeong, Y.; Zhu, Z. J.; Rana, S.; Miranda, O. R.; Rotello, V. M. Drug Delivery Using Nanoparticle-Stabilized Nanocapsules. *Angew. Chem. Int. Ed.* **2011**, *50* (2), 477–481.

(12)   Tang, R.; Kim, C. S.; Solfiell, D. J.; Rana, S.; Mout, R.; Velázquez-Delgado, E. M.; Chompoosor, A.; Jeong, Y.; Yan, B.; Zhu, Z. J.; et al. Direct Delivery of Functional Proteins and Enzymes to the Cytosol Using Nanoparticle-Stabilized Nanocapsules. *ACS Nano* **2013**, *7* (8), 6667–6673.

(13)   Pacardo, D. B.; Ligler, F. S.; Gu, Z. Programmable Nanomedicine: Synergistic and Sequential Drug Delivery Systems. *Nanoscale* **2015**, *7* (8), 3381–3391.

(14) Hardie, J.; Jiang, Y.; Tetrault, E. R.; Ghazi, P. C.; Tonga, G. Y.; Farkas, M. E.; Rotello, V. M. Simultaneous Cytosolic Delivery of a Chemotherapeutic and SiRNA Using Nanoparticle-Stabilized Nanocapsules. *Nanotechnology* **2016**, *27* (37), 374001.

(15) Hofmann, D.; Tenzer, S.; Bannwarth, M. B.; Messerschmidt, C.; Glaser, S.-F.; Schild, H.; Landfester, K.; Mailänder, V. Mass Spectrometry and Imaging Analysis of Nanoparticle-Containing Vesicles Provide a Mechanistic Insight into Cellular Trafficking. *ACS Nano* **2014**, *8* (10), 10077–10088.

(16) Elci, S. G.; Yan, B.; Kim, S. T.; Saha, K.; Jiang, Y.; Klemmer, G. A.; Moyano, D. F.; Tonga, G. Y.; Rotello, V. M.; Vachet, R. W. Quantitative Imaging of 2 Nm Monolayer-Protected Gold Nanoparticle Distributions in Tissues Using Laser Ablation Inductively-Coupled Plasma Mass Spectrometry (LA-ICP-MS). *Analyst* **2016**, *141* (8), 2418–2425.

(17) Elci, S. G.; Jiang, Y.; Yan, B.; Kim, S. T.; Saha, K.; Moyano, D. F.; Yesilbag Tonga, G.; Jackson, L. C.; Rotello, V. M.; Vachet, R. W. Surface Charge Controls the Suborgan Biodistributions of Gold Nanoparticles. *ACS Nano* **2016**, *10* (5), 5536–5542.

(18) Svatoš, A. Mass Spectrometric Imaging of Small Molecules. *Trends Biotechnol.* **2010**, *28* (8), 425–434.

(19) Esquenazi, E.; Yang, Y. L.; Watrous, J.; Gerwick, W. H.; Dorrestein, P. C. Imaging Mass Spectrometry of Natural Products. *Nat. Prod. Rep.* **2009**, *26* (12), 1521–1534.

(20) Zemski Berry, K. A.; Hankin, J. A.; Barkley, R. M.; Spraggins, J. M.; Caprioli, R. M.; Murphy, R. C. MALDI Imaging of Lipid Biochemistry in Tissues by Mass Spectrometry. *Chem. Rev.* **2011**, *111* (10), 6491–6512.

(21) Stoeckli, M.; Staab, D.; Schweitzer, A. Compound and Metabolite Distribution Measured by MALDI Mass Spectrometric Imaging in Whole-Body Tissue Sections. *Int. J. Mass Spectrom.* **2007**, *260* (2–3), 195–202.

(22) Cillero-Pastor, B.; Heeren, R. M. A. Matrix-Assisted Laser Desorption Ionization Mass Spectrometry Imaging for Peptide and Protein Analyses: A Critical Review of On-Tissue Digestion. *J. Proteome Res.* **2014**, *13* (2), 325–335.

(23) Niehoff, A.-C.; Kettling, H.; Pirkl, A.; Chiang, Y. N.; Dreisewerd, K.; Yew, J. Y. Analysis of Drosophila Lipids by Matrix-Assisted Laser Desorption/Ionization Mass Spectrometric Imaging. *Anal. Chem.* **2014**, *86* (22), 11086–11092.

(24) Attia, A. S.; Schroeder, K. A.; Seeley, E. H.; Wilson, K. J.; Hammer, N. D.; Colvin, D. C.; Manier, M. L.; Nicklay, J. J.; Rose, K. L.; Gore, J. C.; et al. Monitoring the Inflammatory Response to Infection through the Integration of MALDI IMS and MRI. *Cell Host Microbe* **2012**, *11* (6), 664–673.

(25) Fülöp, A.; Sammour, D. A.; Erich, K.; Von Gerichten, J.; Van Hoogevest, P.; Sandhoff, R.; Hopf, C. Molecular Imaging of Brain Localization of Liposomes in Mice Using MALDI Mass Spectrometry. *Sci. Rep.* **2016**, *6*, 33791.

(26) Lukowski, J. K.; Weaver, E. M.; Hummon, A. B. Analyzing Liposomal Drug Delivery Systems in Three-Dimensional Cell Culture Models Using MALDI Imaging Mass Spectrometry. *Anal. Chem.* **2017**, *89* (16), 8453–8458.

(27) Drescher, D.; Giesen, C.; Traub, H.; Panne, U.; Kneipp, J.; Jakubowski, N. Quantitative Imaging of Gold and Silver Nanoparticles in Single Eukaryotic Cells by Laser Ablation ICP-MS. *Anal. Chem.* **2012**, *84* (22), 9684–9688.

(28) Böhme, S.; Stärk, H. J.; Kühnel, D.; Reemtsma, T. Exploring LA-ICP-MS as a Quantitative Imaging Technique to Study Nanoparticle Uptake in Daphnia Magna and Zebrafish (Danio Rerio) Embryos. *Anal. Bioanal. Chem.* **2015**, *407* (18), 5477–5485.

(29) Yan, B.; Zhu, Z. J.; Miranda, O. R.; Chompoosor, A.; Rotello, V. M.; Vachet, R. W. Laser Desorption/Ionization Mass Spectrometry Analysis of Monolayer-Protected Gold Nanoparticles. *Anal. Bioanal. Chem.* **2010**, *396* (3), 1025–1035.

(30) Yan, B.; Kim, S. T.; Kim, C. S.; Saha, K.; Moyano, D. F.; Xing, Y.; Jiang, Y.; Roberts, A. L.; Alfonso, F. S.; Rotello, V. M.; et al. Multiplexed Imaging of Nanoparticles in Tissues Using Laser Desorption/Ionization Mass Spectrometry. *J. Am. Chem. Soc.* **2013**, *135* (34), 12564–12567.

(31) Hou, S.; Sikora, K. N.; Tang, R.; Liu, Y.; Lee, Y.-W.; Kim, S. T.; Jiang, Z.; Vachet, R. W.; Rotello, V. M. Quantitative Differentiation of Cell Surface-Bound and Internalized Cationic Gold Nanoparticles Using Mass Spectrometry. *ACS Nano* **2016**, *10* (7), 6731–6736.

(32) Holzlechner, M.; Bonta, M.; Lohninger, H.; Limbeck, A.; Marchetti-Deschmann, M. Multisensor Imaging - From Sample Preparation to Integrated Multimodal Interpretation of LA-ICPMS and MALDI MS Imaging Data. *Anal. Chem.* **2018**, *90* (15), 8831–8837.

(33) de Vega, R. G.; Sanchez, M. L. F.; Eiro, N.; Vizoso, F. J.; Sperling, M.; Karst, U.; Medel, A. S. Multimodal Laser Ablation/Desorption Imaging Analysis of Zn and MMP-11 in Breast Tissues. *Anal. Bioanal. Chem.* **2018**, *410* (3), 913–922.

(34) Niehoff, A.-C.; Schulz, J.; Soltwisch, J.; Meyer, S.; Kettling, H.; Sperling, M.; Jeibmann, A.; Dreisewerd, K.; Francesconi, K. A.; Schwerdtle, T.; et al. Imaging by Elemental and Molecular Mass Spectrometry Reveals the Uptake of an Arsenolipid in the Brain of Drosophila Melanogaster. *Anal. Chem.* **2016**, *88* (10), 5258–5263.

(35) Jiang, Y.; Tang, R.; Duncan, B.; Jiang, Z.; Yan, B.; Mout, R.; Rotello, V. M. Direct Cytosolic Delivery of SiRNA Using Nanoparticle-Stabilized Nanocapsules. *Angew. Chemie - Int. Ed.* **2015**, *54* (2), 506–510.

(36) Wallace, M.; Morris, C.; O'Grada, C. M.; Ryan, M.; Dillon, E. T.; Coleman, E.; Gibney, E. R.; Gibney, M. J.; Roche, H. M.; Brennan, L. Relationship between the Lipidome, Inflammatory Markers and Insulin Resistance. *Mol. BioSyst.* **2014**, *10* (6), 1586–1595.

(37) Sun, Y.; Yin, M.; Zhang, L.; Pan, J. Characterization of the Cytokine Expression Profiles of the Aorta and Liver of Young Tumor Necrosis Factor Alpha Mutant Mice. *Mol. Cell. Biochem.* **2012**, *366* (1–2), 59–67.

(38) Cawthorn, W. P.; Sethi, J. K. TNF-α and Adipocyte Biology. *FEBS Lett.* **2008**, *582* (1), 117–131.

(39) Elci, S. G.; Yesilbag Tonga, G.; Yan, B.; Kim, S. T.; Kim, C. S.; Jiang, Y.; Saha, K.; Moyano, D. F.; Marsico, A. L. M.; Rotello, V. M.; et al. Dual-Mode Mass Spectrometric Imaging for Determination of in Vivo Stability of Nanoparticle Monolayers. *ACS Nano* **2017**, *11* (7), 7424–7430.

(40) Yan, B.; Kim, S. T.; Kim, C. S.; Saha, K.; Moyano, D. F.; Xing, Y.; Jiang, Y.; Roberts, A. L.; Alfonso, F. S.; Rotello, V. M.; et al. Multiplexed Imaging of Nanoparticles in Tissues Using Laser Desorption/Ionization Mass Spectrometry. *J. Am. Chem. Soc.* **2013**, *135* (34), 12564–12567.

(41) Brust, M.; Walker, M.; Bethell, D.; Schiffrin, D. J.; Whyman, R. Synthesis of Thiol-Derivatised Gold Nanoparticles in a Two-Phase Liquid–Liquid System. *J. Chem. Soc., Chem. Commun.* **1994**, No. 7, 801–802.

(42) Miranda, O. R.; Chen, H.-T.; You, C. C.; Mortenson, D. E.; Yang, X.-C.; Bunz, U. H. F.; Rotello, V. M. Enzyme-Amplified Array Sensing of Proteins in Solution and in Biofluids. *J. Am. Chem. Soc.* **2010**, *132* (14), 5285–5289.

(43) Hostetler, M. J.; Templeton, A. C.; Murray, R. W. Dynamics of Place-Exchange Reactions on Monolayer-Protected Gold Cluster Molecules. *Langmuir* **1999**, *15* (11), 3782–3789.

(44) Stanford, T. E.; Bagley, C. J.; Solomon, P. J. Informed Baseline Subtraction of Proteomic Mass Spectrometry Data Aided by a Novel Sliding Window Algorithm. *Proteome Sci.* **2016**, *14* (1), 19.

(45) Klein, O.; Strohschein, K.; Nebrich, G.; Fuchs, M.; Thiele, H.; Giavalisco, P.; Duda, G. N.; Winkler, T.; Kobarg, J. H.; Trede, D.; et al. Unraveling Local Tissue Changes within Severely Injured Skeletal Muscles in Response to MSC-Based Intervention Using MALDI Imaging Mass Spectrometry. *Sci. Rep.* **2018**, *8* (1), 12677.

(46) Gelaye, B.; Sumner, S. J.; McRitchie, S.; Carlson, J. E.; Ananth, C. V.; Enquobahrie, D. A.; Qiu, C.; Sorensen, T. K.; Williams, M. A. Maternal Early Pregnancy Serum Metabolomics Profile and Abnormal Vaginal Bleeding as Predictors of Placental Abruption: A Prospective Study. *PLoS One* **2016**, *11* (6), e0156755.

(47) Gemoll, T.; Miroll, E.; Klein, O.; Lischka, A.; Eravci, M.; Thorns, C.; Habermann, J. K. Spatial UBE2N Protein Expression Indicates Genomic Instability in Colorectal Cancers. *BMC Cancer* **2019**, *19* (1), 710.

CHAPTER 3

NANODELIVERY VEHICLES GENERATE BIOCHEMICAL CHANGES INDEPENDENT OF CARRIER ACCUMULATION AS REVEALED BY MASS SPECTROMETRY IMAGING

Abstract:

Nanodelivery vehicles are widely investigated for the controlled delivery of therapeutics. To assess more fully the efficacy of possible nanodelivery agents, it is essential to understand where the vehicles accumulate and to reveal their site-specific biochemical effects. Here, we use a dual-mode mass spectrometry imaging (MSI) method to evaluate the distributions and biochemical effects of anti-TNFα nanoparticle stabilized capsules (NPSCs) in mice. We find that expected biochemical changes occur at sites away from where the nanomaterials accumulate. In particular, TNFα-specific lipid biomarkers change as expected in the white pulp region of the spleen, while the NPSCs accumulate in the spatially isolated red pulp region of the spleen. Similarly, in the liver, lipid biomarker changes are found in connective tissue, bile ducts, and veins, whereas the NPSCs accumulate primarily in the parenchyma. Unexpectedly, we also find biochemical changes that are associated with the nanomaterials themselves, demonstrating the power of MALDI-MS imaging to reveal markers of possible side effects of the nanodelivery agent. This comprehensive assessment using MSI provides spatial context to nanomaterial distributions and efficacy that cannot be easily achieved with other imaging methods or non-spatially resolved measurement tools.

3.1 Introduction

Nanodelivery vehicles are attractive platforms for distributing therapeutics in a controlled and targeted manner.[1,2] Drugs can be encapsulated in a variety of ways,[3] such as part of an inorganic nanoparticle complex or a lipid bilayer droplet, and these strategies not only allow for the controlled circulation of therapeutics, but also create the potential for more efficacious therapies through dose reduction and directed delivery.[1,2,4] Inorganic nanomaterials are attractive for drug delivery applications due to their high stability, unique physical and chemical properties, and the exquisite synthetic control over their surface chemistry.[2,5] The tunability of these modular systems provides many opportunities to deliver various cargos, including siRNA,[6–8] hydrophobic drugs,[9,10] and proteins.[11]

A frequent challenge that is encountered when developing nanodelivery vehicles is controlling where particles distribute *in vivo*, so that they can have the greatest efficacy.[12] Unfortunately, studies focused on anti-cancer nanodelivery vehicles, for instance, report extremely low success rates (median, 0.7%) in reaching target tumor sites.[13] Instead, most nanodelivery vehicles are found to distribute to the mononuclear phagocytic system (MPS), predominantly the liver, spleen, and kidney.[13–16] While delivery to tumors is apparently inefficient and nanodelivery vehicle levels in MPS-related tissues are typically high, studies rarely address the biochemical changes that occur *in vivo* upon injection of these materials. An assessment of these biochemical changes, and not just their biodistributions, is necessary to evaluate the efficacy of these nanodelivery vehicles.

Given that higher organisms have sophisticated biochemical machinery to process foreign bodies, it is possible that nanodelivery drugs could cause a biochemical effect that is not localized with their accumulation sites. For example, macrophages, which can

identify nanomaterials as foreign bodies, interact with T cells to elicit immune responses in their target organs (e.g. spleen), but often the generated responses can be in separate sub-organ regions from where the original foreign body was taken up by macrophages.[17] It is therefore important to assess if nanomaterials and their cargo can induce biochemical changes at sites distant from where they accumulate. The ability of nanomaterials to generate a distant biochemical response could suggest an alternate/indirect means of therapy, especially given the inefficiency with which anti-cancer nanodelivery agents accumulate in tumors.

To assess the possibility that nanodelivery systems can elicit biochemical effects distant from their accumulation sites, we have applied mass spectrometry (MS) imaging methods to site-specifically track the *in vivo* distributions of nanodelivery systems and their effects
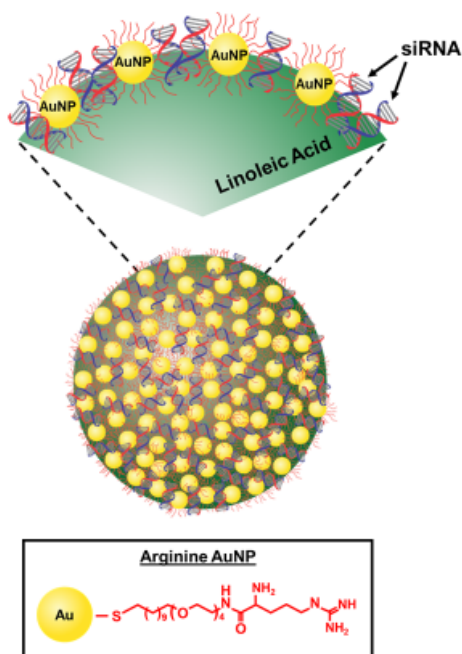
Figure 3.1. Nanoparticle stabilized capsule (NPSC) design and arginine AuNP ligand structure. AuNPs are emulsified with linoleic acid and the arginine headgroup forms a stable macrostructure by interacting with the negatively charged siRNA cargo.

on the underlying biochemistry. Specifically, we use laser ablation-inductively coupled plasma mass spectrometry (LA-ICP-MS)[18–21] and matrix-assisted laser desorption/ionization MS (MALDI-MS)[22,23] based imaging approaches to monitor the sub-organ biodistributions and biochemical effects of a gold nanoparticle-based delivery platform. As a testbed nanodelivery system, we used gold nanoparticle stabilized capsules (NPSCs) (Figure 3.1), which have the demonstrated ability to deliver proteins, siRNA, and small molecule drugs to the cytoplasm of cells.[6,9,11,24,25] TNF-α-targeting siRNA was utilized as the cargo in the current study as NPSCs with this siRNA have been successfully used to knockdown this cytokine *in vitro* and *in vivo*.[6] Moreover, TNF-α suppression produces predictable changes in serum lipid levels,[26] providing a convenient set of biomolecules to track via MALDI-MS imaging.

Using these two MS-based imaging methods, we find that nanodelivery agents can produce the intended biochemical effect in a different location than where the nanomaterials themselves accumulate. Moreover, the ability of MALDI-MS imaging to measure site-specific changes in lipid levels provides a rich set of new biochemical insight into how nanodelivery vehicles themselves influence inflammation pathway, as exemplified by changes in glucosylceramide levels that correlate with the NPSC distributions.

3.2 Results and Discussion

ICP-MS measurements of tissue homogenates of mice injected with NPSCs containing TNF-α targeting siRNA (TNF-α NPSCs) reveal that the nanocarriers predominantly distribute to the liver and spleen tissues (Figure 3.2). This *in vivo* distribution pattern is similar to how other positively charged nanomaterials distribute.[13,18,27–29] Liver and spleen
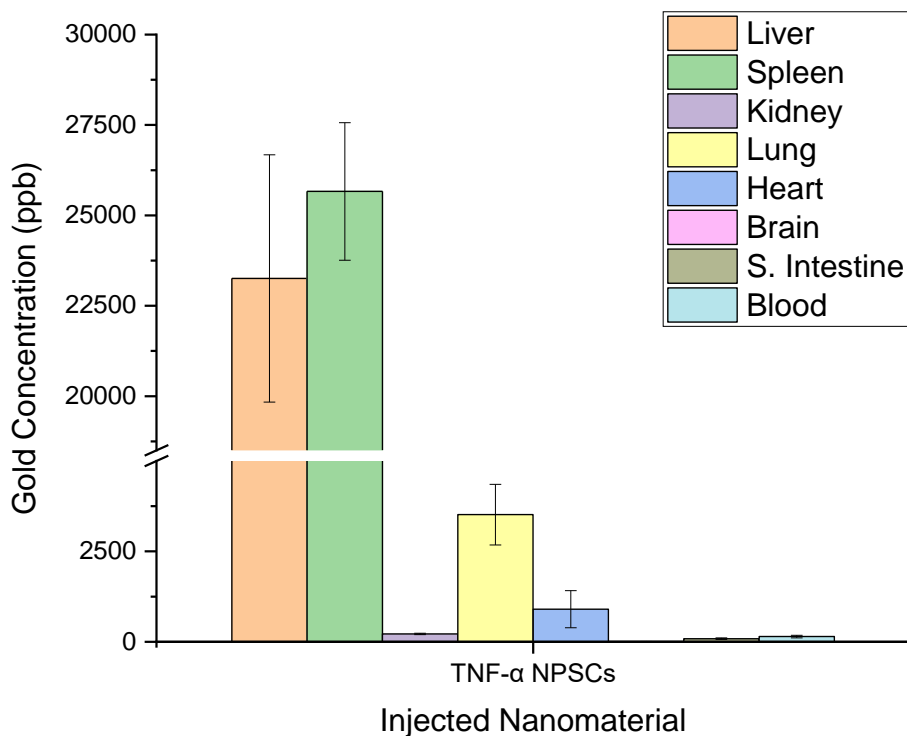
Figure 3.2. ICP-MS analysis of gold in digested NPSC-injected mouse tissues. All reported concentrations are the average of three mice. Error is reported as standard deviation

tissues were thus selected for MS imaging. The distributions of lipid levels in tissues were determined by MALDI-MSI as a means of monitoring pathways that are known to be affected by TNF-α knockdown,[26] and distributions of Au levels in tissues were determined by LA-ICP-MSI as a means of tracking NPSC accumulation sites.

3.2.1 Distribution and colocalization of nanocarrier and biochemical changes in the spleen

MALDI-MS of spleen tissue sections measured 52 different lipids, 44 of which responded to TNF-α in a predictable manner. Utilizing the area under the curve (AUC) of receiver operating characteristic (ROC) curves and ion abundance box-and-whisker plots, lipids were evaluated as successful binary classifiers between the treated and control

tissues.[22,30,31] Based on the measured signals of the 44 lipids from at least three different tissues, 33 lipids are found to change as predicted in the spleens of TNF-α NPSC-injected mice when compared to control tissues (Table 3.1). By using the signal for heme B, which is a biomarker for the red pulp of the spleen,[32] the distributions of lipid changes can be classified as occurring in the white pulp (no heme B signal) or red pulp. For example, PE (p-34:1) and PC (p-40:5), which are plasmalogens known to be involved in anti-inflammatory and anti-oxidant responses in mammalian tissues,[33] increase in the lymphoid-rich white pulp (Figure 3.3a and b). Lipids signals that change in this lymphocyte-rich region of the spleen may be indicative of a downstream immunological response from the NPSCs cargo delivery. Conversely, PE (38:2), which is an unsaturated phosphatidylethanolamine, is known to be involved in membrane curvature and fluidity during membrane fusion,[34] increases mostly in the red pulp (Figure 3.3c). Differentiating the sub-organ distributions of these specific biomarkers is important to better illustrate whether anti-inflammatory responses are occurring (i.e. in the splenic white pulp)[35] versus biochemical responses to cellular uptake (i.e. macrophages in the red pulp).[18,35] Overall,
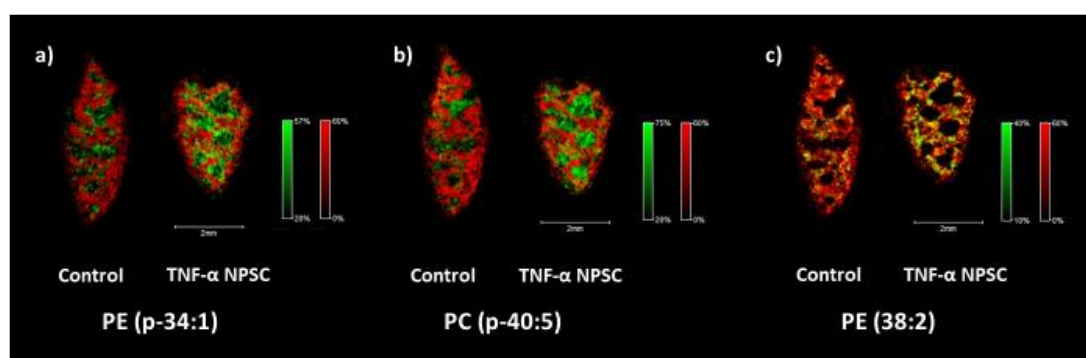
Figure 3.3. MALDI-MS images of predicted lipid responses (green pixels) in TNF-α NPSC-injected mouse spleen tissues (right in each image pair) compared to control spleen tissues (left in each image pair). Lipid images are over laid with heme B (red pixels) to determine sub-organ distribution. Areas of high colocalization between a lipid and Heme B are indicated by yellow pixels. Panels (a) and (b) are representative images of lipids that respond in the white pulp of TNF-α NPSC spleen tissues. Panel (c) is a representative image of a lipid that responds in the red pulp.

Table 3.1. Detected lipid changes in spleen tissues of mice injected with TNF-α-targeting siRNA NPSCs, scrambled siRNA NPSCs, or arginine AuNPs as compared to control mouse spleen tissues. Lipid responses in the TNF-α NPSC column are highlighted in green for "predicted" responses and in red for "unexpected" responses. Lipids are highlighted in scrambled NPSCs or arginine AuNP column if they share a response with the TNF-α column. (Abbreviations: LPC – lysophosphatidylcholine; PC – phosphatidylcholine; Cer – ceramide; SM – sphingomyelin; PE – phosphatidylethanolamine; CAR – carnitine; "p-" – plasmalogen)

Lipid I.D.	Detected m/z	TNF-α NPSCs (+) or (-) compared to control	Scrambled NPSCs (+) or (-) compared to control	Arginine AuNPs (+) or (-) compared to control
LPC (16:0)	496.3 518.4	(+)	None	None
LPC (18:0)	524.4	(+)	None	None
LPC (p-18:0)	508.6	(-)	(-)	None
LPC (18:2)	520.2	None	None	None
LPC (20:4)	544.3	(-)	None	(-)
PC (30:0)	706.6	None	None	None
PC (32:0)	734.5 772.5	(+)	None	(+)
PC (p-32:0)	756.5	(+)	(+)	None
PC (34:0)	762.6	(+)	(+)	None
PC (p-34:0)	746.6	(+)	(+)	None
PC (34:1)	760.6 798.6	None	None	None
PC (p-34:1)	744.6	None	(+)	None
PC (34:2)	780.5	None	None	None
PC (34:3)	756.6	(+)	(+)	None
PC (p-36:5)	786.6 802.5	(+)	None	None
PC (p-36:4)	788.6 804.5	(+)	(+)	None
PC (p-36:2)	770.6 792.6 808.5	(+)	None	None
PC (36:0)[d]	790.6 812.6 828.5	(+)	(+)	None

PC (p-38:6)[d]	790.6 828.5	(+)	(+)	None
PC (p-38:5)	792.5 830.5	(+)	None	None
PC (p-38:4)	794.7 816.6 832.5	(+)	(-)	None
PC (p-40:5)	820.6 858.6	(+)	None	None
2H OH Cer (d18:1/20:0)	650.5	(-)	None	None
2H Cer (d18:1/25:1)	681.7	(-)	None	None
2H Cer (d18:1/20:1)	632.5	(-)	None	None
Glucosylceramide	806.2	(+)	(+)	(+)
SM (d18:1/17:0)	741.6 757.6	(+)	None	None
SM (d18:1/20:0)	759.6	(+)	None	None
SM (d18:1/21:1)	771.6 809.6	(+)	(+)	None
SM (d18:1/23:2)	819.6	(-)	None	None
SM (d18:1/24:0)	853.7	(+)	(-)	None
SM (d18:1/24:3)	809.6 847.6	(+)	(+)	(+)
PE (26:4)	497.2	(+)	(+)	None
PE (p-34:3)	557.5	(+)	None	(+)
PE (p-34:2)	559.5 581.5	None	None	None
PE (p-34:1)[d]	583.5	(-)	None	None
PE (p-36:4)[d]	583.5	(-)	None	None
PE (p-34:1)	732.5	(+)	None	None
PE (p-36:4)	724.5	(+)	None	None
PE (p-36:3)	585.5	(+)	None	None
PE (38:2)	669.5	(+)	(-)	None
PE (38:1)[d]	671.5	None	None	None
PE (p-40:5)[d]	671.5	None	None	None
CAR (16:0)	400.4	(-)	None	(+)
CAR (18:1)	426.6	(-)	None	(+)

79% of the 33 predicted lipid changes are found in the white pulp of the spleen tissue. These MSI data indicate that the majority of the lipid responses are due to the efficacious delivery of the anti-inflammatory siRNA therapeutic to the appropriate cell types.

To ensure that these lipid changes arise from biochemical changes induced by TNF-α knockdown, and not the NPSC carrier itself, mice were also injected with scrambled (non-functional) siRNA-containing NPSCs (scrambled NPSCs) and the free arginine-functionalized NPs (arginine AuNPs) that comprise the capsules. Of the 44 detected lipids, only 11 and five have significantly altered levels in the spleens of mice injected with scrambled NPSCs, and arginine NPs, respectively (Table 3.1), indicating that the majority of the lipid changes seen in mice injected with TNF-α specific NPSCs are due to TNF-α-targeted knockdown. In mice injected with the scrambled NPSCs, most lipids behave like PC (p-40:5) (Figure 3.4). Their signal levels do not change significantly compared to the control, regardless of whether they are found in the white pulp or red pulp.
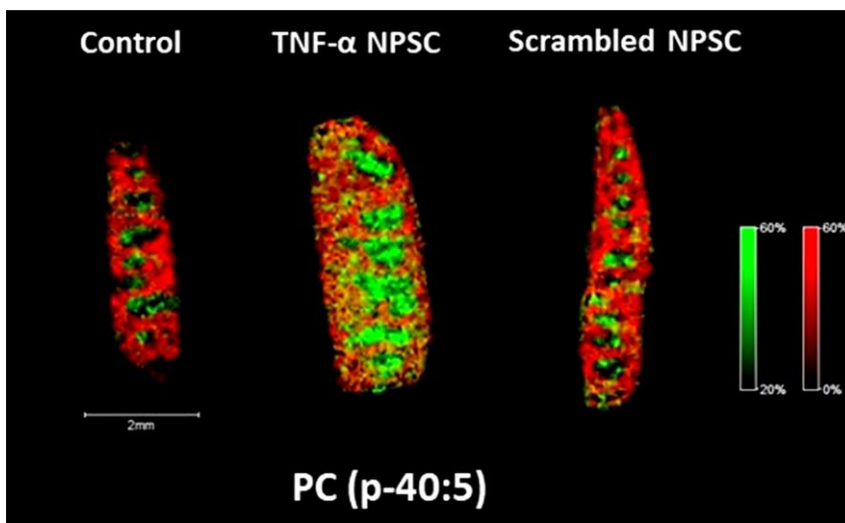
Figure 3.4. MALDI-MS images of PC (p-40:5) response (green pixels) in TNF-α and scrambled NPSC-injected mouse spleen tissues compared to control spleen tissues. Lipid images are over laid with heme B (red pixels) to determine sub-organ distribution. When compared to the control tissue, the TNF-α NPSC exhibits a ROC AUC of 0.810 and the scrambled NPSC had an ROC AUC of 0.610.
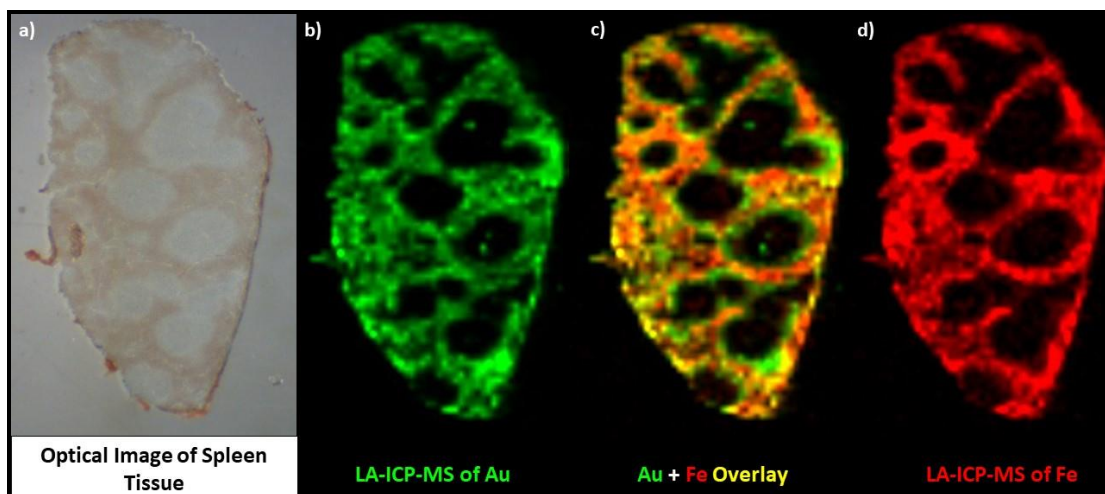
Figure 3.5. Optical and LA-ICP-MS images of TNF-α NPSC-injected mouse spleen. (a) Optical camera images from Teledyne CETAC LSX-213 G2 laser ablation system. (b) Reconstructed 50 μm LA-ICP-MS image of gold, single color scale. (c) Gold (green) and iron (red) LA-ICP-MS overlay images. Yellow pixels indicate analyte overlap. (d) Reconstructed 50 μm LA-ICP-MS image of iron, single color scale.

LA-ICP-MS imaging was used to investigate the distribution in the spleen of the TNF-α NPSCs themselves (Figure 3.5). In these images, Fe signals were used to discern the blood-rich red pulp from the white pulp (Figure 3.5b), as has been done in several previous studies.[18–20] A quick visual comparison of the Au (Figure 3.5c) and Fe distributions indicate that the two metals have similar distributions, and this similarity is even more apparent from the overlaid images (Figure 3.5d). Based on a quantitative pixel analysis of the overlaid Au and Fe images in Figure 3.5d, a Pearson correlation analysis indicates a 67% correlation between the Au and Fe distributions. LA-ICP-MS imaging analysis of 3 spleen tissues from 3 mice lead to an average correlation of 65%. Overall, these results indicate that the Au carrier predominantly accumulates in the red pulp of the spleen. A very similar observation is made for spleen tissues from mice injected with scrambled NPSCs. The NPSCs accumulate mostly in the red pulp of the spleen (Figure 3.6). An average correlation of 43% between Au and Fe is found for the scrambled NPSCs.
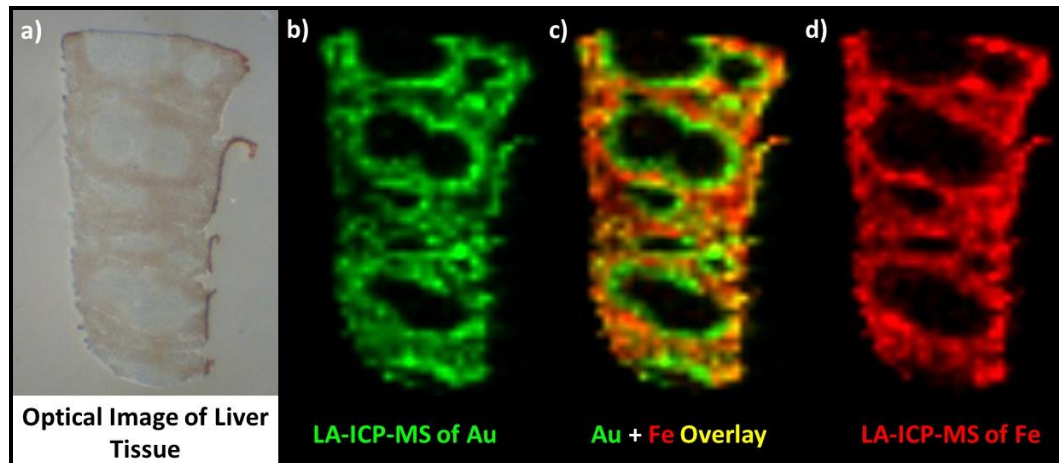
Figure 3.6. Optical and LA-ICP-MS images of scrambled NPSC-injected mouse spleen. (a) Optical camera images from Teledyne CETAC LSX-213 G2 laser ablation system. (b) Reconstructed 50 μm LA-ICP-MS image of gold, single color scale. (c) Gold (green) and iron (red) LA-ICP-MS overlay images. Yellow pixels indicate analyte overlap. (d) Reconstructed 50 μm LA-ICP-MS image of iron, single color scale.

While Au primarily accumulates in the red pulp, most (79%) predicted lipid changes due to TNF-α knockdown occur in the white pulp of the spleen (e.g. Figure 3.3), indicating that the intended biochemical effect occurs in a different location than where the NPSCs accumulate. To confirm these results quantitatively, the LA-ICP-MS and MALDI-MS images were co-registered based on previous reports,[36,37] and correlations were calculated between Au and each lipid. Based on these correlation analyses, 25 of the 33 lipids that change as expected negatively correlate with the distribution of the NPSCs (Figure 3.7), whereas only eight of them positively correlate with the NPSCs. Clearly, most of the TNF-α knockdown related changes occur independently of the nanodelivery vehicle distribution.

3.2.2 Distribution and colocalization of nanocarrier and biochemical changes in the liver

NPSC and lipid distributions were also assessed in the liver due to the high gold content in this tissue (Figure 3.2). In the liver, 40 TNF-α-specific lipids are measured by MALDI-MS, and 18 of these 40 lipids undergo the expected change (Table 3.2). Fewer lipids in the

Figure 3.7. Correlation plot of MALDI-MSI lipid distributions compared to LA-ICP-MS gold distributions in NPSC spleen tissue. Lipids are separated by class from left to right: phosphatidylcholines, carnitines, lysophosphatidylcholines, sphingomyelins, phosphatidylethanolamines, ceramides. Lipids with a value close to +1 have a strong positive correlation with gold distribution, lipids with a value close to -1 have a strong negative correlation with gold distribution. Lipids with close to zero have no significant correlation with gold.

liver are observed to change as expected, in comparison to the spleen, in part due to lower overall lipid signals in the liver. Only nine and five of these 40 lipids undergo significant changes in mice that are injected with the scrambled NPSCs and arginine AuNPs, respectively, indicating that the lipid changes are again primarily due to TNF-α knockdown. Unlike in the spleen, which has visually apparent sub-organ regions, the lipid distributions in the liver are not as easily classified into different regions sub-organ regions (Figure 3.8). LA-ICP-MS images reveal that Au has a punctate distribution in the liver (Figure 3.9a and b). Previous work has shown that positively-charged AuNPs accumulate

Table 3.2. Detected lipid changes in liver tissues of mice injected with TNF-α-targeting siRNA NPSCs, scrambled siRNA NPSCs, or arginine AuNPs as compared to control mouse spleen tissues. Lipid responses in the TNF-α NPSC column are highlighted in green for "predicted" responses and in red for "unexpected" responses. Lipids are highlighted in scrambled NPSCs or arginine AuNP column if they share a response with the TNF-α column. (Abbreviations: LPC – lysophosphatidylcholine; PC – phosphatidylcholine; Cer – ceramide; SM – sphingomyelin; PE – phosphatidylethanolamine; CAR – carnitine; "p-" – plasmalogen)

Lipid I.D.	Detected m/z	TNF-α NPSCs (+) or (-) compared to control	Scrambled NPSCs (+) or (-) compared to control	Arginine AuNPs (+) or (-) compared to control
LPC (16:0)	496.3	(+)	None	None
LPC (18:0)	524.4	(-)	None	None
LPC (p-18:0)	508.6	(-)	None	None
LPC (18:2)	520.2	None	None	None
LPC (20:4)	544.3	None	None	None
PC (30:0)	706.6	None	None	None
PC (32:0)	734.5 772.5	(+)	(+)	None
PC (p-32:0)	756.5	None	(-)	None
PC (34:0)	784.6	(+)	(+)	None
PC (p-34:0)	746.6	None	None	None
PC (34:1)	760.6	None	N/A	N/A
PC (p-34:1)	744.6	None	None	N/A
PC (34:2)	780.5	(+)	None	None
PC (34:3)	756.6	None	None	None
PC (p-36:5)	786.6 802.5	(+)	None	None
PC (p-36:4)	788.6	(+)	None	None
PC (p-36:2)	770.6	(+)	None	None
PC (36:0)[d]	828.5	(+)	None	None
PC (p-38:6)[d]	828.5	(+)	None	None
PC (p-38:5)	792.5 830.5	None	None	None

PC (p-38:4)	832.5	(+)	None	None
PC (p-40:5)	820.6 858.6	(+)	None	None
2H OH Cer (d18:1/20:0)	650.5	(-)	None	None
2H Cer (d18:1/20:1)	632.5	None	None	None
Glucosylceramide	806.2	(+)	(+)	(+)
SM (d18:1/17:0)	741.6 757.6	None	None	None
SM (d18:1/21:1)	771.6 809.6	(+)	None	None
SM (d18:1/24:3)	809.6 847.6	(+)	(+)	(+)
PE (p-34:1)	732.5	(-)	None	None
PE (38:1)	671.5	(-)	(-)	(-)
PE (p-40:5)	671.5	(-)	(-)	(-)
CAR (16:0)	400.4	(-)	(-)	(-)

in the hepatocytes, giving rise to such a distribution,[18,27] suggesting that the positively-charged NPs used in the NPSCs studied here likely also accumulate in hepatocytes. Images from mice injected with scrambled NPSC liver tissues show the same punctate Au distribution (Figure 3.10).
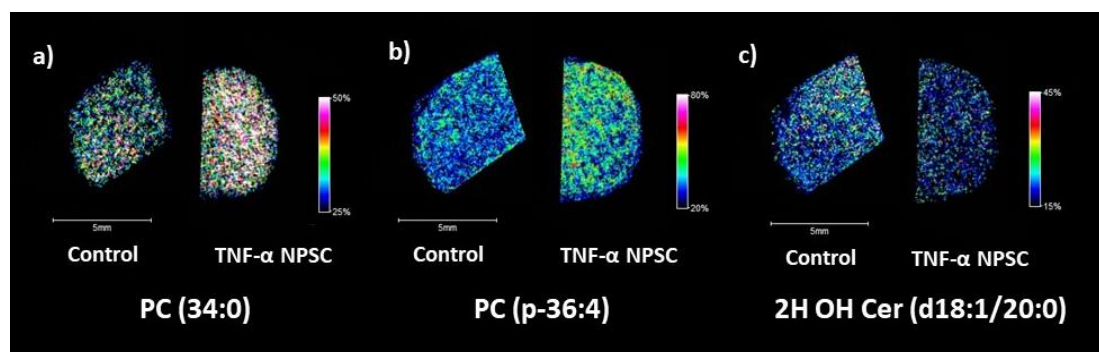
Figure 3.8. MALDI-MS images of predicted lipid responses in TNF-α NPSC-injected mouse liver tissues (right in each image pair) compared to control liver tissues (left in each image pair). Panels (a) and (b) are representative images of lipids that increase in TNF-α NPSC liver tissues. Panel (c) is a representative image of a lipid that decreases in TNF-α NPSC liver tissues.
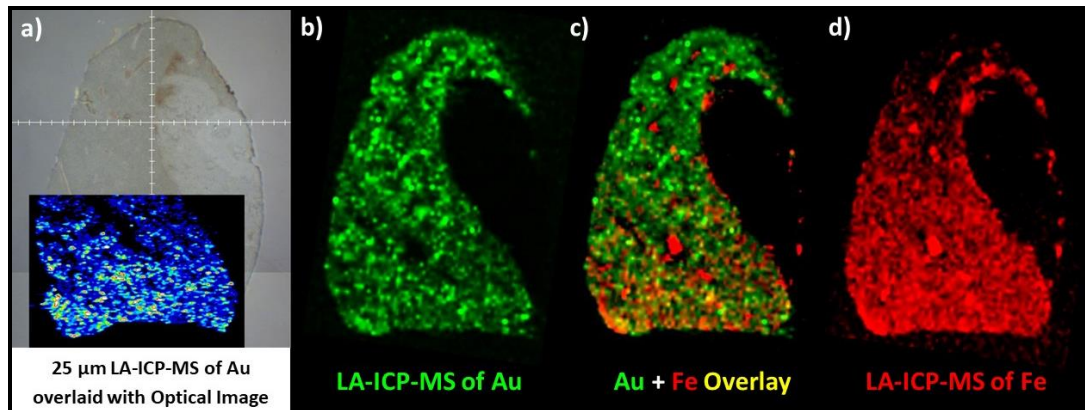
Figure 3.9. Optical and LA-ICP-MS images of TNF-α NPSC mouse liver. (a) Overlay of optical camera image from Teledyne CETAC LSX-213 G2 laser ablation system and 25 μm LA-ICP-MS image of gold of a TNF-α NPSCs mouse liver slice. The punctate distribution of gold has been previously observed for positively charged nanoparticles, indicating localization to the hepatocytes of the liver.[17] (b) Reconstructed 50 μm LA-ICP-MS image of gold heat map. (c) Reconstructed 50 μm LA-ICP-MS image of gold, single color scale. (d) Gold (green) and iron (red) LA-ICP-MS overlay images. (e) Reconstructed 50 μm LA-ICP-MS image of iron, single color scale.

When we compare the distributions of Au and the lipids that change upon TNF-α knockdown after co-registering the LA-ICP-MS and MALDI-MS images, we again find that the lipid changes mostly do not correlate with Au accumulation sites (Figure 3.11). The majority (13 of 18) of the predicted TNF-α induced changes occur throughout the liver
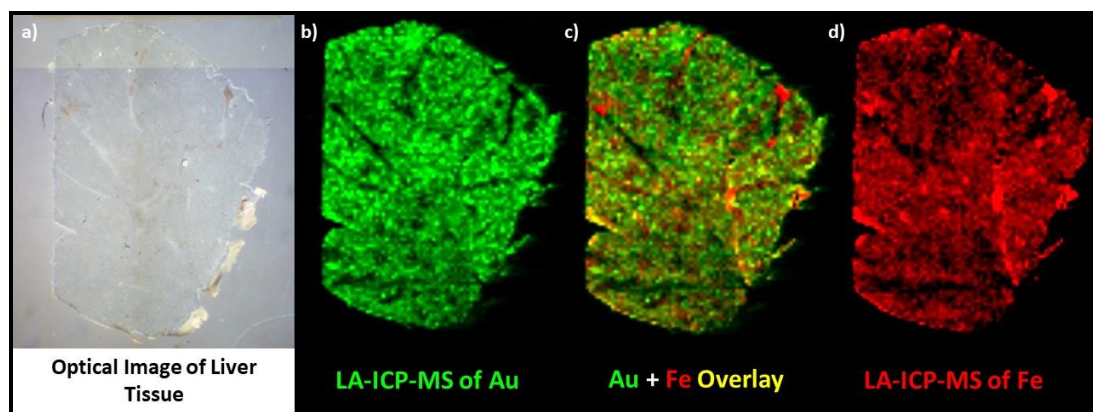
Figure 3.10. Optical and LA-ICP-MS images of scrambled NPSC mouse liver. (a) Optical camera images from Teledyne CETAC LSX-213 G2 laser ablation system. (b) Reconstructed 50 μm LA-ICP-MS image of gold heat map. (c) Reconstructed 50 μm LA-ICP-MS image of gold, single color scale. (d) Gold (green) and iron (red) LA-ICP-MS overlay images. (e) Reconstructed 50 μm LA-ICP-MS image of iron, single color scale.
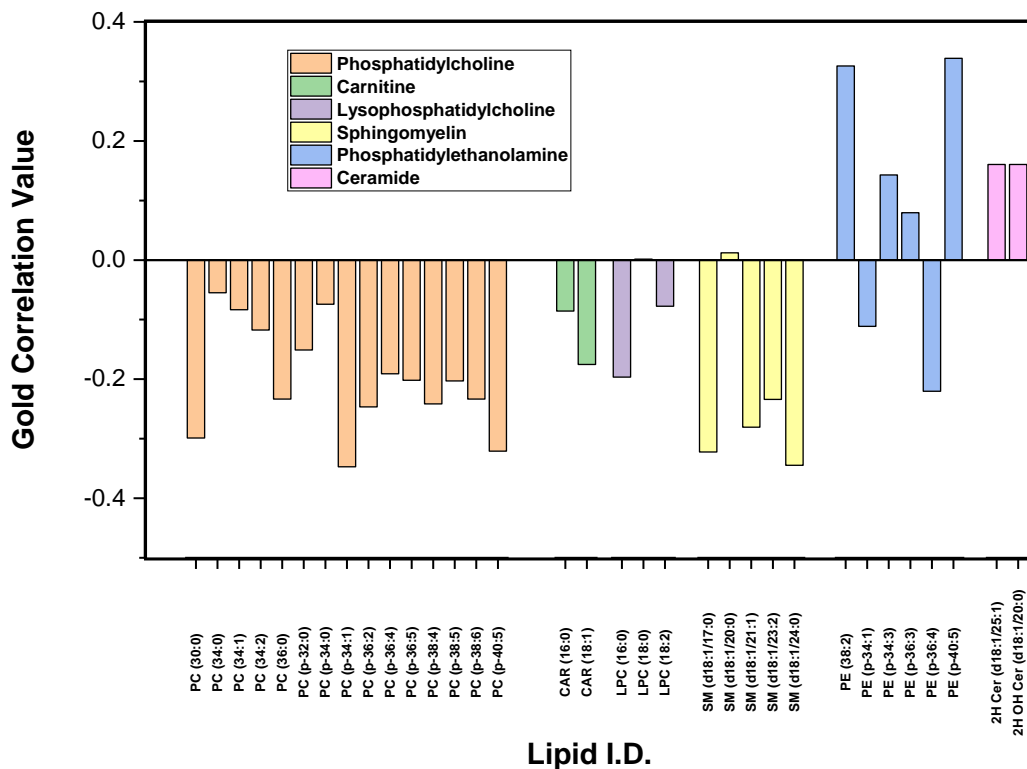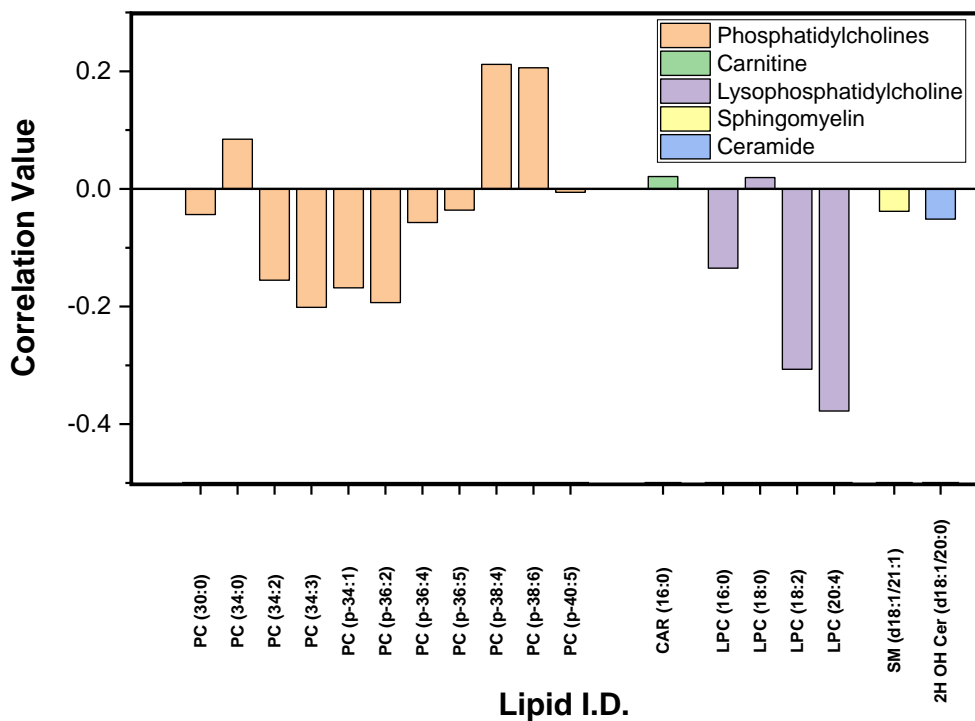
Figure 3.11. Correlation plot of MALDI-MSI lipid distributions compared to LA-ICP-MS gold distributions in NPSC liver tissue. Lipids are separated by class from left to right: phosphatidylcholines, carnitines, lysophosphatidylcholines, sphingomyelins, phosphatidylethanolamines, ceramides. Lipids with a value close to +1 have a strong positive correlation with gold distribution, lipids with a value close to -1 have a strong negative correlation with gold distribution. Lipids with close to zero have no significant correlation with gold.

tissue, and do not correlate strongly with the Au carrier distribution. These data suggest that the lipid responses also occur independently of the nanodelivery vehicle distribution in the liver as was observed in the spleen.

Even though sub-organ regions of the liver are not readily apparent, some lipids are known to associate with certain regions of the liver (Figure 3.12),[38] allowing the distribution of gold to be assigned to individual sub-organ regions. The NPSCs are found to accumulate mostly in the parenchyma (78%) and veins (22%) with none occurring in the bile ducts or connective tissue. These results are consistent with previous work that showed the accumulation of positively-charged AuNPs in the hepatocytes of the liver,[18]
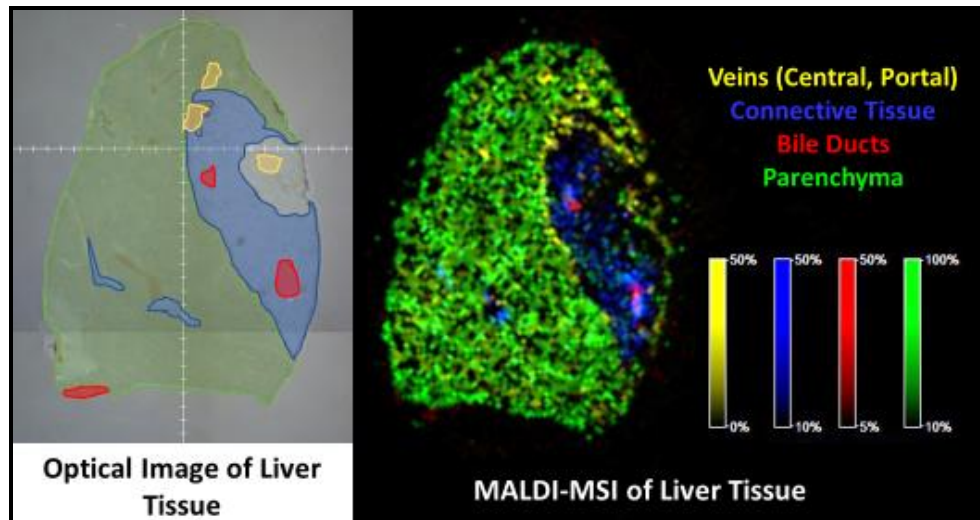
Figure 3.12. Example optical and MALDI-MSI liver images to classify sub-organ regions of liver tissue. Veins are indicated by yellow pixels, connective tissue by blue pixels, bile ducts by red pixels, and parenchyma by green pixels.

which are found in the parenchyma. Of the TNFα-related lipid changes in the liver, most occur in the connective tissue (34%) and the parenchyma (32%), with some also occurring in the veins (18%) and bile ducts (16%). Interestingly, the connective tissue is known be the liver's main source of mast cells,[39] which are heavily involved in transmitting signals during an inflammatory response in the liver.[40] Overall, like in the spleen, the effects of the anti-TNF-α therapy primarily occur in regions where the gold NPSC carriers are not accumulating.

3.2.3 Distribution of unexpected lipid changes in tissue of NPSC-injected mice

The dual-mode imaging method used here reveals not only that the NPSCs elicit their biochemical changes at locations away from where they accumulate but also that some biochemical changes are likely caused by the nanocarrier itself. The inherent multiplexed nature of MALDI-MS imaging along with the Au distributions obtained from LA-ICP-MS allow us to discern unexpected effects of the carrier. One lipid that changes unexpectedly in mice injected with TNF-α NPSCs, scrambled NPSCs, and arginine AuNPs is

glucosylceramide. The signal for this lipid increases in both spleen and liver tissues and is found to positively correlate with gold distributions from tissues injected with each of the nanomaterial constructs. Ceramide is a pro-apoptotic mediator that glucosylceramide synthase (GCS) converts to the nonfunctional compound, glucosylceramide. Glucosylceramides are biomarkers involved in inflammation and are specifically associated with macrophage uptake in the liver, spleen, and kidney. Observing this lipid increase with all three nanomaterial constructs in both the liver and spleen suggests that the AuNPs themselves are causing an inflammatory response. Future work will be necessary to fully understand the nature of this effect.

Utilizing this dual-mode imaging method to provide spatial context to the unexpected changes can help to identify their origin and biochemical significance. For example, glucosylceramide increased unexpectedly in TNF-α NPSC mice liver. Based on analyses of the scrambled NPSC and Arg-AuNP mice, this lipid also increases unexpectedly in these liver tissues. Utilizing co-registration analysis, glucosylceramide is found to correlate with gold 77% in the TNF-α NPSC liver, 93% in the scrambled NPSC liver, and 90% in the Arg-AuNP liver tissues (Figure 3.13). Ceramide is a pro-apoptotic mediator, which glucosylceramide synthase (GCS) converts to the nonfunctional compound, glucosylceramide.[41] Glucosylceramides are biomarkers known to be involved in inflammation, and specifically in macrophage uptake in the liver, spleen, and kidney tissues,[42] therefore correlating greatly with the gold carrier across all tissue types suggests that the AuNP itself is having an inflammatory response in all three tissue types. This assessment utilizing dual-mode imaging and registration provides a more thorough

evaluation of the effects of the nanomaterials themselves and is a powerful way to evaluate

both the efficacy and side effects of nanomaterials *in vivo*.
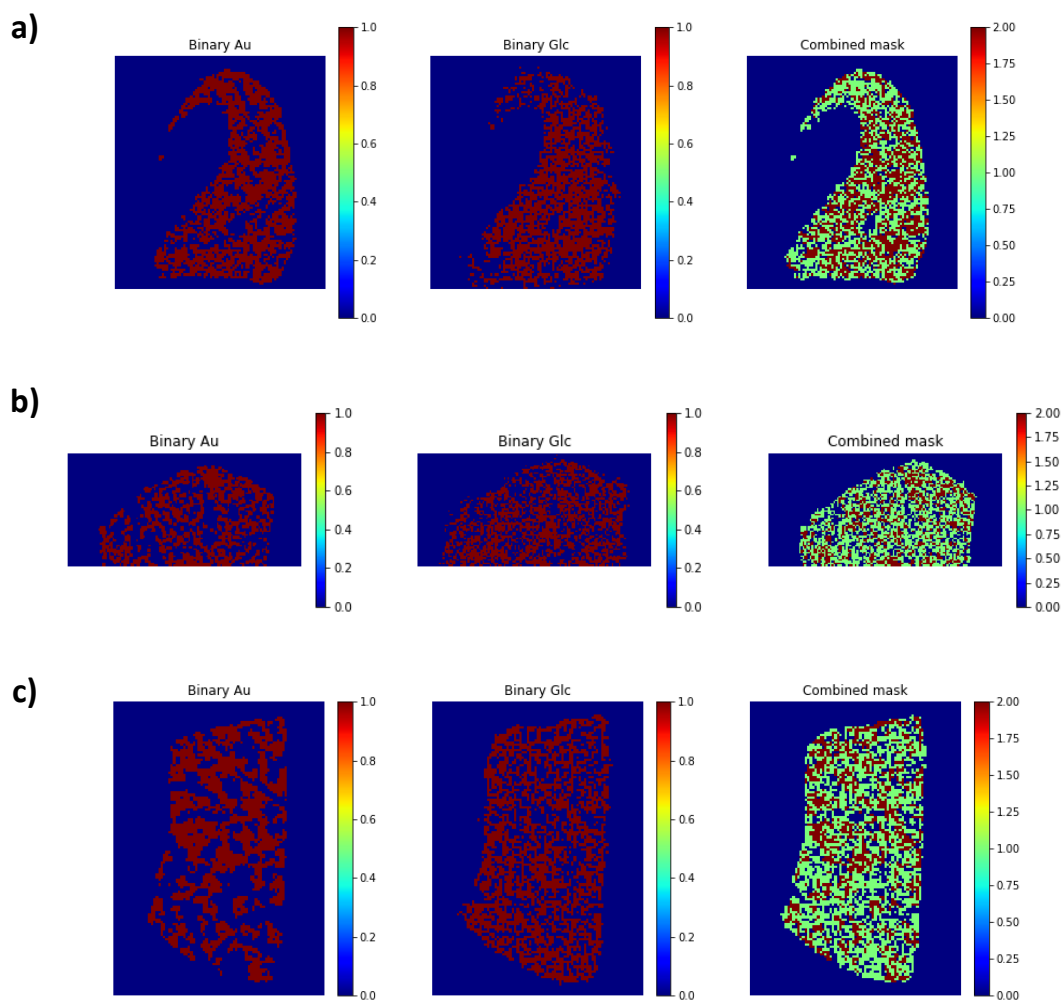
Figure 3.13. LA-ICP-MS gold (Au) (left-most column) and MALDI-MS glucosylceramide (Glc) (middle column) overlaid in a combined binary mask (right-most column) in TNF-α NPSC (a), scrambled NPSC (b), and arginine AuNP (c) liver tissues. In the Au and Glc figures, a value of 0 (blue) indicates no signal and a value of 1 (red) indicates true analyte signal above the noise. In the combined mask, a value of 0 (blue) indicates no signal from either analyte, a value of 1 (red) indicates signal from either Au or Glc, and a value of 2 (green) indicates signal from both Au and Glc.

3.3 Conclusions

MS imaging techniques have been employed to monitor the distribution and co-localization of a nanodelivery system and its biochemical effect in various tissue types. Using these methods, we demonstrate that the majority of the expected biochemical changes occur in regions distant from where the nanodelivery system accumulates. Specifically, we find that anti-TNFα NPSCs cause the expected changes in lipid biomarkers primarily in the white pulp of the spleen, whereas the NPSCs themselves accumulate in the red pulp. Similarly, we find that anti-TNFα NPSCs elicit the expected changes in liver lipid biomarkers in veins, connective tissue, and bile ducts, while the NPSCs accumulate mostly in the parenchyma. These observations are important because they demonstrate that nanodelivery vehicles can generate the desired biochemical responses even though they may not accumulate in the desired location. This ability of nanodelivery agents suggests an indirect means of therapy, which could be particularly important for anti-cancer nanodelivery agents that accumulate inefficiently in tumors. Another important result from the work described here is that information-rich MALDI-MS imaging is capable of identifying unexpected changes in tissue biochemistry that are caused by the presence of nanodelivery vehicles. Such new insight provides a means of understanding and possibly addressing potential side effects that are caused by nanodelivery systems.

3.4 Experimental

3.4.1 Synthesis of Nanoparticles and Nanoparticle Stabilized Capsules

Arginine-functionalized AuNPs (Arg-AuNPs) and NPSCs were synthesized according to a previous report.[22] Briefly, 1-pentanethiol protected AuNPs (Au-C5) were

synthesized via the Brust-Sciffrin two-phase synthesis.[43] Arg-AuNPs were then synthesized by the Murray place-exchange method.[44] NPSCs were generated by emulsifying 1 uL linoleic acid with 1 uM Arg-AuNPs in phosphate buffer. A 2.5 uM aliquot mixture was then combined with 1 uM of siRNA. The mixture was then incubated at room temperature before injection.

3.4.2 Animal Experiments and Tissue Preparation

All animal protocols were approved by the University of Massachusetts Amherst Institutional Animal Care and Use Committee (IACUC), guided by the U.S. Animal Welfare Act and U.S. Public Health Service Policy. Balb/c mice (female, 8-week-old) were obtained from Charles River Laboratories, Inc. (Wilmington, MA). Mice were held in controlled climates (22 ± 2 °C temperature, 12 h light/dark daily cycle) with free access to food and water. Mice were randomly selected for control and nanomaterial treatment. Each mouse was tail-vein-injected with 200 μL of either PBS, 2.5 μM of NPSCs, or 2.5 μM of Arg-AuNPs. After 48 h of particle circulation, mice were sacrificed via carbon dioxide inhalation and cervical dislocation. Mouse tissues were promptly removed, flash frozen in liquid nitrogen, and stored at -80 °C until slicing for MS imaging.

Flash-frozen tissues were sectioned into 12 μm slices via a LEICA CMM1850 cryostat, thaw-mounted onto ITO slides (MALDI-MS) or glass slides (LA-ICP-MS), and desiccated under vacuum for 1 h. Bruker ImagePrep apparatus was used to spray a 25 mg/mL 2,5-DHB solution (1:1 methanol:water) onto the tissues intended for MALDI imaging analysis.

3.4.3 Dual-Mode Imaging Analysis

MALDI-MSI was conducted using a Bruker ultrafleXtreme MALDI-TOF/TOF instrument at 50 μm resolution. All experiments were performed at least three different sets

of tissues and all treated tissues (NPSC or Arg-AuNP-injected) were run simultaneously with control tissues to ensure reproducibility. MS/MS experiments were run via LIFT cell with collision-induced dissociation to confirm biomolecule identities.

LA-ICP-MS imaging was conducted using PerkinElmer NEXION 300 ICP-MS coupled with a Teledyne CETAC LSX-213 G2 laser ablation system which was attached to the ICP-MS via Teflon tubing. Tissues were ablated at a spot size of either 50 or 25 μm with a15 μm/s scan rate, 10 Hz laser frequency, 0.6 L/min He carrier gas flow, and 10 s shutter delay. Images were reconstructed according to previous reports.[18,22,27]

3.4.4 Statistical Evaluation

MALDI-MSI images were normalized and processed in SCiLS Lab 2015b, as previously reported.[22] In brief, baseline subtraction was conducted using the TopHat, followed by total ion count (TIC) normalization, peak picking, and discriminative value determination using both receiver operating characteristic (ROC) curves and ion abundance box-and-whisker plots. ROC area under the curve (AUC) thresholds of greater than 0.65 for analyte increases or lower than 0.35 for analyte decreases were used distinguish significant differences between tissues.

3.4.5 Correlation Plot Calculations

Correlation plot calculations were made by Laura Castellanos in Python using Pearson's correlation analysis. Briefly, MALDI-MS and LA-ICP-MS data were transformed into the same scale. Images were then overlaid using non-linear co-registration with the MALDI set as the fixed image and the LA-ICP-MS image set as the moving image. Once tissues were properly co-registered on a pixel-by-pixel scale, Pearson's correlation was conducted for each analyte against each other to assess the strength of association

between the two variables with -1 being an absolute negative correlation, +1 being an absolute positive correlation, and 0 being no correlation.

3.5 References

(1)   De, M.; Ghosh, P. S.; Rotello, V. M. Applications of Nanoparticles in Biology. *Adv. Mater.* **2008**, *20* (22), 4225–4241.

(2)   Yu, X.; Trase, I.; Ren, M.; Duval, K.; Guo, X.; Chen, Z. Design of Nanoparticle-Based Carriers for Targeted Drug Delivery. *J. Nanomater.* **2016**, 1087250.

(3)   Yih, T. C.; Al-Fandi, M. Engineered Nanoparticles as Precise Drug Delivery Systems. *J. Cell. Biochem*. **2006**, 97(6), 1184-1190.

(4)   Kumar, B.; Jalodia, K.; Kumar, P.; Gautam, H. K. Recent Advances in Nanoparticle-Mediated Drug Delivery. *J. Drug Deliv. Sci. Technol.* **2017**, *41* (6), 260–268.

(5)   Dreaden, E. C.; Alkilany, A. M.; Huang, X.; Murphy, C. J.; El-Sayed, M. a. The Golden Age: Gold Nanoparticles for Biomedicine. *Chem. Soc. Rev.* **2012**, *41* (7), 2740.

(6)   Jiang, Y.; Hardie, J.; Liu, Y.; Ray, M.; Luo, X.; Das, R.; Landis, R. F.; Farkas, M. E.; Rotello, V. M. Nanocapsule-Mediated Cytosolic SiRNA Delivery for Anti-Inflammatory Treatment. *J. Control. Release* **2018**, *283* (May), 235–240.

(7)   Abrams, M. T.; Koser, M. L.; Seitzer, J.; Williams, S. C.; Dipietro, M. A.; Wang, W.; Shaw, A. W.; Mao, X.; Jadhav, V.; Davide, J. P.; et al. Evaluation of Efficacy, Biodistribution, and Inflammation for a Potent SiRNA Nanoparticle: Effect of Dexamethasone Co-Treatment. *Mol. Ther.* **2010**, *18* (1), 171–180.

(8)   Whitehead, K. A.; Langer, R.; Anderson, D. G. Knocking down Barriers: Advances in SiRNA Delivery. *Nat. Rev. Drug Discov.* **2009**, *8* (2), 129–138.

(9)   Yang, X. C.; Samanta, B.; Agasti, S. S.; Jeong, Y.; Zhu, Z. J.; Rana, S.; Miranda, O. R.; Rotello, V. M. Drug Delivery Using Nanoparticle-Stabilized Nanocapsules. *Angew. Chem. Int. Ed.* **2011**, *50* (2), 477–481.

(10)   Hoffmann, E. De; Stroobant, V. *Mass Spectrometry Principles and Applications Third Edition*; 2007.

(11)   Tang, R.; Kim, C. S.; Solfiell, D. J.; Rana, S.; Mout, R.; Velázquez-Delgado, E. M.; Chompoosor, A.; Jeong, Y.; Yan, B.; Zhu, Z. J.; et al. Direct Delivery of Functional Proteins and Enzymes to the Cytosol Using Nanoparticle-Stabilized Nanocapsules. *ACS Nano* **2013**, *7* (8), 6667–6673.

(12)   De Jong, W. H.; Hagens, W. I.; Krystek, P.; Burger, M. C.; Sips, A. J. A. M.; Geertsma, R. E. Particle Size-Dependent Organ Distribution of Gold Nanoparticles after Intravenous Administration. *Biomaterials* **2008**, *29* (12), 1912–1919.

(13)   Wilhelm, S.; Tavares, A. J.; Dai, Q.; Ohta, S.; Audet, J.; Dvorak, H. F.; Chan, W. C. W. Analysis of Nanoparticle Delivery to Tumours. *Nat. Rev. Mater.* **2016**, *1* (5), 16014.

(14)   Gunawan, C.; Lim, M.; Marquis, C. P.; Amal, R. Nanoparticle-Protein Corona Complexes Govern the Biological Fates and Functions of Nanoparticles. *J. Mater. Chem. B* **2014**, *2* (15), 2060–2083.

(15)   Zhang, Y.; Cai, K.; Li, C.; Guo, Q.; Chen, Q.; He, X.; Liu, L.; Zhang, Y.; Lu, Y.; Chen, X.; et al. Macrophage-Membrane-Coated Nanoparticles for Tumor-Targeted Chemotherapy. *Nano Lett.* **2018**, *18* (3), 1908–1915.

(16)   Albanese, A.; Tang, P. S.; Chan, W. C. W. The Effect of Nanoparticle Size, Shape, and Surface Chemistry on Biological Systems. *Annu. Rev. Biomed. Eng.* **2012**, *14* (1), 1–16.

(17)   Borges Da Silva, H.; Fonseca, R.; Pereira, R. M.; Cassado, A. A.; Álvarez, J. M.; D'Império Lima, M. R. Splenic Macrophage Subsets and Their Function during Blood-Borne Infections. *Front. Immunol.* **2015**, *6*, 480.

(18)   Elci, S. G.; Jiang, Y.; Yan, B.; Kim, S. T.; Saha, K.; Moyano, D. F.; Yesilbag Tonga, G.; Jackson, L. C.; Rotello, V. M.; Vachet, R. W. Surface Charge Controls the Suborgan Biodistributions of Gold Nanoparticles. *ACS Nano* **2016**, *10* (5), 5536–5542.

(19)   Elci, S. G.; Yesilbag Tonga, G.; Yan, B.; Kim, S. T.; Kim, C. S.; Jiang, Y.; Saha, K.; Moyano, D. F.; Marsico, A. L. M.; Rotello, V. M.; et al. Dual-Mode Mass Spectrometric Imaging for Determination of in Vivo Stability of Nanoparticle Monolayers. *ACS Nano* **2017**, *11* (7), 7424–7430.

(20)   Castellanos-García, L. J.; Gokhan Elci, S.; Vachet, R. W. Reconstruction, Analysis, and Segmentation of LA-ICP-MS Imaging Data Using Python for the Identification of Sub-Organ Regions in Tissues. *Analyst* **2020,** *145* (10), 3705-3712.

(21)   Sussulini, A.; Becker, J. S.; Becker, J. S. Laser Ablation ICP-MS: Application in Biomedical Research. *Mass Spectrom. Rev*. **2017**, *36* (1), 47-57.

(22)   Sikora, K. N.; Hardie, J. M.; Castellanos-García, L. J.; Liu, Y.; Reinhardt, B. M.; Farkas, M. E.; Rotello, V. M.; Vachet, R. W. Dual Mass Spectrometric Tissue Imaging of Nanocarrier Distributions and Their Biochemical Effects. *Anal. Chem.* **2020**, *92* (2), 2011–2018.

(23)   Buchberger, A. R.; DeLaney, K.; Johnson, J.; Li, L. Mass Spectrometry Imaging: A Review of Emerging Advancements and Future Insights. *Anal. Chem.* **2018**, *90* (1), 240-265.

(24)   Hardie, J.; Jiang, Y.; Tetrault, E. R.; Ghazi, P. C.; Tonga, G. Y.; Farkas, M. E.; Rotello, V. M. Simultaneous Cytosolic Delivery of a Chemotherapeutic and SiRNA Using Nanoparticle-Stabilized Nanocapsules. *Nanotechnology* **2016**, *27* (37), 374001.

(25) Jiang, Y.; Tang, R.; Duncan, B.; Jiang, Z.; Yan, B.; Mout, R.; Rotello, V. M. Direct Cytosolic Delivery of SiRNA Using Nanoparticle-Stabilized Nanocapsules. *Angew. Chem. Int. Ed.* **2015**, *54* (2), 506–510.

(26) Wallace, M.; Morris, C.; O'Grada, C. M.; Ryan, M.; Dillon, E. T.; Coleman, E.; Gibney, E. R.; Gibney, M. J.; Roche, H. M.; Brennan, L. Relationship between the Lipidome, Inflammatory Markers and Insulin Resistance. *Mol. Biosyst.* **2014**, *10* (6), 1586–1595.

(27) Elci, S. G.; Yan, B.; Kim, S. T.; Saha, K.; Jiang, Y.; Klemmer, G. A.; Moyano, D. F.; Tonga, G. Y.; Rotello, V. M.; Vachet, R. W. Quantitative Imaging of 2 Nm Monolayer-Protected Gold Nanoparticle Distributions in Tissues Using Laser Ablation Inductively-Coupled Plasma Mass Spectrometry (LA-ICP-MS). *Analyst* **2016**, *141* (8), 2418–2425.

(28) Yan, B.; Kim, S. T.; Kim, C. S.; Saha, K.; Moyano, D. F.; Xing, Y.; Jiang, Y.; Roberts, A. L.; Alfonso, F. S.; Rotello, V. M.; et al. Multiplexed Imaging of Nanoparticles in Tissues Using Laser Desorption/Ionization Mass Spectrometry. *J. Am. Chem. Soc.* **2013**, *135* (34), 12564–12567.

(29) Arvizo, R. R.; Miranda, O. R.; Moyano, D. F.; Walden, C. A.; Giri, K.; Bhattacharya, R.; Robertson, J. D.; Rotello, V. M.; Reid, J. M.; Mukherjee, P. Modulating Pharmacokinetics, Tumor Uptake and Biodistribution by Engineered Nanoparticles. *PLoS One* **2011**, *6* (9), 3–8.

(30) Klein, O.; Strohschein, K.; Nebrich, G.; Fuchs, M.; Thiele, H.; Giavalisco, P.; Duda, G. N.; Winkler, T.; Kobarg, J. H.; Trede, D.; et al. Unraveling Local Tissue Changes within Severely Injured Skeletal Muscles in Response to MSC-Based Intervention Using MALDI Imaging Mass Spectrometry. *Sci. Rep.* **2018**, *8* (1), 12677.

(31) Gemoll, T.; Miroll, E.; Klein, O.; Lischka, A.; Eravci, M.; Thorns, C.; Habermann, J. K. Spatial UBE2N Protein Expression Indicates Genomic Instability in Colorectal Cancers. *BMC Cancer* **2019**, *19* (1), 710.

(32) Kihara, M.; Matsuo-Tezuka, Y.; Noguchi-Sasaki, M.; Yorozu, K.; Kurasawa, M.; Shimonaka, Y.; Hirata, M. Visualization of 57 Fe-Labeled Heme Isotopic Fine Structure and Localization of Regions of Erythroblast Maturation in Mouse Spleen by MALDI FTICR-MS Imaging. *J. Am. Soc. Mass Spectr.* **2017**, *28* (11), 2469-2475.

(33) Ifuku, M.; Katafuchi, T.; Mawatari, S.; Noda, M.; Miake, K.; Sugiyama, M.; Fujino, T. Anti-Inflammatory/Anti-Amyloidogenic Effects of Plasmalogens in Lipopolysaccharide-Induced Neuroinflammation in Adult Mice. *J. Neuroinflammation* **2012**, *9* (1), 673.

(34) Irie, A.; Yamamoto, K.; Miki, Y.; Murakami, M. Phosphatidylethanolamine Dynamics Are Required for Osteoclast Fusion. *Sci. Rep.* **2017**, *7* (1), 46715.

(35) Cesta, M. F. Normal Structure, Function, and Histology of the Spleen. *Toxicol. Pathol.* **2006**, *34* (5), 455-465.

(36)   Patterson, N. H.; Tuck, M.; Van De Plas, R.; Caprioli, R. M. Advanced Registration and Analysis of MALDI Imaging Mass Spectrometry Measurements through Autofluorescence Microscopy. *Anal. Chem.* **2018**, *90* (21), 12395-12403.

(37)   Jones, M. A.; Cho, S. H.; Patterson, N. H.; Van de Plas, R.; Spraggins, J. M.; Boothby, M. R.; Caprioli, R. M. Discovering New Lipidomic Features Using Cell Type Specific Fluorophore Expression to Provide Spatial and Biological Specificity in a Multimodal Workflow with MALDI Imaging Mass Spectrometry. *Anal. Chem.* **2020**, *92* (10), 7079-7086.

(38)   Flinders, B.; Huizing, L. R. S.; Van Heerden, M.; Cuyckens, F.; Neumann, U. P.; Van Der Laan, L. J. W.; Olde Damink, S. W. M.; Heeren, R. M. A.; Schaap, F. G.; Vreeken, R. J. Cross-Species Molecular Imaging of Bile Salts and Lipids in Liver: Identification of Molecular Structural Markers in Health and Disease. *Anal. Chem.* **2018**, *90* (20) 11835-11846.

(39)   Weiskirchen, R.; Meurer, S. K.; Liedtke, C.; Huber, M. Mast Cells in Liver Fibrogenesis. *Cells* **2019**, *8* (11), 1429.

(40)   Gordon, J. R.; Galli, S. J. Mast Cells as a Source of Both Preformed and Immunologically Inducible TNF-α/Cachectin. *Nature* **1990**, *346* (6281) 274-276.

(41)   Singh, R.; Lillard, J. W. Nanoparticle-Based Targeted Drug Delivery. *Exp. Mol. Pathol.* **2009**, *86* (3), 215–223.

(42)   Khovidhunkit, W.; Kim, M. S.; Memon, R. A.; Shigenaga, J. K.; Moser, A. H.; Feingold, K. R.; Grunfeld, C. Thematic Review Series: The Pathogenesis of Atherosclerosis. Effects of Infection and Inflammation on Lipid and Lipoprotein Metabolism Mechanisms and Consequences to the Host. *J. Lipid Res.* **2004**, *45* (7), 1169–1196.

(43)   Brust, M.; Walker, M.; Bethell, D.; Schiffrin, D. J.; Whyman, R. Synthesis of Thiol-Derivatised Gold Nanoparticles in a Two-Phase Liquid–Liquid System. *J. Chem. Soc., Chem. Commun.* **1994**, *7*, 801–802.

(44)   Hostetler, M. J.; Templeton, A. C.; Murray, R. W. Dynamics of Place-Exchange Reactions on Monolayer-Protected Gold Cluster Molecules. *Langmuir* **1999**, *15* (11), 3782–3789.

MASS SPECTROMETRY IMAGING REVEALS UNEXPECTED

BIOCHEMICAL EFFECTS OF NANO-BASED DRUG DELIVERY VEHICLES

4.1 Introduction

Nanodelivery vehicles are dynamic systems, containing many functional parts in addition to an active therapeutic (Figure 1.5).[1,2] For instance, the nanoparticle stabilized capsules (NPSCs) introduced in Chapters 2 & 3 are composed of a gold nanoparticle (AuNP)-based shell, a fatty acid droplet core, and an siRNA targeting a specific pathway (Figure 4.1).[3,4] The siRNA is the active constituent of the delivery vehicle, with a predicted biochemical response, however, the other portions of the nanodelivery vehicle, while not targeting a specific pathway, are not necessarily inactive and may still affect biological systems they encounter. It is therefore important to not only evaluate how these materials distribute *in vivo*, but also determine what biochemical role the vehicles themselves have when distributed to their target sites.
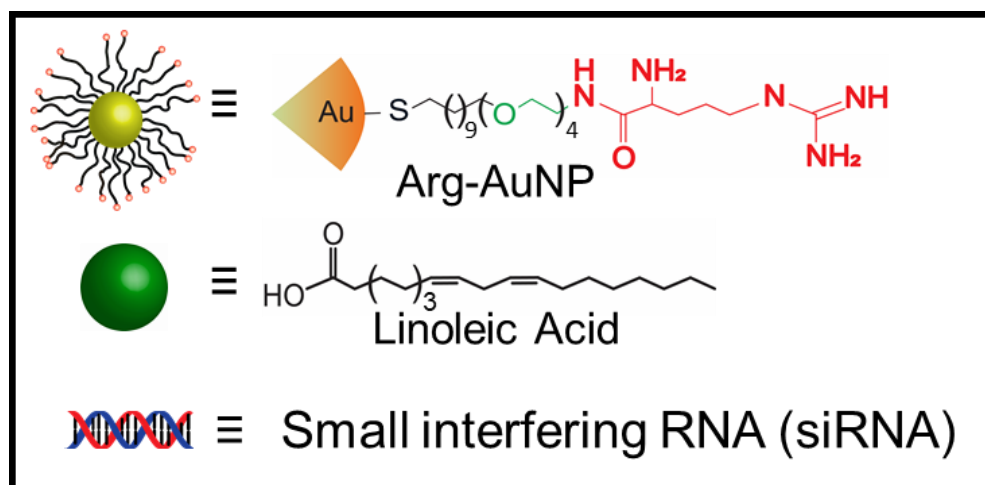
Figure 4.1. Nanoparticle stabilized capsule components.

Various "-omics" focusing on proteins, genes, and lipids, can be exploited to rapidly evaluate the health of an organism. Lipidomics is particularly attractive for assessing biochemical status due to the high concentration of lipids *in vivo* as well as the many signaling, inflammatory, and disease pathways that lipids are involved in.[5] Lipidomic studies have previously been utilized to evaluate the dysregulation of lipids in various tissues as a marker of inflammation and disease,[6–8] but without spatial context, these studies are limited in the information they provide. As mentioned in sections 2.1 and 3.1, it is important to provide spatial context to the accumulation of both the nanomaterial and biochemical changes of the deliverable therapeutic. Although the delivery vehicle may be residing in one sub-organ region, the therapeutic-induced biochemical effects may be occurring in a different sub-organ region, independently of the carrier distribution. This information is a key aspect for assessing not only which regions and biochemical pathways are being affected by the delivered therapeutic, but also can better illustrate the efficacy of the nanodelivery vehicle itself in the tissue it distributes to

Mass spectrometry imaging (MSI) methods provide a platform to rapidly monitor hundreds of lipids simultaneously while also providing site-specific information in affected tissues.[9] Dual-mode mass spectrometry imaging is especially attractive for evaluating the biochemical effect of nanodelivery vehicles due to the ability to assess the correlation between carrier distribution and subsequent biochemical effects in a site-specific manner.[10]

As shown in Chapters 2 & 3, the spatial correlation between predicted lipid responses and nanocarrier distributions in NPSC-injected mice tissues has been thoroughly evaluated. Through these studies, most predicted changes were qualitatively and quantitatively determined to be occurring independently of AuNP distribution. However, there were

many unpredicted lipid changes that occurred, some of which correlated strongly with the AuNP carrier *in situ*. Utilizing this imaging platform, the sources of predicted and unexpected biochemical changes, based on the known biochemistry of TNF-α knockdown and lipid metabolism, are investigated.

4.2 Results and Discussion

In order to evaluate the effect of the individual NPSCs components, we injected mice with the NPSCs containing a TNF-α-targeting siRNA, NPSCs containing a scrambled siRNA, as well as pure arginine gold nanoparticles (Arg AuNPs). By evaluating each of these increasingly less-complex systems, the roles of the TNF-α siRNA, linoleic acid droplet core, and Arg AuNP carrier will be assessed, respectively. As previously mentioned, TNF-α NPSCs predominantly accumulate in the liver and spleen tissues when injected in mice, which is expected based on the accumulation of nanoparticles in the mononuclear phagocytic system (MPS).[11] ICP-MS digestion analysis reveals that
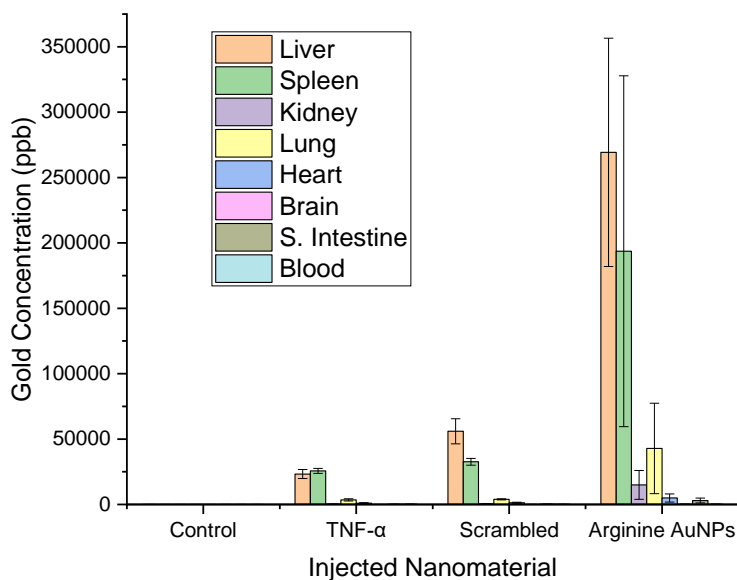
Figure 4.2. ICP-MS gold analysis of digestions of nanomaterial-injected mouse tissues.
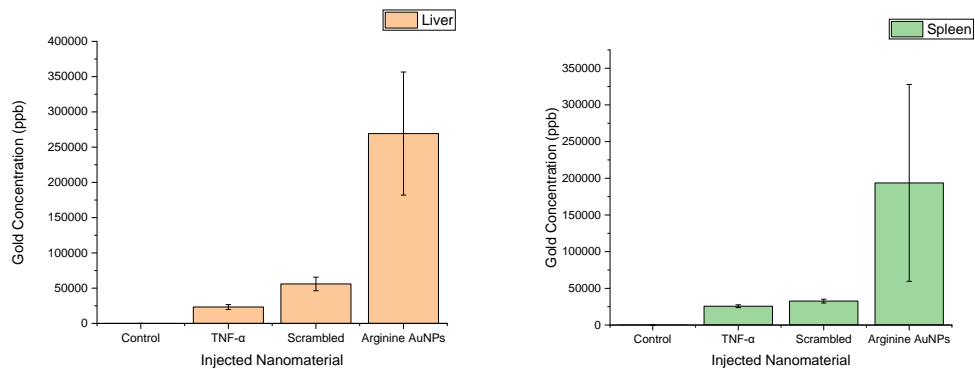
Figure 4.3. ICP-MS gold distributions in the liver (left) and spleen (right) tissues of treated mice.
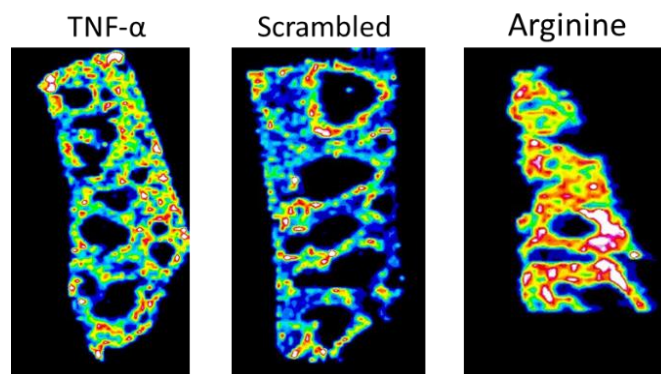
Figure 4.4. LA-ICP-MS images of gold distribution in the spleen of TNF-α NPSC, scrambled NPSC, and arginine AuNP-injected mice. Note the accumulation of gold falls in the red pulp of all tissue types.
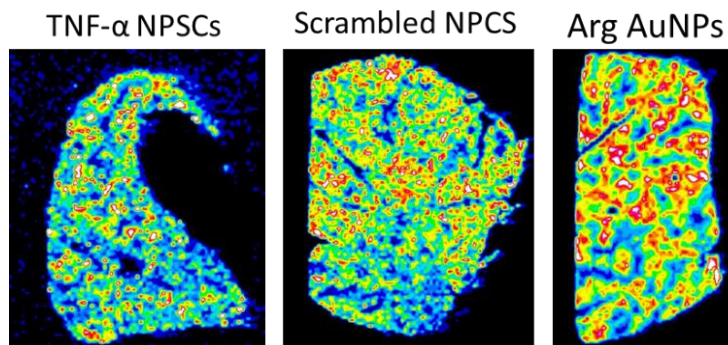
Figure 4.5. LA-ICP-MS images of gold distribution in the liver of TNF-α NPSC, scrambled NPSC, and arginine AuNP-injected mice. Note the punctate distribution is consistent through all tissue types.

scrambled NPSCs and Arg AuNPs also exhibit similar distributions in tissues, with gold predominantly accumulating in the spleen and liver tissues (Figures 4.2 & 4.3).

LA-ICP-MS analysis also reveal that the gold distributes similarly in the sub-organ regions of the liver and spleen for all injected nanomaterials (Figures 4.4 & 4.5). In the spleen tissues the gold accumulates predominantly in the red pulp of the spleen (Figures 3.5, 3.6, & 4.4) and in the liver the gold exhibits a punctate distribution indicative of hepatocyte accumulation (Figure 4.5).[12] Due to the readily distinguishable sub-organ regions, LA-ICP-MS data suggest that all nanomaterial types have similar fates *in vivo* in the spleen. The component that is shared between all three conditions is the Arg AuNP carrier. It can therefore be inferred that the distribution of the AuNP carrier is not influenced by other the other working components (i.e. linoleic acid or siRNA) in the spleen tissues. In the liver, all three nanomaterial types distribute in similar punctate patterns in tissues. It is possible that these distribution patterns are the results of hepatocyte accumulation, however, because the hepatocytes do not cluster in a readily identifiable way in the liver as they do in the red and white pulp of the spleen, additional microscopy analysis should be conducted in order to confirm this occurrence in scrambled NPSC and Arg AuNP-injected mice liver tissues.

4.2.1 Evaluating biochemical effects of NPSCs on the spleen

In the spleen tissue, of the lipids predicted to be affected by TNF-α knockdown, 33 lipids behave as expected in TNF-α NPSC-injected mice.[10] Of these lipid changes, eight were found to be altered as predicted in the spleen of scrambled NPSC-injected mice and one in the spleen of Arg AuNP-injected mice (Table 3.1). This indicates that 76% of the lipid responses can be exclusively associated with the active siRNA knockdown. For
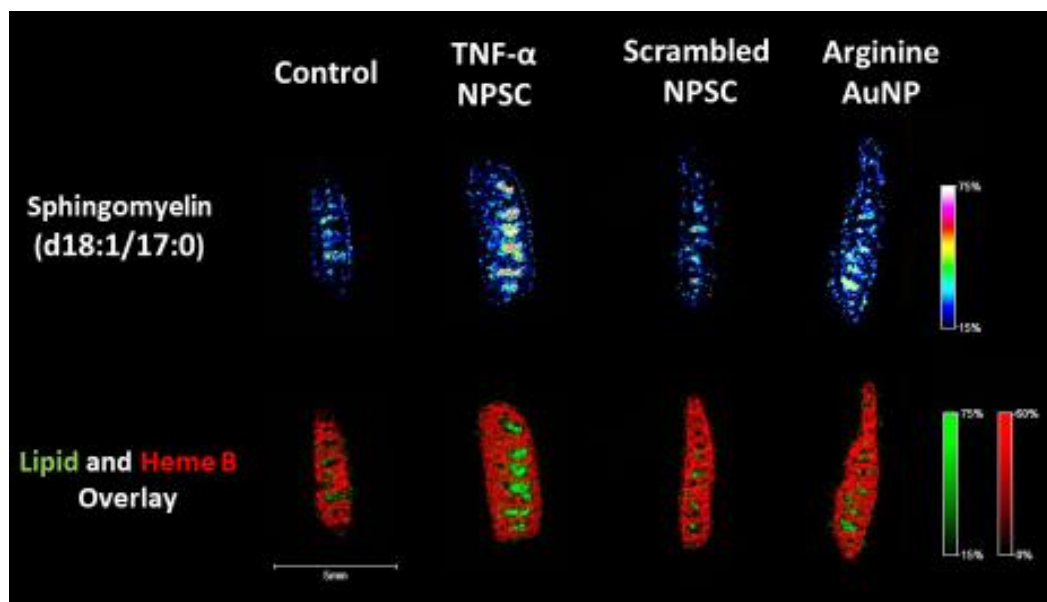
Figure 4.6. MALDI images of spleen tissues of nanomaterial injected mice. Top sets of images show just the lipid of interest and bottom images combine the lipid with heme B to assess the sub-organ distribution of the lipid. Based on the minimal overlap with heme B, as indicated by minimal yellow pixels in the bottom set of images,[10] this lipid appears to be changing in the white pulp of the TNF-α NPSC-injected mouse spleen.

example, sphingomyelin (SM) (d18:1/17:0) is a lipid known to be associated with TNF-α knockdown and it only changes as predicted in the white pulp of TNF-α NPSC spleen tissues (Figure 4.6).

Injection of TNF-α NPSCs also results in 11 unexpected changes with 64% of these changes occurring in the red pulp of the spleen.[10] When observing the changes in the scrambled NPSPCs and Arg AuNP spleen tissues, we see that 5 and 4 unexpected changes overlap with the unexpected changes in the red pulp of the TNF-α NPSC spleen, respectively. For example, SM (d18:1/24:3) is a TNF-α knockdown-associated lipid that changes in an unexpected manner in the red pulp across all three treated tissue types (Figure 4.7). One of the fatty acid chains of Sphingomyelin (d18:1/24:3), docosahexaenoic acid (DHA), is known to be a mediator of anti-inflammatory responses in tissues, including the spleen.[13–15] An unexpected increase in a SM molecule containing this fatty acid chain
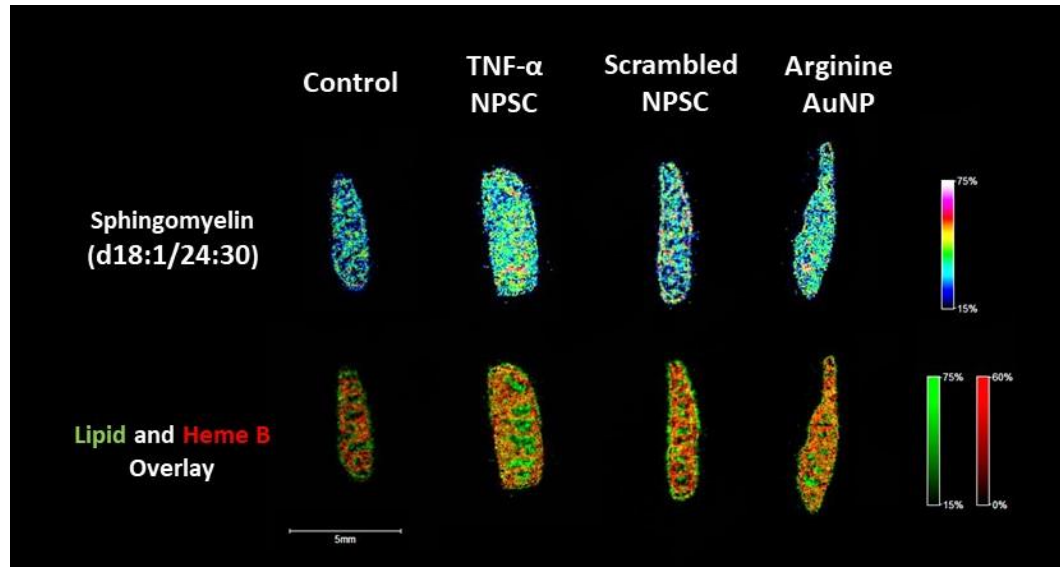
Figure 4.7. MALDI images of spleen tissues of nanomaterial injected mice. Top sets of images show just the lipid of interest and bottom images combine the lipid with heme B to assess the sub-organ distribution of the lipid. Based on the high overlap with heme B, as indicated by intense yellow pixels in the bottom set of images,[10] this lipid appears to be changing in the red pulp of all spleen types.

across all nanomaterial types, specifically in the red pulp where the AuNP nanocarrier is known to distribute (Figure 4.4), may be indicative of the red pulp macrophages responding to the to the uptake of a foreign body (AuNPs) by neutralizing a potential immunological or toxicity response.[16]

In another instance, lysophosphatidylcholine (LPC) (p-18:0) unexpectedly decreases in the red pulp of the spleen of mice injected with TNF-α and scrambled NPSCs, but not Arg AuNPs, suggesting this response is caused by the presence of linoleic acid. Certain LPCs are known to play a role in phospholipid fatty acid incorporation.[17] A free fatty acid chain will combine with an LPC to form a double chain PC. Therefore, the depletion of this particular LPC may be a result of the linoleic acid incorporation to form PC molecules when the NPSCs accumulate in the red pulp of the spleen.

4.2.2 Evaluating biochemical effects of NPSCs on the liver

In the liver, similar patterns arise when compared to the spleen in terms of the effect of the various nanomaterials on the tissue. Although there are fewer overall lipid changes in this liver, we still observe 19 lipids behave as expected in the presence of TNF-α NPSCs. Of these predicted lipid changes, two lipids also change as predicted in the presence of scrambled NPSCs, and one lipid changes in the presence of Arg AuNPs, indicating that the TNF-α siRNA plays the biggest role (89%) in the predicted biochemical changes in the liver. For example, PC (p-36:5) is known to be associated with TNF-α knockdown, and it only changes in the TNF-α NPSC liver tissue (Table 3.2). Because there is no single biochemical marker in MALDI-MSI to discern the liver sub-organ regions, like heme B in the spleen, correlation tables are utilized to assess the lipid distribution patterns (Figure 4.8). The liver is then segregated into the parenchyma, veins, connective tissue, and bile ducts utilizing the MALDI-MS biomarkers indicated in section 3.1 and figure 3.12.

In the correlation plots in figure 4.8, the more greatly two analytes are correlated, the closer their value will be to +1 or 100% correlation. The more greatly two analytes are anti-correlated, the closer their value will be to -1 or -100% correlation. If two analytes are neither correlated nor anti-correlated, their value will be closer to 0 or 0 % correlation. PC (p-36:5) is found to be minimally correlated (-3.6%) with the gold carrier and highly correlated with biomarkers associated with the parenchyma (58.4%) and connective tissue (49.8%). Because this lipid is not altered for other nanomaterials, we can confidently say this change is related to TNF-α knockdown and not the gold carrier distribution in the liver. Additionally, although this analyte response occurs mostly in the parenchyma where the gold is also found, the low correlation value of PC (p-36:5) and gold indicates that the lipid
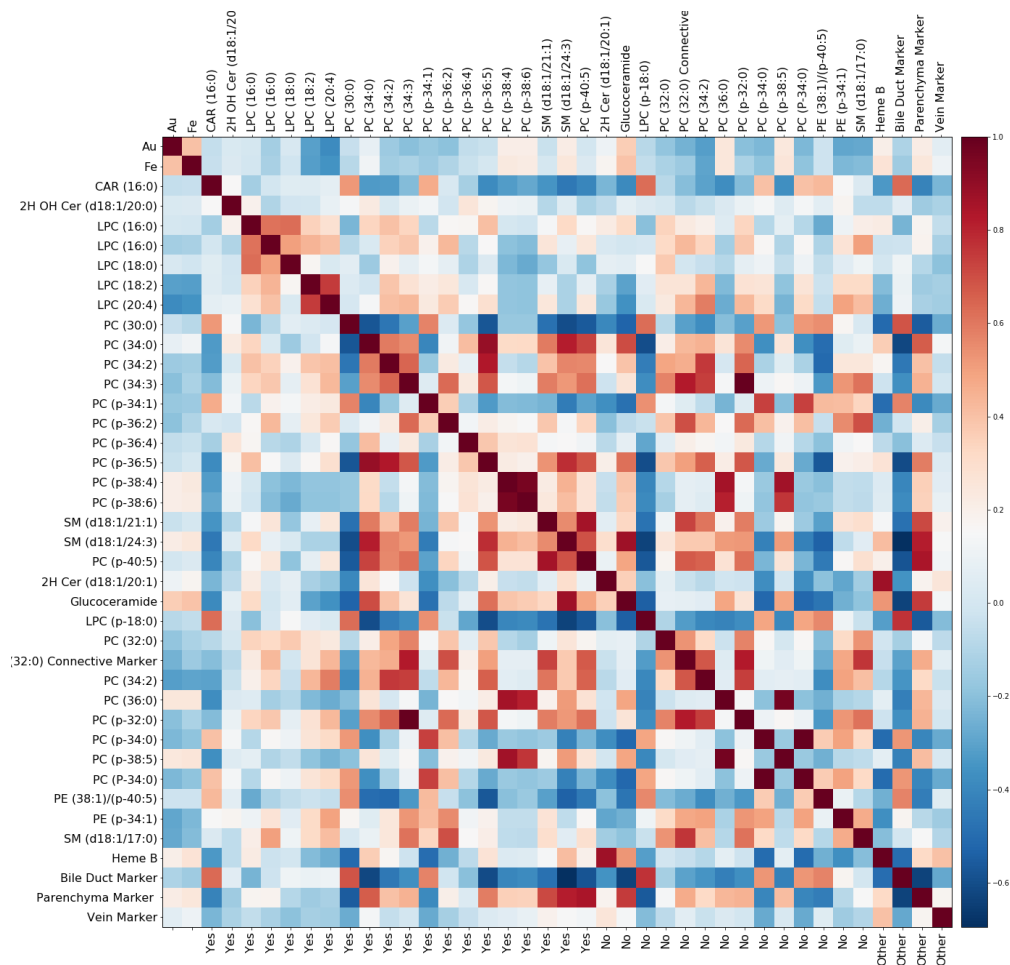
Figure 4.8. Correlation map for LA-ICP-MS analytes (Au, Fe) and MALDI-MSI analytes (lipid classes) with liver sub-organ regions in TNF-α NPSC-injected mice liver tissues. Correlation values of +1 have a dark red color. Correlation values of -1 have a dark blue color. Correlation values of 0 are white.

is still changing independently of the carrier accumulation. This site-specific information would have been otherwise lost in a non-imaging context.

In the liver tissue, there are also nine lipids that change unexpectedly in the presence of TNF-α NPSCs. Of these nine lipids, five also behave unexpectedly in scrambled liver tissues and four in arginine liver tissues. For example, glucosylceramide changes unexpectedly across all three nanomaterial treated mice liver tissues. Ceramide is a pro-apoptotic mediator, which glucosylceramide synthase (GCS) converts to the nonfunctional

compound, glucosylceramide.[18] Glucosylceramides are biomarkers known to be involved in inflammation, and specifically in macrophage uptake in the liver, spleen, and kidney tissues.[19] This particular unexpected response has a high correlation with the gold signal (77%) and the parenchyma biomarker (38%) (Figure 4.8). This change in lipid response in the liver may be indicative of an acute inflammatory response from the uptake of the nanomaterials in the macrophages of these tissues.

4.3 Conclusions

NPSC components were evaluated by comparing the lipid profiles of TNF-α NPSCS, scrambled NPSCs, and arginine AuNPs in mouse spleen and liver tissues. Based on the analysis of lipid changes, TNF-α NPSCs produced substantially more lipid changes than those in the scrambled NPSC and arginine AuNP tissues for both liver and spleen tissues. Changes observed in scrambled NPSCs spleen tissues, indicate that the linoleic acid may have slight anti-inflammatory effect since eight predicted lipids related to TNF-α knockdown are still observed to change in the spleen of the scrambled NPSC-injected mice. In the liver however, fewer predicted lipid changes arise in the presence of scrambled NPSCs indicating less of an anti-inflammatory effect in this tissue type. Both liver and spleen arginine AuNP tissues only exhibited one predicted lipid changes related to TNF-α knockdown and therefore the AuNPs themselves do not appear to play a major role in the TNF-α-mediated anti-inflammatory response in either tissue.

Conversely, many of the unpredicted changes overlap between the TNF-α NPSC, scrambled NPSC, and Arg AuNP-injected mice spleen and liver tissues. An unexpected increase of an inflammatory regulator was observed in the red pulp of the spleen in the presence of all nanomaterial treatments, indicating a potential response to the uptake of the

AuNP nanocarrier itself. There was also an unexpected increase of an inflammatory marker in the parenchyma of the liver in the presence of all the nanomaterial types, indicating a potential inflammatory effect of the Arg AuNPs in these tissues. Linoleic acid also seems to play a role in the anti-inflammatory response of the spleen tissues due to the significant number of analytes that are altered in the presence of scrambled NPSCs. These results not only suggest that the inactive components of NPSCs could be altering their therapeutic effect, but also illustrate the importance of evaluating nano-based delivery vehicles in their entirety.

Utilizing our dual-mode imaging method, we can qualitatively and quantitatively assess the various components of nano-based delivery vehicles *in vivo*. The spatial context provided is valuable in providing biochemical context of both the predicted and unpredicted responses of the TNF-α siRNA, linoleic acid, and Arg AuNPs. Overall, the TNF-α NPSCs are affecting their treated tissues in a predicted, and localized manner. The changes mostly arise independently of the carriers location, however there are some changes that occurring where the carrier is located, and these changes may be related to the biochemical effect the linoleic acid and AuNPs have on the system itself.

4.4 Experimental

All reagents, materials, equipment, as well as methods for mouse handling, mass spectrometry imaging protocols, and statistical evaluation of both MALDI and LA-ICP-MS images can be found in the cited reference.[10] For additional statistical analysis and data processing see section 3.4.

4.5 References

(1)   Li, Z.; Tan, S.; Li, S.; Shen, Q.; Wang, K. Cancer Drug Delivery in the Nano Era: An Overview and Perspectives. *Oncol. Rep.* **2017**, *38* (2), 611–624.

(2)   Babu, A.; Templeton, A. K.; Munshi, A.; Ramesh, R. Nanodrug Delivery Systems: A Promising Technology for Detection, Diagnosis, and Treatment of Cancer. *AAPS PharmSciTech* **2014**, *15* (3), 709–721.

(3)   Yang, X. C.; Samanta, B.; Agasti, S. S.; Jeong, Y.; Zhu, Z. J.; Rana, S.; Miranda, O. R.; Rotello, V. M. Drug Delivery Using Nanoparticle-Stabilized Nanocapsules. *Angew. Chem. Int. Ed.* **2011**, *50* (2), 477–481.

(4)   Jiang, Y.; Hardie, J.; Liu, Y.; Ray, M.; Luo, X.; Das, R.; Landis, R. F.; Farkas, M. E.; Rotello, V. M. Nanocapsule-Mediated Cytosolic SiRNA Delivery for Anti-Inflammatory Treatment. *J. Control. Release* **2018**, *283* (May), 235–240.

(5)   Harkewicz, R.; Dennis, E. A. Applications of Mass Spectrometry to Lipids and Membranes. *Annu. Rev. Biochem.* **2011**, *80* (1), 301–325.

(6)   Cecile Martel; Davide Degli Esposti; Antonin Bouchet; Catherine Brenner; Antoinette Lemoine. Non-Alcoholic Steatohepatitis: New Insights from OMICS Studies. *Curr. Pharm. Biotechnol.* **2012**, *13* (5), 726-735.

(7)   Bermúdez-López, M.; Arroyo, D.; Betriu, À.; Masana, L.; Fernández, E.; Valdivielso, J. M. New Perspectives on CKD-Induced Dyslipidemia. *Expert Opin. Ther. Targets* **2017**, *21* (10), 967–976.

(8)   Osae, E. A.; Steven, P.; Redfern, R.; Hanlon, S.; Smith, C. W.; Rumbaut, R. E.; Burns, A. R. Dyslipidemia and Meibomian Gland Dysfunction: Utility of Lipidomics and Experimental Prospects with a Diet-Induced Obesity Mouse Model. *Int. J. Mol. Sci.* **2019**, *20* (14), 3505.

(9)   Goto-Inoue, N.; Hayasaka, T.; Zaima, N.; Setou, M. Imaging Mass Spectrometry for Lipidomics. *Biochim. Biophys. Acta - Mol. Cell Biol. Lipids* **2011**, *1811* (11), 961–969.

(10)   Sikora, K. N.; Hardie, J. M.; Castellanos-García, L. J.; Liu, Y.; Reinhardt, B. M.; Farkas, M. E.; Rotello, V. M.; Vachet, R. W. Dual Mass Spectrometric Tissue Imaging of Nanocarrier Distributions and Their Biochemical Effects. *Anal. Chem.* **2020**, *92* (2), 2011–2018.

(11)   Wilhelm, S.; Tavares, A. J.; Dai, Q.; Ohta, S.; Audet, J.; Dvorak, H. F.; Chan, W. C. W. Analysis of Nanoparticle Delivery to Tumours. *Nat. Rev. Mater.* **2016**, *1* (5), 16014.

(12)   Elci, S. G.; Jiang, Y.; Yan, B.; Kim, S. T.; Saha, K.; Moyano, D. F.; Yesilbag Tonga, G.; Jackson, L. C.; Rotello, V. M.; Vachet, R. W. Surface Charge Controls the Suborgan Biodistributions of Gold Nanoparticles. *ACS Nano* **2016**, *10* (5), 5536–5542.

(13)   Raederstorff, D.; Pantze, M.; Bachmann, H.; Moser, U. Anti-Inflammatory Properties of Docosahexaenoic and Eicosapentaenoic Acids in Phorbol-Ester-Lnduced Mouse Ear Inflammation. *Int. Arch. Allergy Immunol.* **1996**, *111* (3), 284–290.

(14)   Berry, K. A. Z.; Li, B.; Reynolds, S. D.; Barkley, R. M.; Gijón, M. A.; Hankin, J. A.; Henson, P. M.; Murphy, R. C. MALDI Imaging MS of Phospholipids in the Mouse Lung. *J. Lipid Res.* **2011**, *52* (8), 1551–1560.

(15)   de Visser, H. M.; Mastbergen, S. C.; Ravipati, S.; Welsing, P. M. J.; Pinto, F. C.; Lafeber, F. P. J. G.; Chapman, V.; Barrett, D. A.; Weinans, H. Local and Systemic Inflammatory Lipid Profiling in a Rat Model of Osteoarthritis with Metabolic Dysregulation. *PLoS One* **2018**, *13* (4), e0196308.

(16)   Gustafson, H. H.; Holt-Casper, D.; Grainger, D. W.; Ghandehari, H. Nanoparticle Uptake: The Phagocyte Problem. *Nano Today* **2015**, *10* (4), 487–510.

(17)   Law, S.-H.; Chan, M.-L.; Marathe, G. K.; Parveen, F.; Chen, C.-H.; Ke, L.-Y. An Updated Review of Lysophosphatidylcholine Metabolism in Human Diseases. *Int. J. Mol. Sci.* **2019**, *20* (5), 1149.

(18)   Singh, R.; Lillard, J. W. Nanoparticle-Based Targeted Drug Delivery. *Exp. Mol. Pathol.* **2009**, *86* (3), 215–223.

(19)   Khovidhunkit, W.; Kim, M.-S.; Memon, R. A.; Shigenaga, J. K.; Moser, A. H.; Feingold, K. R.; Grunfeld, C. Thematic Review Series: The Pathogenesis of Atherosclerosis. Effects of Infection and Inflammation on Lipid and Lipoprotein Metabolism Mechanisms and Consequences to the Host. *J. Lipid Res.* **2004**, *45* (7), 1169–1196.

CHAPTER 5

QUANTITATIVE DIFFERENTIATION OF CELL SURFACE-BOUND AND INTERNALIZED CATIONIC GOLD NANOPARTICLES USING MASS SPECTROMETRY

Abstract:

Differentiation between cell surface-bound and internalized nanoparticles is challenging yet essential for accurately quantifying cellular uptake. Here, we describe a versatile mass spectrometry-based method that allows separate quantification of both cell surface-bound and internalized nanoparticles. This rapid method uses tuned laser fluencies to selectively desorb and ionize cell surface-bound cationic gold nanoparticles from intact cells, providing quantification of external particles. Overall nanoparticle quantities are obtained from the cell lysates, with subtraction of external particles from the total amount providing quantification of nanoparticles taken up by cells. The utility of this strategy was demonstrated through simultaneous quantitative determination of how cell-surface proteoglycans influence nanoparticle binding and uptake into cells.

5.1 Introduction

The ability to finely control the size,[1] shape,[2] and surface properties[3] of nanoparticles (NPs) coupled with their ability to provide controlled release[4,5] makes them potent carriers

for cellular delivery of therapeutics. The unique optical and magnetic properties of NP cores likewise make them important imaging reagents.[6,7] The localization of these materials is, however, essential to their utility with efficiency of cellular uptake is a key figure of merit in the engineering of NPs for biomedical applications. Most strategies for achieving uptake, however, rely on modification of NPs with ligands designed to interact with specific receptors or to interact strongly with the plasma membrane.[8,9] Both strategies will generate simultaneous cell surface adhesion and internalization, with very different therapeutic/imaging outcomes for these two locations.

Despite the central importance of quantifying cellular uptake, quantitative differentiation of internalized and cell surface-bound NPs remains a significant challenge.[10] In order to construct a comprehensive picture of nanoparticle adhesion and uptake, distribution, quantification, and multiplex tracking must all be addressed. Optical and microscopic techniques have been the most valuable in this regard. Confocal[11] and fluorescence microscopy[12] as well as transmission electron microscopy (TEM)[13] are reliable methods for measuring the distribution of NPs on a cellular level. These methods can typically distinguish between NPs bound to the cell surface and those that have been internalized. In some cases, the sub-cellular distributions can also be determined, but simultaneous measurements of multiple NP types can be challenging.

Quantitative measurements of NP uptake into cells rely on methods such as inductively-coupled plasma mass spectrometry (ICP-MS)[14] and flow cytometry.[15,16] These methods are sensitive to a wide variety of materials and provide a relatively high-throughput, quantitative measure of NP uptake. In order to differentiate which particles are

actually internalized as compared to those that are simply adhering to the surface, chemical etching is typically performed.[17,18]

Chemical etching, however, uses toxic reagents and disruptively low ionic strengths that limit its applicability.[19] Molecular mass spectrometric techniques have the potential to provide quantitative information while simultaneously reporting on multiple NPs in their intact state. Our group has previously shown that laser desorption/ionization (LDI) MS is a versatile strategy that can successfully be used to detect a wide range of NPs with different materials and sizes. For example, LDI-MS was used to detect surface monolayers on quantum dots which enables monitoring of intracellular monolayer stability.[20] Magnetic nanoparticle can also facilitate ionization when coupled with LDI-MS, which allows direct determination of ligand composition.[21] Other examples include the imaging of carbon nanomaterials[22] and AuNPs[23] in animal tissues. Widely compatible with different NPs, LDI-MS has been used to determine cellular uptake[24] and monitor stability of NPs in cells.[25] We report here an extension of the LDI-MS method that uses tuned laser fluency to rapidly quantify cell surface-bound and internalized NPs. This LDI-MS method quantitatively distinguishes between cell surface-bound and internalized AuNPs through laser fluency absorption by the NP core that then enables desorption and ionization of the attached monolayers.[26]

A unique benefit of utilizing this new LDI-MS method is that it capable of measuring multiple NPs in a single analysis due to the label-free and multiplex nature inherent to MS. This feature allows for the creation of specific adhesion and uptake profiles of different NPs. The combination of both optical and mass spectrometric methods allows for one to create a comprehensive picture of the uptake of various NPs in biological cells. Using the

94
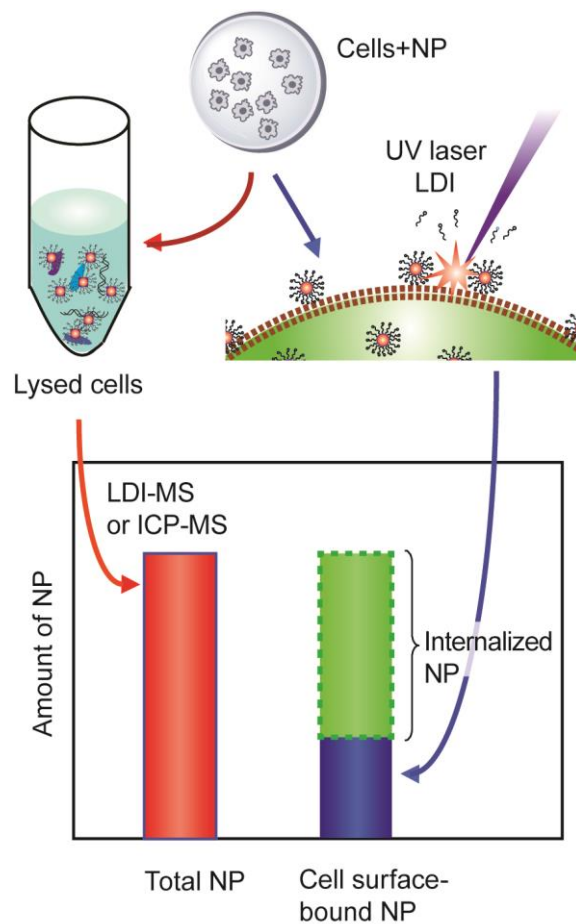
Figure 5.1. Workflow for quantifying total NP, cell surface-bound and internalized NPs using LDI-MS.

LDI-MS method with cell -level optical and quantitative methods enables the quantitative differentiation of extra- and intracellular NP distributions (Figure 5.1). Here, we demonstrate the utility of the LDI-MS method through quantitative assessment of the role of proteoglycans in determining cellular uptake of NPs, a challenging question that requires effective differentiation of surface-bound and internalized NPs.

5.2 Results and Discussion

The hypothesis underlying our research is the laser fluency could be tuned to desorb and ionize monolayers from NPs attached to the outside of intact cells but unable to
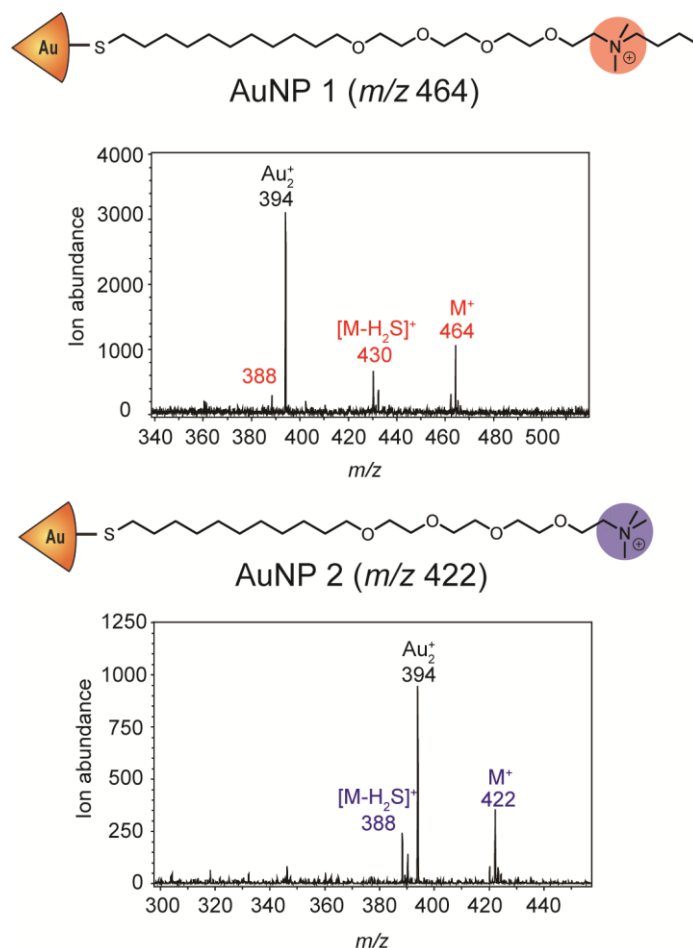
Figure 5.2. Structures of the monolayer-stabilized AuNPs used in this study and the m/z ratios of their molecular ions and major fragments.

penetrate intact cells membrane to desorb and ionize monolayers from NPs inside the cells.

We first determined if AuNPs could be detected on intact cells by studying two cationic

AuNPs (Figure 5.2a). Cells were cultured on poly-lysine coated indium tin oxide (ITO)

glass slide, so that LDI-MS analyses could be performed directly following incubation

without further manipulation of the cells. HeLa cells (20,000 cells) were incubated with

250 nM of AuNP 1 and AuNP 2 in serum-free media for 15 min. After incubation, the cells

were washed and analyzed by LDI-MS. The ligand molecular ion or "mass barcodes" of

AuNP 1 and 2 (m/z 464 and 422, respectively) are readily observed in the mass spectrum,

as are fragment ions (loss of H2S from the ligands) and Au2+ (m/z 394) ions (Figure 5.2b).

We determined the appropriate laser fluency for selectively detecting surface-bound AuNPs using pulse-chase kinetics. AuNPs 1 and 2 were sequentially incubated with the cells, so that AuNP 1 was pushed for internalization. After removal of surface-bound AuNP 1, AuNP 2 was added for cell surface binding, the cell samples analyzed by LDI-MS, with the distinct ligands on two nanoparticles allowing differentiation by LDI-MS. First, 250 nM of AuNP 1 was incubated with HeLa cells in serum free media for 60 min. After incubation, the cells were extensively washed with PBS to remove any AuNP 1 that was still bound to the cell surface. From separate ICP-MS measurements, we found that four wash cycles were sufficient to remove essentially all AuNPs bound to the cell surface (Figure 5.3a), leaving only the internalized AuNPs. In a control experiment using a polylysine-coated glass slide, no signal from AuNPs was detected in LDI-MS after the washing step, confirming that the effect of AuNPs on the substrate after the washing step was negligible (Figure 5.4). After removal of cell-surface bound AuNP 1, 250 nM of AuNP
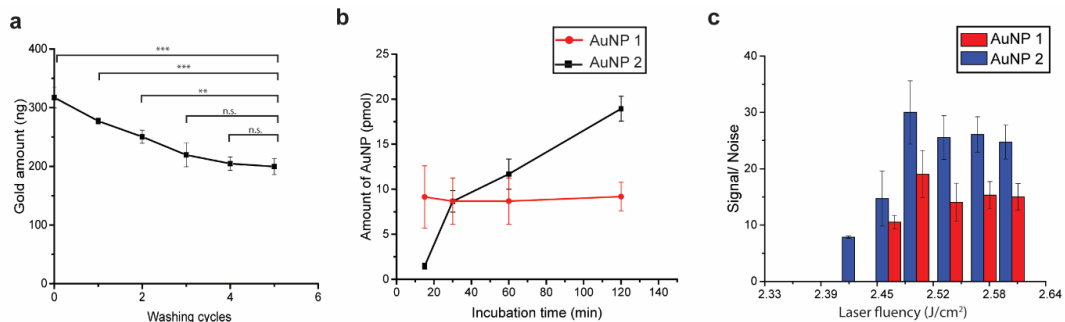
Figure 5.3. Differentiation of cell surface-bound and internalized AuNPs by tuning laser fluency. (a) ICP-MS measurement of AuNP 1 levels in the cells after wash cycles showing essentially complete removal of surface-bound NPs. Paired sample t-test were performed, n=3; ***, $P<0.01$; **, $P<0.05$; n.s., $P>0.05$. (b) LDI-MS quantification of two AuNPs in cell lysate at different AuNP 2 incubation times. Note that AuNP 1 was first incubated for 60 min and then the cell monolayer was washed five times before incubation with AuNP 2. One-way ANOVA were performed on amount of AuNP 1, n=3, $P<0.01$, no significant difference between different time points was identified. (c) LDI-MS detection of AuNPs 1 and 2 from the intact cells. All error bars represent the standard deviation.
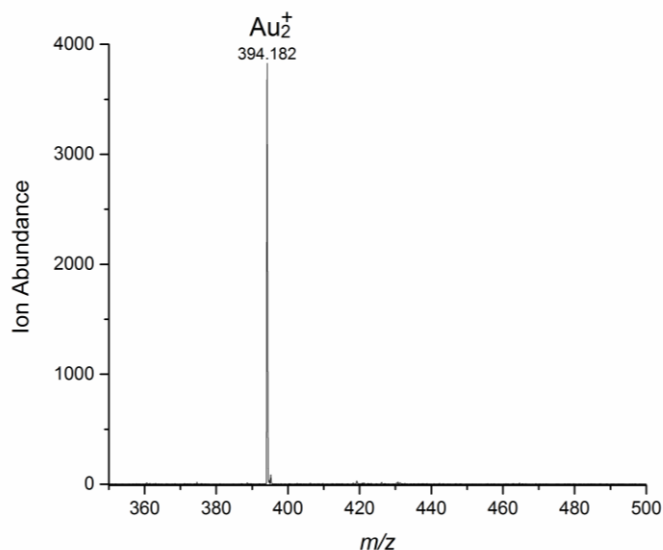
Figure 5.4. LDI-MS detection of AuNPs on plain slide after washing steps. 250 nM AuNP 1 media solution was incubated on poly-lysine coated glass slide for 30 minutes at 37 °C. After the incubation, the AuNP 1 solution was removed and the glass slide was washed with PBS for 5 times, AuNP 2 was then incubated for 30 minutes under the same condition and washed with PBS for one time.

2 was then incubated with the cells for different amounts of time to allow AuNP 2 to both bind to the cell surface and be taken up by the cells. As expected, a greater amount of AuNP 2 is associated with the cells after longer incubation times, as measured by LDI-MS of the cell lysate (Figure 5.3b), indicating that both cell uptake and cell adherence has occurred. During this time the level of AuNP 1 remained unchanged due to the relatively slow rate of exocytosis (Figure 5.3b).[27] We incubated cells with AuNP 1 for 60 min, followed by washing and incubation with AuNP 2, at time points that provided approximately equal total quantities of the two NPs (Figure 5.3b). The cells were then subjected to laser irradiation at different laser fluencies, and mass spectra were acquired. The signal-to-noise ratios (S/N) of the mass barcodes for each NP were then compared (Figure 5.3d). S/N was used to evaluate the level of detection, where a peak of S/N over 5 was considered distinguishable from background and can be used for quantification.[28] Results show that

no ion signal is measured for either AuNP at energies below 2.39 J/cm^2, but as the laser fluency is increased to 2.42 J/cm^2, AuNP 2 is selectively and reproducibly detected. In control experiments using washed and unwashed cells that were incubated with only a single NP, only the unwashed cells provided an ion signal at laser fluencies below 2.45 J/cm^2 (Figure 5.5). As the laser fluency is further increased past 2.45 J/cm^2, both AuNPs can be detected from the intact cells, indicating that higher laser fluencies are sufficient to desorb and ionize NPs both inside and outside the cell. As expected, the NPs outside the cells are detected more efficiently at all the laser fluencies studied (Figure 5.3c), consistent with our initial hypothesis that the cell membrane of intact cells would hinder the desorption/ionization process.

We next performed both energy depletion of cells and cell incubation at 4 °C. After energy depletion with sodium azide and 2-deoxyglucose, we observed both nanoparticles
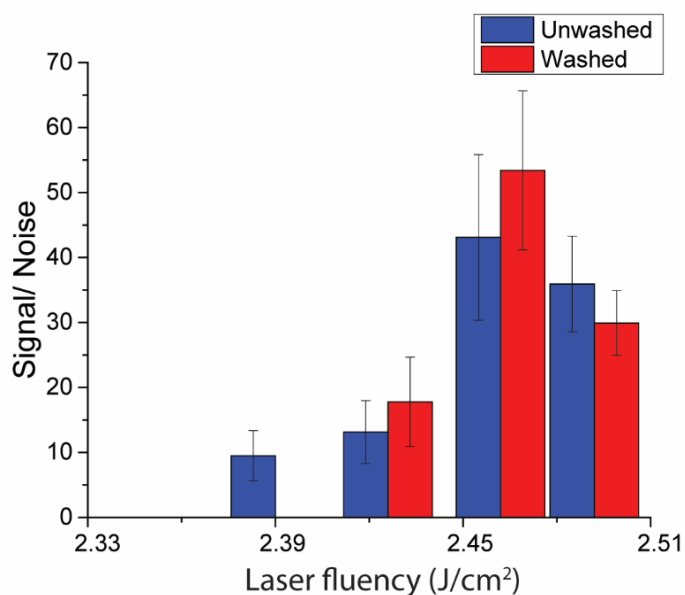
Figure 5.5. LDI-MS of AuNP 2 on cell monolayers before and after washing. 250 nM AuNP 2 was incubated with the cell monolayer for 60 minutes in serum free media at 37 °C. After incubation, the cell monolayer was either washed four times (washed) or one time (unwashed) before LDI-MS analysis.
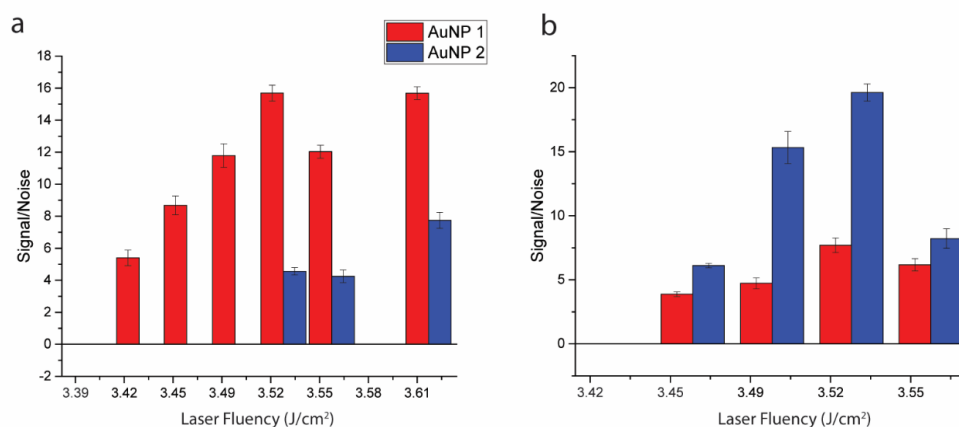
Figure 5.6. a) LDI-MS of HeLa cell monolayer after sequential incubation by AuNP 2 and AuNP 1. b) LDI- MS of HeLa cells monolayers treated with 3mg/ml NaN3 and 50 nM 2-deoxyglucose in DMEM for 30 minutes prior to sequential AuNP incubation.

at lower laser fluency than expected (Figure 5.6), potentially due to the ability of sodium azide to dissociate the cell membrane from the cytoskeleton.[29] Chase particle AuNP 2 was observed at much higher levels than pulse AuNP 1 as expected, with the observation of some level of internalized AuNP 1 consistent with our previous finding has shown that energy depletion cannot prevent internalization of positively charged nanoparticles.[30] For cells incubated at 4 °C, both surface binding and internalization of nanoparticles were reduced to levels that could not be quantified, presumably due to reduced binding kinetics and cellular activity. We also compared our method with chemical etching. After incubating with AuNP 1, one batch of HeLa cells were treated through I_2/KI etching process,[17] whereas another batch was washed with DPBS for five times. We found that cells had dramatic morphological change and reduced cell density after etching compared to non-etched ones (Figure 5.7a), suggesting massive cell death after chemical etching, presumably due to osmotic stress when using the low ionic strength required for this method. Gold content in the supernatant from these samples was measured and compared with the cell surface-bound AuNP measured by LDI-MS (Figure 5.7b). Supernatant from
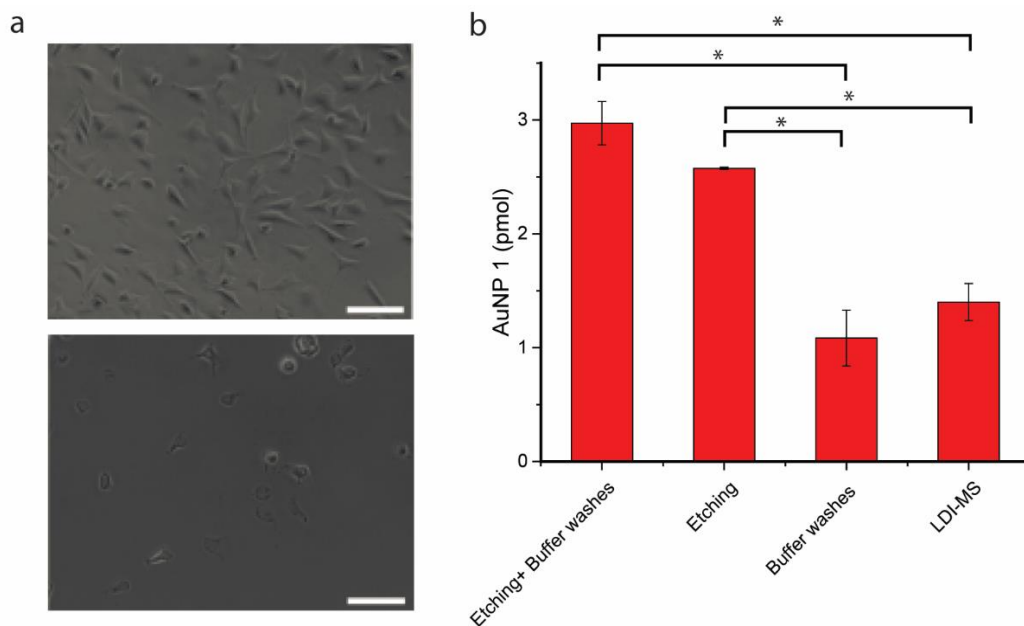
Figure 5.7. a) Microscopic image of HeLa cells not etched (up) and etched (down) by I_2/KI solution. Scale bars: 100µm. b) Comparisons of removal of surface-bound AuNPs via etching and buffer washing measured by ICP-MS. LDI-MS measurement of cell-surface adhered AuNP was added for further comparison. All the experiments were done with HeLa cells incubated with AuNP 1 for 30 minutes. The gold amount measured by ICP-MS in the etched and non-etched samples were converted to AuNP amount through division by 48.62 ng gold/ pmol AuNP. One way-ANOVA ($P<0.05$) was performed, n=3, all error bars represent standard deviation. Stars above the bars indicate significance, whereas no stars suggest not significantly different.

non-etched showed agreement to LDI-MS measurement as one way-ANOVA test showed no significant difference. Interestingly, significantly higher amount of gold was measured for etched samples. Considering the loss of cells shown in Figure 5.7a, it is possible that some AuNPs was removed with the cells unintentionally by the etching process.

We next quantified the cell surface-bound AuNPs using an AuNP internal standard and an external calibration on HepG2 cells. AuNP 1 was used as internal standard; increasing concentrations of AuNP 2 and a fixed concentration of AuNP 1 (100 nM) were incubated with cells for 15 min, during which time minimal NPs were internalized (See Figure 5.8b). After incubation, the intact cells were immediately analyzed by LDI-MS at the laser fluency (*i.e.* 2.42 J/cm^2) that ionized only cell-surface bound AuNPs. Differences in
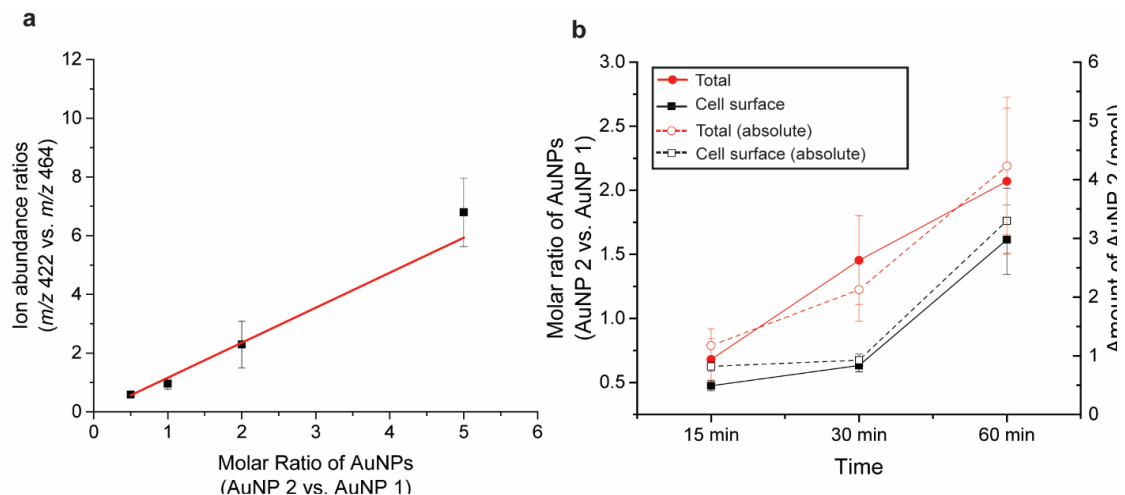
Figure 5.8. Quantification of cell surface-bound and total AuNPs in HepG2 cells. (a) Calibration curve obtained for AuNP 2 (*m/z* 422) when using AuNP 1 (*m/z* 464) as the internal standard (b) Relative amounts (solid) and absolute amount (pmol) (dashed) of AuNPs absorbed on cell surface and associated with the entire cells. The absolute amount of total AuNP 2 was measured by ICP-MS and the absolute amount of cell surface AuNP 2 was determined using the calibration curve.

behavior between cell types requires laser fluency calibration for different cell samples, adding additional experimentation. The resulting ion abundance ratios of the mass barcodes for AuNP 2 (*m/z* 422) and AuNP 1 (*m/z* 464) were plotted against the concentration ratio between the two AuNPs to generate a calibration curve (Figure 5.8a). Using this calibration curve, the relative amounts of AuNP 2 bound to the surface of the cell's monolayer could be determined (black data points in Figure 5.8b). For each incubation time indicated, the internal standard (AuNP 1) was added at 100 nM (12.5 pmol) to the incubated sample and allowed to sit with the cells for 15 minutes before LDI-MS analysis. For comparison, a fraction of the cells was also lysed after different incubation times and the total NP content in the cells was determined by LDI-MS (red data points in Figure 5.8b). The difference between the total (red data) and cell surface bound (black data) amounts allows determination of AuNP 2 internalized (Figure 5.8b). It is worth notice that the amount of

AuNP on cell surface is monotonically, which could be a reflection of cell shape and or surface structure modulation by exposure to positively charged AuNPs.[31,32]

Having established rapid and effctive quantification of nanoparticles, we demonstrated the utility of this method by determining how different cell-surface proteoglycans influence AuNP internalization as a demonstration of the utility of our method. Wild-type Chinese hamster ovary (CHO) cells and two proteoglycan knockdown mutants, CHO-2 (xylosyltransferase 1 deficient) and CHO-3 (galactosyltransferase 1 deficient) cells,[33] were incubated with AuNP 2 and analyzed (Figure 5.9a & 5.10). No measurable cell uptake occurs during the first 15 minutes of incubation, providing a quantitative measure of total NP adsorption in these cells using ICP-MS measurements on the cells at the 15 min time point and using these values to correlate ion abundance ratios and the absolute NP quantity (see Supplementary Information for details). The data in Figure 5.9 summarize the
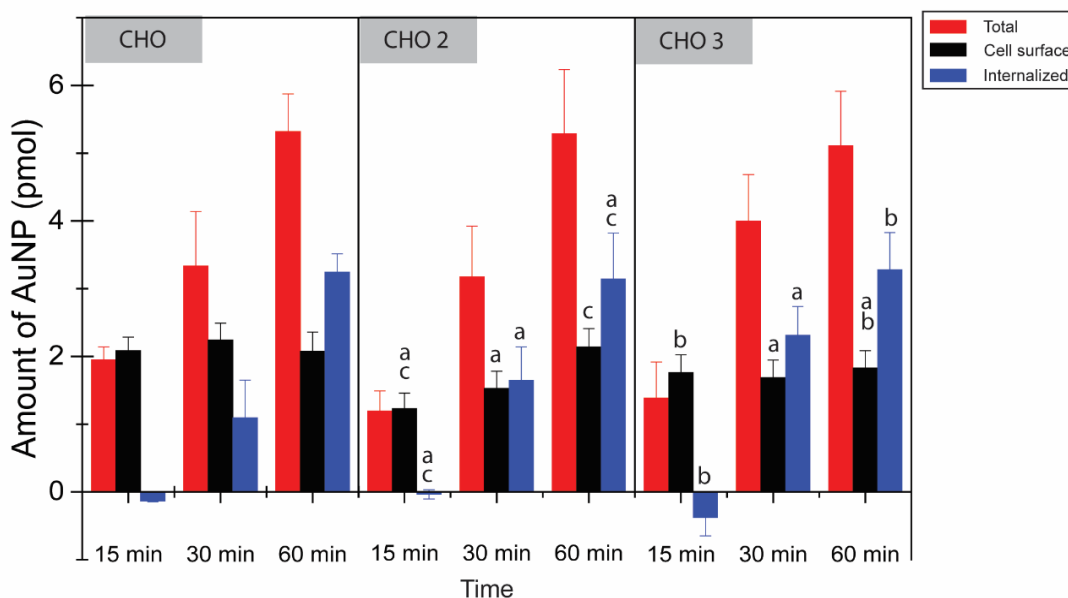
Figure 5.9. Quantities of AuNPs associated with the different CHO cell lines. One way-ANOVA (P<0.01) was performed, n=3, all error bars represent standard deviation. Letters above the bars indicate significance, in which a, b and c are in comparison with CHO, CHO2 and CHO3 at the same time point, respectively.
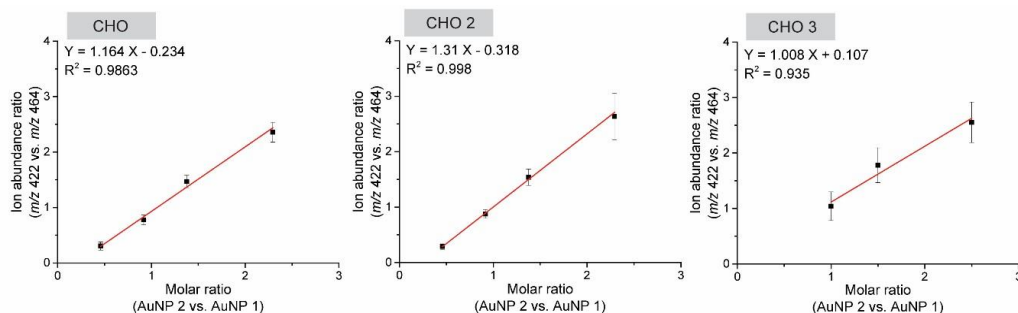
Figure 5.10. LDI-MS calibration curves for AuNP 2 on the cell surface. HeLa, CHO, CHO 2, and CHO 3 cells were cultured on ITO-glass slide. Increasing concentrations of AuNP 2 were mixed with AuNP 1 (internal standard) and incubated with cells as described in the text. Cells on the glass slide were detected using 38.6 µJ to only detect AuNPs on cell surface. Molecular ions of both AuNPs were plotted against molar ratios.

quantitative NP distributions in the three different cell types. Three conclusions can be obtained from these data: 1) The NP amounts on the cell surface do not change significantly during the course of incubation, indicating there is a rapidly achieved equilibrium between cell culture media and plasma membrane. 2) The NP amounts bound to plasma membrane differ based on cell glycosylation. The normal CHO cells have a higher level of cell surface adsorption than the proteoglycan knockdown mutants, consistent with the study by Payne *et al.* that proposed the importance of negatively charged proteoglycans as binding sites for cationic nanomaterials.[34] 3) Despite the difference in particle attachment, there was no significant difference in cellular uptake. Taken together, these studies provide direct evidence of the ability of nanoparticles to differentiate between cell surfaces based on glycosylation, an important issue for sensing[35] and therapeutic strategies.[36]

5.3 Conclusion

We have shown that cell surface-bound AuNPs can be selectively detected and quantified using LDI-MS by choosing the appropriate laser fluency for analysis. Combination of this method with overall NP levels obtained through ICP-MS or LDI-MS of the cell lysate provides quantitative values for cell surface-bound and internalized NP.

This method is rapid, reproducible, and avoids processing conditions that complicate etching-based methods. Given the wide range of nanomaterials that have been shown to be LDI-active,[23,25,37–39] this method provides a highly versatile approach to addressing the long-standing challenge of quantifying nanoparticle internalization, with the potential to increase both throughput and accuracy for fundamental and translational studies of nanomaterials.

5.4 Experimental

5.4.1 Gold Nanoparticle Synthesis

The gold NPs and ligands were synthesized according to the previous reports.[40] The Brust-Schiffrin two-phase synthesis method was used to synthesize 2 nm core AuNPs.[41] After that, the Murray place-exchange was used to functionalize the AuNPs.[42]

5.4.2 Cell Culture and Interaction with Gold Nanoparticles

HeLa and HepG2 cells were cultured in a humidified atmosphere (5% CO_2) at 37 °C and grown in Dulbecco's modified eagle's medium (DMEM, low glucose) supplemented with 10% fetal bovine serum (FBS) and 1% antibiotics (100 U/ml penicillin and 100 μg/ml streptomycin. CHO (ATCC CCL-61), CHO 2 (pgsB-618 (ATCC CRL-2241)) and CHO 3 (pgsA-745 (ATCC CRL-2242)) cells (20,000 cells/well) were cultured in a humidified atmosphere (5% CO_2) at 37 °C and grown in F-12K medium supplemented with 10% fetal bovine serum (FBS), 1% antibiotics (100 U/ml penicillin and 100 μg/ml streptomycin) and 1% non-essential amino acids. The cells were split into two groups, one was plated on ITO glass slide and the other was on 96-well plate. After 24 h of plating, the cells were washed three times with cold phosphate buffer saline (PBS). Then, 125 μl of serum free DMEM containing AuNPs was added to the cells at 37 °C. After incubation, the cells were washed

by cold PBS with one group analyzed directly on ITO glass slide and the other group was lysed for 30 min using lysis buffer (125 µl; Genlantis).

5.4.3 LDI-MS Detection and Quantification of Gold Nanoparticles in Cell Monolayer

ITO glass slides were coated with 0.1% poly-lysine solution for 5 minutes and then washed with deionized water 3 times to remove excess poly-lysine. The coated slides were then air dried. Open-ended Eppendorf (I.D. = 10 mm) tubes were glued to the coated slide on one end to generate media reservoirs for the cell culture. Planted cells on the slides were used for incubation with AuNPs. After incubation, the reservoirs were removed and cell monolayers on the substrate were analyzed by LDI-MS. All LDI-MS measurements were carried on a Bruker Autoflex III MALDI-TOF mass spectrometer. All mass spectra were acquired in the reflectron mode with an average of 100 laser shots at a repetition frequency at 100 Hz. The acceleration voltage was set to 19 kV. Bruker software (FlexAnalysis Version 3.3) was used for data analysis. At least 30 spectra were collected and averaged for each sample point.

5.4.4 LDI-MS Detection and Quantification of Gold Nanoparticles in Cell Lysate

The lysed cells containing AuNP 1 and/or AuNP 2 were centrifuged at 14,000 r.p.m. for 30 min. Cell pellets generated by this process were collected and washed with 60% acetonitrile/40% water to remove excess surfactants. Then, the pellets were transferred onto a 384 MTP grounded stainless steel MALDI target for LDI-MS analysis. External calibration curves were generated before sample analyses (See Figure S6 in Supplementary Information). Increasing concentrations of AuNP 2 (0, 1, 2, 5, 10 and 20 pmol) and a constant amount of AuNP 1 (5 pmol) were spiked into cell lysate and vortexed for 15 min. The resulting pellets from centrifugation were washed and analyzed by LDI-MS. The

intensity ratios of the molecular ions for both AuNPs were plotted against AuNP molar ratios to generate a calibration curve. The quantities of AuNP were then determined by comparing with the calibration curve.

5.4.5 ICP-MS Sample Preparation and Measurements

After incubation of the AuNPs with the cells, the lysed cells were digested with 0.5 ml of fresh aqua regia (highly corrosive; use with high caution) for 15 min. The digested samples were diluted to 10 ml with deionized water. A series of gold standard solutions (0, 0.2, 0.5, 1, 2, 5, 10 and 20 ppb) were prepared in 5 % aqua regia before each experiment. The gold standard solutions and cell lysate samples were measured on a PerkinElmer Nexion ICP mass spectrometer. The instrument was operated with 1,100W radiofrequency power, and the nebulizer argon flow rate was optimized around 0.9 to 1.1 l/ min.

5.4.6 Quantification of Total, Internalized, and Cell Surface-Bound AuNP 2

After incubation and addition of the internal standard (AuNP 1), the cells are lysed for ICP-MS detection. The gold amount measured from the sample is denoted by X (ng). X arises from contributions from the gold amounts of AuNP 2 (X (AuNP 2) total) and AuNP 1 (X (AuNP 1)). The LDI-MS measured molar ratio between AuNP 2 and AuNP 1 is denoted by Y. Y_{total} represents the molar ratio of the total amounts of AuNP 2 to AuNP 1. With equation (1), the absolute amount of total AuNP 2 with cells can be calculated.

$$\begin{cases} X\ (AuNP\ 2)_{total} = X - X\ (AuNP\ 1) \\ \dfrac{X\ (AuNP\ 2)_{total}}{X\ (AuNP\ 1)} = Y_{total} \end{cases} \tag{1}$$

$$X(AuNP\ 2)_{surface} = \frac{Y_{surface}}{Y_{total}} \times X(AuNP\ 2)_{total} \tag{2}$$

$$X(AuNP\ 2)_{internalization} = X(AuNP\ 2)_{total} - X(AuNP\ 2)_{surface} \tag{3}$$

Equation (2) describes the absolute amount of AuNP 2 on the cell surface. $Y_{surface}$ represents the molar ratio of cell surface-bound AuNP 2 to AuNP 1. By subtracting AuNP 2 on cell surface from total amount of AuNP 2 in equation (3), absolute amount for internalization can be determined.

5.5 References

(1)   Duncan, B.; Kim, C.; Rotello, V. M. Gold Nanoparticle Platforms as Drug and Biomacromolecule Delivery Systems. *J. Control. Release* **2010**, *148* (1), 122–127.

(2)   Tao, A. R.; Habas, S.; Yang, P. Shape Control of Colloidal Metal Nanocrystals. *Small* **2008**, *4* (3), 310–325.

(3)   Faraji, A. H.; Wipf, P. Nanoparticles in Cellular Drug Delivery. *Bioorg. Med. Chem.* **2009**, *17* (8), 2950–2962.

(4)   Meyer, D. E.; Shin, B. C.; Kong, G. A.; Dewhirst, M. W.; Chilkoti, A. Drug Targeting Using Thermally Responsive Polymers and Local Hyperthermia. *J. Control. Release* **2001**, *74* (1–3), 213–224.

(5)   Hong, R.; Han, G.; Fernández, J. M.; Kim, B.; Forbes, N. S.; Rotello, V. M. Glutathione-Mediated Delivery and Release Using Monolayer Protected Nanoparticle Carriers. *J. Am. Chem. Soc.* **2006**, *128* (4), 1078–1079.

(6)   Gao, X.; Cui, Y.; Levenson, R. M.; Chung, L. W. K.; Nie, S. In Vivo Cancer Targeting and Imaging with Semiconductor Quantum Dots. *Nat. Biotechnol.* **2004**, *22* (8), 969–976.

(7)   Kircher, M. F.; de la Zerda, A.; Jokerst, J. V.; Zavaleta, C. L.; Kempen, P. J.; Mittra, E.; Pitter, K.; Huang, R.; Campos, C.; Habte, F.; et al. A Brain Tumor Molecular Imaging Strategy Using a New Triple-Modality MRI-Photoacoustic-Raman Nanoparticle. *Nat. Med.* **2012**, *18* (5), 829–834.

(8)   Brannon-Peppas, L.; Blanchette, J. O. Nanoparticle and Targeted Systems for Cancer Therapy. *Adv. Drug Deliv. Rev.* **2012**, *64*, 206–212.

(9)   Verma, A.; Stellacci, F. Effect of Surface Properties on Nanoparticle-Cell Interactions. *Small* **2010**, *6* (1), 12–21.

(10)   Lesniak, A.; Salvati, A.; Santos-Martinez, M. J.; Radomski, M. W.; Dawson, K. A.; Åberg, C. Nanoparticle Adhesion to the Cell Membrane and Its Effect on Nanoparticle Uptake Efficiency. *J. Am. Chem. Soc.* **2013**, *135* (4), 1438–1444.

(11)   Verma, A.; Uzun, O.; Hu, Y.; Hu, Y.; Han, H.-S.; Watson, N.; Chen, S.; Irvine, D. J.; Stellacci, F. Surface-Structure-Regulated Cell-Membrane Penetration by Monolayer-Protected Nanoparticles. *Nat. Mater.* **2008**, *7* (7), 588–595.

(12)   Hartmann, R.; Weidenbach, M.; Neubauer, M.; Fery, A.; Parak, W. J. Stiffness-Dependent In Vitro Uptake and Lysosomal Acidification of Colloidal Particles. *Angew. Chemie Int. Ed.* **2015**, *54* (4), 1365–1368.

(13) Sokolov, K.; Follen, M.; Aaron, J.; Pavlova, I.; Malpica, A.; Lotan, R.; Richards-Kortum, R. Real-Time Vital Optical Imaging of Precancer Using Anti-Epidermal Growth Factor Receptor Antibodies Conjugated to Gold Nanoparticles. *Cancer Res.* **2003**, *63* (9), 1999–2004.

(14) Chithrani, B. D.; Ghazani, A. A.; Chan, W. C. W. Determining the Size and Shape Dependence of Gold Nanoparticle Uptake into Mammalian Cells. *Nano Lett.* **2006**, *6* (4), 662–668.

(15) Semmling, M.; Kreft, O.; Muñoz Javier, A.; Sukhorukov, G. B.; Käs, J.; Parak, W. J. A Novel Flow-Cytometry-Based Assay for Cellular Uptake Studies of Polyelectrolyte Microcapsules. *Small* **2008**, *4* (10), 1763–1768.

(16) Kim, J. A.; Åberg, C.; Salvati, A.; Dawson, K. A. Role of Cell Cycle on the Cellular Uptake and Dilution of Nanoparticles in a Cell Population. *Nat. Nanotechnol.* **2012**, *7* (1), 62–68.

(17) Cho, E. C.; Xie, J.; Wurm, P. A.; Xia, Y. Understanding the Role of Surface Charges in Cellular Adsorption versus Internalization by Selectively Removing Gold Nanoparticles on the Cell Surface with a I 2 /KI Etchant. *Nano Lett.* **2009**, *9* (3), 1080–1084.

(18) Braun, G. B.; Friman, T.; Pang, H.-B.; Pallaoro, A.; de Mendoza, T. H.; Willmore, A.-M. A.; Kotamraju, V. R.; Mann, A. P.; She, Z.-G.; Sugahara, K. N.; et al. Etchable Plasmonic Nanoparticle Probes to Image and Quantify Cellular Internalization. *Nat. Mater.* **2014**, *13* (9), 904–911.

(19) Cooper, R. A. Iodine Revisited. *Int. Wound J.* **2007**, *4* (2), 124–137.

(20) Zhu, Z. J.; Yeh, Y.-C.; Tang, R.; Yan, B.; Tamayo, J.; Vachet, R. W.; Rotello, V. M. Stability of Quantum Dots in Live Cells. *Nat. Chem.* **2011**, *3* (12), 963–968.

(21) Yan, B.; Jeong, Y.; Mercante, L. a; Tonga, G. Y.; Kim, C.; Zhu, Z. J.; Vachet, R. W.; Rotello, V. M. Characterization of Surface Ligands on Functionalized Magnetic Nanoparticles Using Laser Desorption/Ionization Mass Spectrometry (LDI-MS). *Nanoscale* **2013**, *5* (11), 5063–5066.

(22) Chen, S.; Xiong, C.; Liu, H.; Wan, Q.; Hou, J.; He, Q.; Badu-Tawiah, A.; Nie, Z. Mass Spectrometry Imaging Reveals the Sub-Organ Distribution of Carbon Nanomaterials. *Nat. Nanotechnol.* **2015**, *10* (2), 176–182.

(23) Yan, B.; Kim, S. T.; Kim, C. S.; Saha, K.; Moyano, D. F.; Xing, Y.; Jiang, Y.; Roberts, A. L.; Alfonso, F. S.; Rotello, V. M.; et al. Multiplexed Imaging of Nanoparticles in Tissues Using Laser Desorption/Ionization Mass Spectrometry. *J. Am. Chem. Soc.* **2013**, *135* (34), 12564–12567.

(24) Zhu, Z. J.; Ghosh, P. S.; Miranda, O. R.; Vachet, R. W.; Rotello, V. M. Multiplexed Screening of Cellular Uptake of Gold Nanoparticles Using Laser Desorption/Ionization Mass Spectrometry. *J. Am. Chem. Soc.* **2008**, *130* (43), 14139–14143.

(25) Zhu, Z. J.; Tang, R.; Yeh, Y.-C.; Miranda, O. R.; Rotello, V. M.; Vachet, R. W. Determination of the Intracellular Stability of Gold Nanoparticle Monolayers Using Mass Spectrometry. *Anal. Chem.* **2012**, *84* (10), 4321–4326.

(26) Zhu, Z. J.; Rotello, V. M.; Vachet, R. W. Engineered Nanoparticle Surfaces for Improved Mass Spectrometric Analyses. *Analyst* **2009**, *134* (11), 2183–2188.

(27)   Kim, S. T.; Saha, K.; Kim, C.; Rotello, V. M. The Role of Surface Functionality in Determining Nanoparticle Cytotoxicity. *Acc. Chem. Res.* **2013**, *46* (3), 681–691.

(28)   Hoffmann, E. De; Stroobant, V. *Mass Spectrometry Principles and Applications Third Edition*; 2007.

(29)   Titushkin, I.; Cho, M. Regulation of Cell Cytoskeleton and Membrane Mechanics by Electric Field: Role of Linker Proteins. *Biophys. J.* **2009**, *96* (2), 717–728.

(30)   Saha, K.; Kim, S. T.; Yan, B.; Miranda, O. R.; Alfonso, F. S.; Shlosman, D.; Rotello, V. M. Surface Functionality of Nanoparticles Determines Cellular Uptake Mechanisms in Mammalian Cells. *Small* **2013**, *9* (2), 300–305.

(31)   Prats-Mateu, B.; Ertl, P.; Toca-Herrera, J. L. Influence of HepG2 Cell Shape on Nanoparticle Uptake. *Microsc. Res. Tech.* **2014**, *77* (8), 560–565.

(32)   Tang, R.; Moyano, D. F.; Subramani, C.; Yan, B.; Jeoung, E.; Tonga, G. Y.; Duncan, B.; Yeh, Y.-C.; Jiang, Z.; Kim, C.; et al. Rapid Coating of Surfaces with Functionalized Nanoparticles for Regulation of Cell Behavior. *Adv. Mater.* **2014**, *26* (20), 3310–3314.

(33)   Stanley, P.; Caillibot, V.; Siminovitch, L. Selection and Characterization of Eight Phenotypically Distinct Lines of Lectin-Resistant Chinese Hamster Ovary Cells. *Cell* **1975**, *6* (2), 121–128.

(34)   Payne, C. K.; Jones, S. A.; Chen, C.; Zhuang, X. Internalization and Trafficking of Cell Surface Proteoglycans and Proteoglycan-Binding Ligands. *Traffic* **2007**, *8* (4), 389–401.

(35)   Bajaj, A.; Rana, S.; Miranda, O. R.; Yawe, J. C.; Jerry, D. J.; Bunz, U. H. F.; Rotello, V. M. Cell Surface-Based Differentiation of Cell Types and Cancer States Using a Gold Nanoparticle-GFP Based Sensing Array. *Chem. Sci.* **2010**, *1* (1), 134.

(36)   Ernst, B.; Magnani, J. L. From Carbohydrate Leads to Glycomimetic Drugs. *Nat. Rev. Drug Discov.* **2009**, *8* (8), 661–677.

(37)   Castellana, E. T.; Russell, D. H. Tailoring Nanoparticle Surface Chemistry to Enhance Laser Desorption Ionization of Peptides and Proteins. *Nano Lett.* **2007**, *7* (10), 3023–3025.

(38)   Wen, X.; Dagan, S.; Wysocki, V. H. Small-Molecule Analysis with Silicon-Nanoparticle-Assisted Laser Desorption/Ionization Mass Spectrometry. *Anal. Chem.* **2007**, *79* (2), 434–444.

(39)   Chen, C.-T.; Chen, Y.-C. Fe 3 O 4 /TiO 2 Core/Shell Nanoparticles as Affinity Probes for the Analysis of Phosphopeptides Using TiO 2 Surface-Assisted Laser Desorption/Ionization Mass Spectrometry. *Anal. Chem.* **2005**, *77* (18), 5912–5919.

(40)   Brust, M.; Walker, M.; Bethell, D.; Schiffrin, D. J.; Whyman, R. Synthesis of Thiol-Derivatised Gold Nanoparticles in a Two-Phase Liquid–Liquid System. *J. Chem. Soc., Chem. Commun.* **1994**, No. 7, 801–802.

(41)   Templeton, A. C.; Wuelfing, W. P.; Murray, R. W. Monolayer-Protected Cluster Molecules. *Acc. Chem. Res.* **2000**, *33* (1), 27–36.

(42)   You, C.-C.; Miranda, O. R.; Gider, B.; Ghosh, P. S.; Kim, I.-B.; Erdogan, B.; Krovi, S. A.; Bunz, U. H. F.; Rotello, V. M. Detection and Identification of Proteins Using Nanoparticle–Fluorescent Polymer 'Chemical Nose' Sensors. *Nat. Nanotechnol.* **2007**, *2* (5), 318–323.

CHAPTER 6

SUMMARY AND FUTURE WORK

6.1 Dissertation Summary

In this dissertation, mass spectrometry methods were developed to evaluate the uptake, distribution, accumulation, and biochemical effects of AuNPs and AuNP-based nanomaterials. First, we developed a method to evaluate complex nanodelivery vehicles in tissues. LA-ICP-MS and MALDI-MS imaging were used in combination to evaluate sub-organ distributions of an AuNP-based delivery system and its cargo-induced biochemical effects. LA-ICP-MSI was utilized to track the inorganic AuNP carrier while MALDI-MS was utilized to determine the biochemical changes caused by the delivery of an siRNA cargo. Combing the two imaging modalities, biochemical effects were evaluated for colocalization with the delivery vehicle. Images were correlated to one another by aligning the Fe signals in LA-ICP-MS and heme signals in MALDI-MS.

Through this analysis, we found new spatial information regarding the biochemical changes in the lipidome upon TNF-α knockdown. The predicted biochemical responses were found predominantly in the white pulp of the spleen. Conversely, several lipids were found to exhibit unexpected changes in their abundances and these were mostly located in red pulp of the spleen, where concentrations of the NPSCs carrier are highest, suggesting that changes to these lipids are caused by the NPSCs themselves.

In combining LA-ICP-MS and MALDI imaging, the distribution of a multitude of inorganic delivery vehicles and their cargos' downstream effects can be monitored in a spatial context in tissues without labeling or modifying the carriers. Due to the multiplex nature of the method, analyses of nanodelivery vehicles can be made comprehensively and

in situ in various sub-organ regions. This method could be especially powerful for assessing the efficacy and penetration of therapeutics in difficult to target tissues such as tumors. However, this method is still not quantitative and therefore methods such as LC-MS or fluorescence may be necessary as a complementary analysis method to extrapolate quantitative information from these particles, i.e. percent of biochemical changes. Additionally, the resolution is limiting and in order to assess cellular level changes, additional assays may also be necessary.

After successfully developing an imaging method to correlate the distributions of nanodelivery vehicle and biochemical effect, we evaluated the correlation between the two qualitatively and quantitatively. MALDI-MSI analysis revealed the sub-organ distribution of predicted biochemical changes in both the spleen and liver tissues. LA-ICP-MS images were co-registered with the MALDI-MSI images to assess correlation values. Of the predicted biochemical changes that behaved as expected, 75% change where the AuNP carrier is not in both tissue types. NPSCs containing non-functional siRNA were also evaluated in the spleen and liver to confirm that the changes occurring were in-fact related to the TNF-α-targeting siRNA cargo. In both the liver and spleen significantly fewer lipid changes were observed, confirming the efficacy of the TNF-α cargo on the system. Some lipid responses were unexpected in the spleen and liver tissues of NPSC-injected mice. Utilizing our method, we found that two exemplary unexpected lipid changes were more greatly correlated with the gold carrier in both the liver and spleen, suggesting biochemical changes may be occurring due to the presence of the nanocarrier itself.

The unexpected results from the previous chapter indicated the potential of our dual-mode imaging method to further evaluate the specific biochemical implications of

nanodelivery vehicles *in vivo*. To assess this, we evaluated the specific lipid changes that occurred in the presence of fully functioning TNF-α NPSCs, scrambled NPSCs with no active cargo, and Arg AuNPs with no linoleic acid. Based on the degree of changes in the presence of each nanomaterial, we found that TNF-α siRNA is playing the biggest role in altering lipids in the system. However, based on the number of changes that still occur in the presence of scrambled siRNA, the linoleic acid appears to have a slight role in altering lipids known to be correlated to TNF-α knockdown.

The dual-mode imaging method provides comprehensive analysis of the sub-organ distribution, colocalization, and biochemical effects of nanodelivery vehicles *in vivo*. By monitoring different nanomaterial types, potential side effects can be identified in a spatial context, providing potential biochemical basis for the arrival of these unexpected changes. In doing so, we found that many of the predicted effects of the NPSCs penetrate beyond where the carriers distribute, while many of the unpredicted effects occur where the carriers accumulate. This type of assessment of nanodelivery vehicles is not only valuable for designing safer and more efficacious materials, but also implies that simply monitoring nanodelivery vehicle distribution is not a comprehensive enough evaluation of these particles *in vivo*. Again, although our method has promising potential to asses nano-based delivery agents' safety and efficacy, because it is neither quantitative or nor highly sensitive, it is necessary to use this method complementarily with other assays to better understand the biochemical effects. Additionally, this method is not high throughput and therefore can be used readily as a first-pass assessment but should be combined with higher throughput biochemical analysis for assessing therapeutic delivery on a larger, more significant scale.

Finally, we described a method to quantitatively measure NP cellular uptake and surface adhesion using LDI-MS. The universality of this method provides a way to assess cellular level information regarding uptake of any LDI-active AuNP in a variety of cell types. Future studies regarding sub-organ specific cell types (i.e. red pulp macrophages or hepatocytes) with the NPs in functional nanodelivery vehicles could be conducted to further assess the mechanism by which these nanomaterials distribute and accumulate when in circulation. This method provides the means to quantitatively assess the uptake of many different nanoparticles simultaneously in a label-free manner. Without disturbing the biochemistry of the particles or the cells themselves, this method is a trustworthy way to evaluate and distinguish the uptake and adhesion of a multitude of nanoparticles in a variety of cell types. However, this method is only useful for particles that have intrinsically ionizable ligands, or mass barcodes, and therefore is limited by the chemistry of the particles themselves. In order to address this, different sample preparation methods may be explored to encourage particle ionization, such as adding matrix to the samples.

The use of nanomaterials in biomedical applications provides immense potential to improve therapeutic delivery, but also generates a greater need for analytical tools to thoroughly assess the safety and efficacy of these materials *in vivo*. Cellular uptake of nanomaterials has been monitored by microscopy methods,[1–3] flow cytometry,[4,5] chemical etching,[6] and ICP-MS.[7] Microscopy provides high resolution methods to reliably measure the cellular internalization of NPs, but is not quantitative in the case of confocal and transmission electron microscopy. Chemical etching and fluorescence microscopy have the capability of being quantitative, but not without chemical modification. Flow cytometry and ICP-MS are quantitative and applicable for nanomaterials with a variety of core

chemistries, however, these methods do not have the capability of readily distinguishing materials with the same core material and different molecular composition, such as varied ligand structures, simultaneously. With MS methods such as LDI, multiple species of NPs can be monitored without chemical modification due to the intrinsic mass of the nanomaterials. However, quantification and sample preparation are more time-intensive with this analytical method and require additional effort, creating a reduced throughput for the assessment of cellular uptake.

Fluctuations in biological molecules in response to nanomaterials can be investigated using enzyme-linked immunosorbent assay (ELISA)[8] and even predictive computational methods.[9] ELISAs are limited in that they can only monitor a select few biological molecules at a time. Conversely, computational methods conducted *in silico*, are much more comprehensive and can probe hundreds of thousands of molecular species' responses to nanomaterials in a matter of minutes. These techniques utilize molecular modeling to assess potential toxicity and inflammatory responses of nanomaterials when they interact with certain cell types (i.e. immunological, endothelial, etc.) by assessing the quantitative structure-activity relationship of the interaction of particles with these cells and biological molecules. This enables the enormous pool of potential biomolecular responses to be concentrated down into to a select focal group of relevant species, however this method is still just predictive and complementary to the experimental assessment of biochemical responses *in vivo*. LC-MS analyses, i.e. proteomics,[10,11] lipidomics,[12] and metabolomics,[12,13] although not as rapid as computational approaches, can also assess hundreds of biomolecular responses to nanomaterials through quantitative, multiplex detection, but this technique is limited in the spatial context of these changes. Utilizing

MALDI-MS, hundreds of biological species can be monitored in tandem and *in situ*, providing spatial context to many biochemical responses, however this method is not as reliable of a quantitative analytical tool and therefore is limited to qualitative assessment of biological changes.

Site-specific information of nanomaterial distributions is typically obtained through methods such as magnetic resonance imaging (MRI),[14] surface plasmon resonance (SPR),[15,16] Raman spectroscopy,[17] and fluorescence microscopy.[18–20] These methods are sensitive and high throughput, however their uses are limited by the chemical properties of the materials themselves and therefore cannot be universally applied to all nanomaterial types. LA-ICP-MS is a sensitive analytical tool that can be applied to a variety of inorganic-based nanomaterials. Additionally, LA-ICP-MS allows for other biologically-relevant inorganic molecules, such as iron and zinc, to be detected simultaneously to provide additional spatial and biological context to the nanomaterial distributions. As with LDI and MALDI, LA-ICP-MS is also limited by the capability of rapid quantification and therefore cannot be high throughput. These methods do however have the capability of providing valuable first-pass, multiplex and spatial, information regarding nanomaterials in vivo.

Overall, the findings of this dissertation illustrate the capacity of LDI, MALDI, and LA-ICP-MS methods to comprehensively monitor the uptake, fate, and biochemical effect of nano-based delivery vehicles *in vivo*. The next section outlines areas in which these methods can be expanded upon for additional applications.

6.2 Future Directions

In the following sections, proposed experiments utilizing the previously developed mass spectrometric analytical techniques will be described for additional AuNP and AuNP-based nanomaterial analyses.

6.2.1 Tracking Carrier, Cargo, and Biochemical Effects Using Dual-Mode MSI

Tracking and evaluating nanodelivery vehicles is of utmost importance in assessing their efficacy in biomedical applications. Our methods have been successfully utilized to better understand the accumulation of these vehicles, the biochemical effects they have *in vivo*, and how these two aspects are correlated to one another. An additional aspect to understanding these vehicles will be monitoring where the cargo itself is localizing. siRNA is not an ideal candidate for this analysis due to the rapid degradation of the molecules *in vivo*, however our NPSC system has the capability of encapsulating hydrophobic drugs that can then be monitored by MALDI-MSI analysis.

Tamoxifen (Figure 6.1), a known chemotherapeutic,[21] is suitable for advancing our
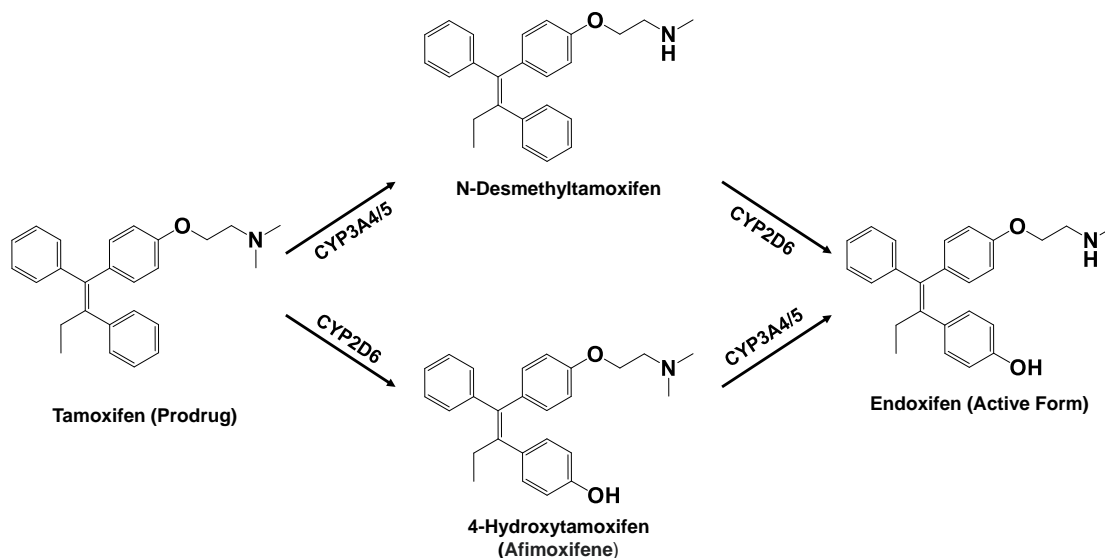
Figure 6.1. Structure and metabolic pathway of tamoxifen to active form, endoxifen. The specific liver P450 enzymes involved in the metabolism pathway are indicated on the arrows.

117

analytical technique towards the simultaneous monitoring of carrier, cargo, and biochemical effect. This molecule has been previously detected in tissues via MALDI-MS analysis[22] and therefore can be easily incorporated into our previously developed dual-mode imaging technique. Tamoxifen is a pro-drug that needs to be metabolized in the liver into its active form endoxifen, which can occur through two different pathways involving liver P450 enzymes (Figure 6.1).[21,23] Tamoxifen's metabolites have been successfully detected by other MS techniques and therefore have the potential to be detected by MALDI methods.[24] Knowing that our NPSC systems accumulate in the liver, we can utilize our dual-mode method to further evaluate how encapsulating this cargo into NPSCs affects the distribution of the drug and potentially its metabolites with respect to the carrier, as well as any biochemical changes that arise.

6.2.2 Mass Spectrometric Analysis of the Circulation and Excretion of Charged AuNPs

Some work has been done by our group to evaluate the role that charge plays on AuNP distribution,[25,26] but little is known about the fate of AuNP of various charges as they
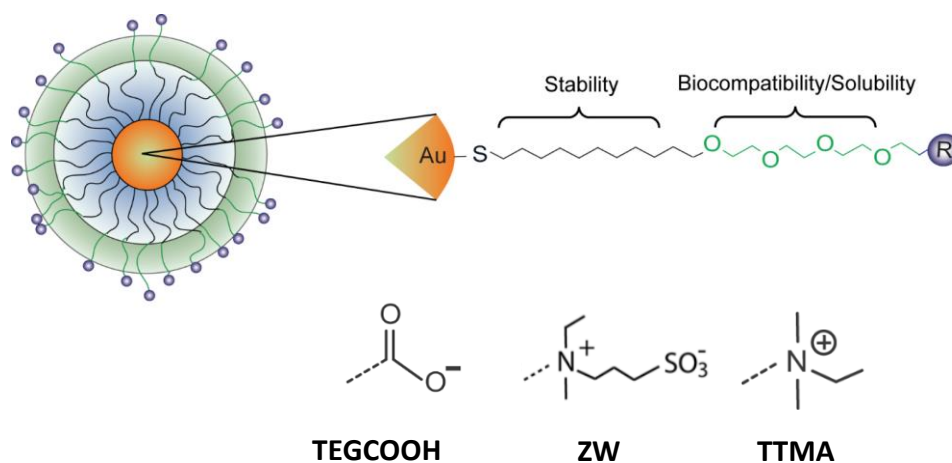
Figure 6.2. Structure of negatively (TEGCOOH), zwitterionic (ZW), and positively (TTMA) charged AuNPs.
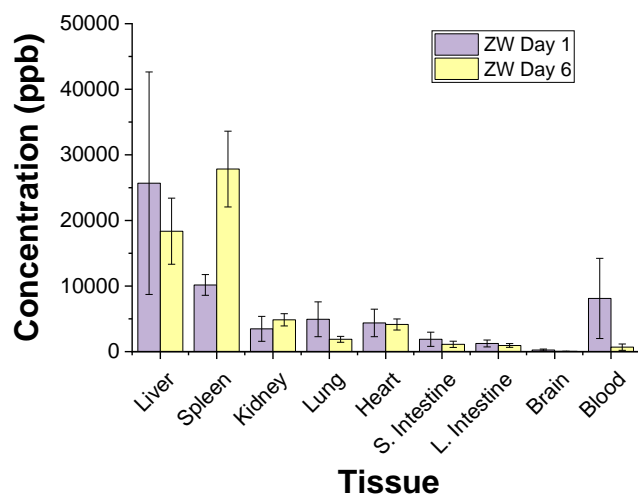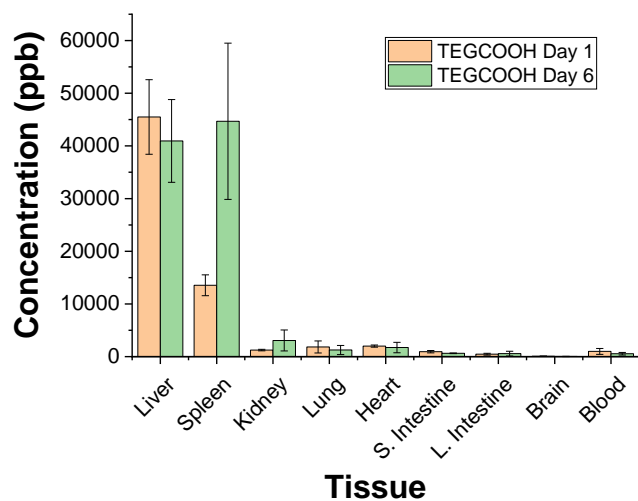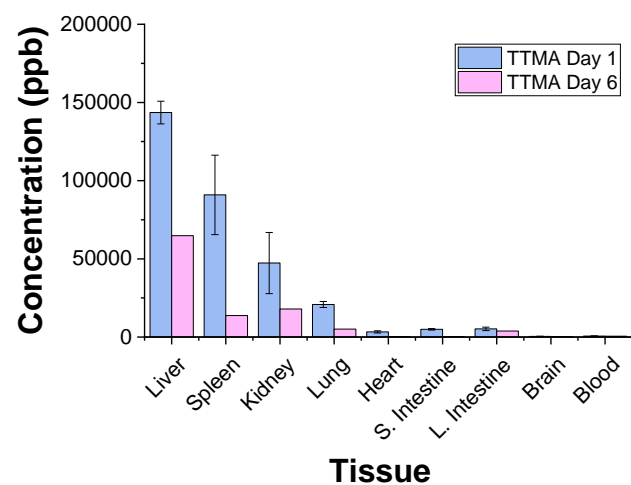
Figure 6.3. Gold accumulation in mouse tissues over time for TTMA, TEGCOOH, and ZW AuNPs. Quantitative measurements made by ICP-MS analysis of digested mouse tissues.

circulate *in vivo*. To evaluate this, AuNPs of 3 surface charges: positive, zwitterionic, negative (Figure 6.2), were injected into mice and they were sacrificed after either one or six days. Tissues were then extracted and digested by ICP-MS analysis to determine the accumulation of AuNPs in the tissues over time. As can be seen in Figure 6.3, AuNPs accumulate differently in mouse tissues over time based on their surface charges. For instance, zwitterionic NPs, which are known to exhibit a "stealth" effect in biological systems,[27] have the greatest shift of accumulation in the blood between day 1 and day 6. This is expected based on the prediction that these nanomaterials circulate longer in the blood than those that are positively or negatively charged.

The results obtained in Figure 6.4, which shows a mass balance of all the tissues that were digested and analyzed by ICP-MS, also indicates that surface charge dictates how quickly gold is excreted from tissues over time. It appears that while ZW and TTMA particles are consistently lost through excretion, TEGCOOH particles exhibit minimal changes over time. To further evaluate this, urine and feces excretions were collected from
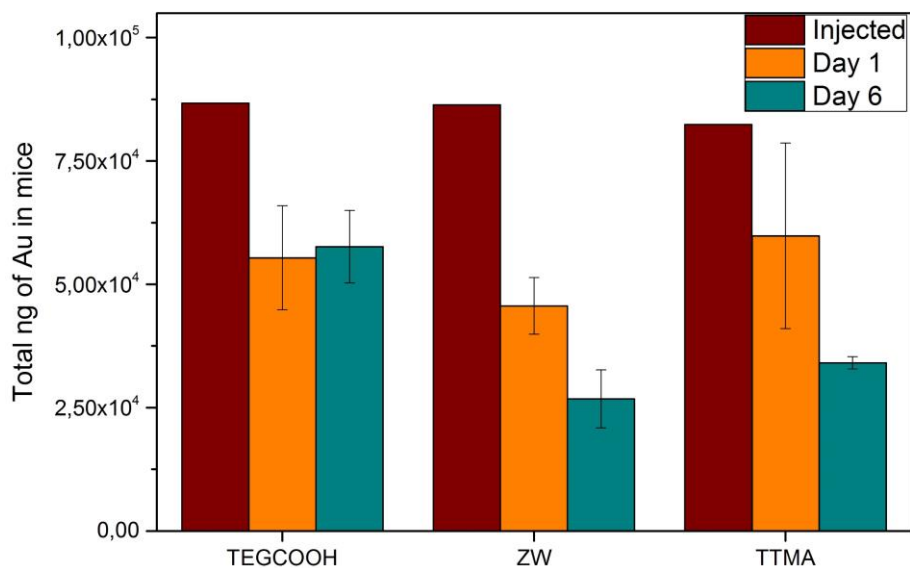
Figure 6.4. Mass balance of gold accumulation in all TEGCOOH, ZW, and TTMA AuNP tissues analyzed by ICP-MS.
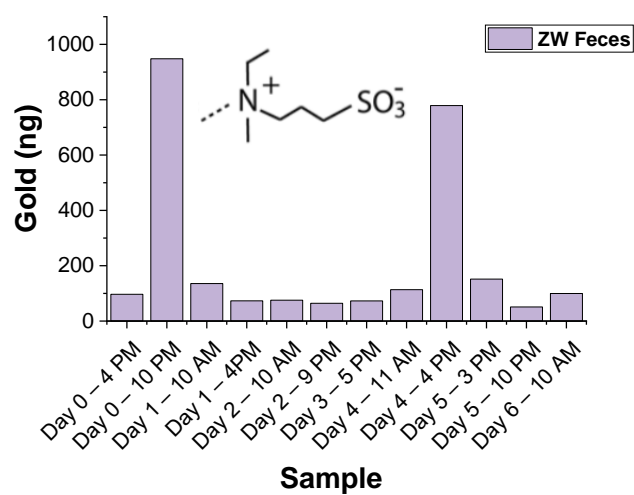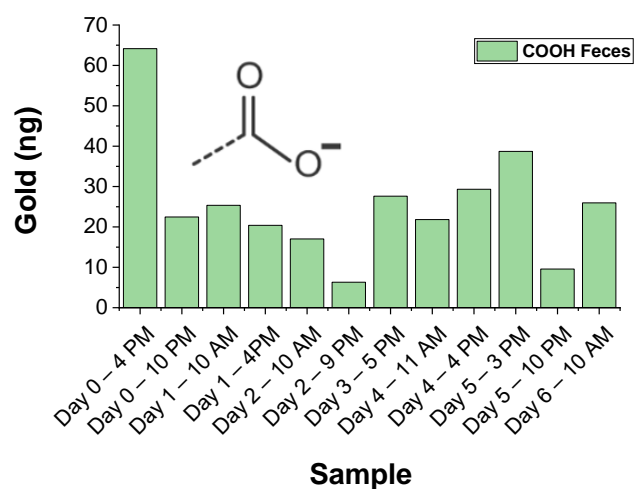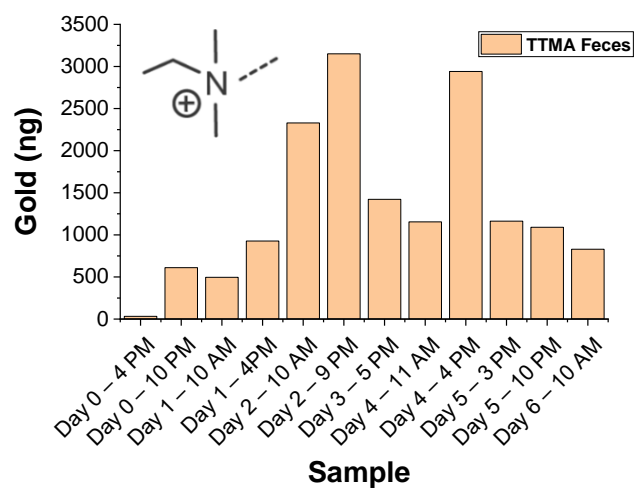
Figure 6.5. ICP-MS analyses of Au in feces for (a) TTMA, (b) TEGCOOH, and (c) ZW AuNPs, over time.
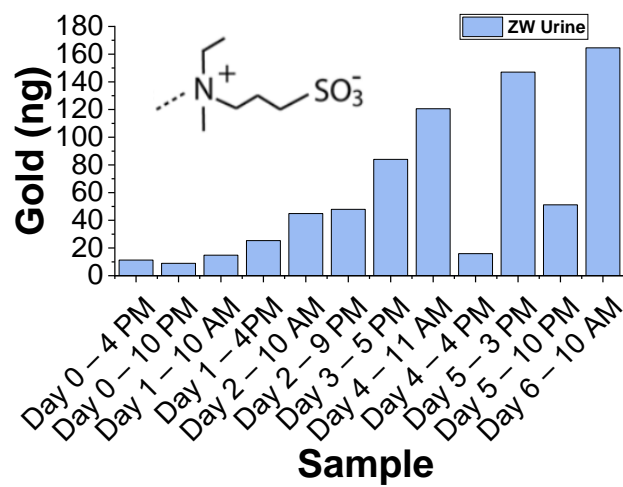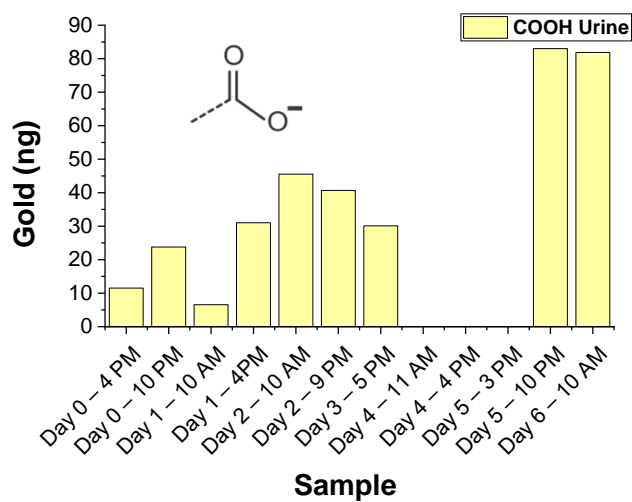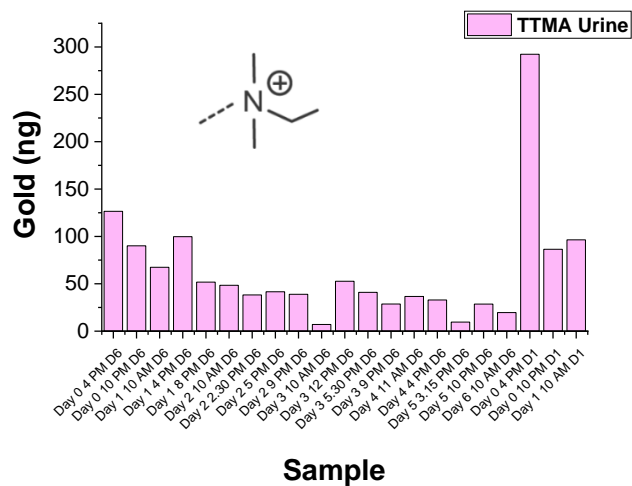
Figure 6.6. ICP-MS analyses of Au in urine for (a) TTMA, (b) TEGCOOH, and (c) ZW AuNPs, over time.

mice over the course of the six days before sacrifice. As can be seen in Figures 6.5 & 6.6, surface charge also dictates to which secretory pathway (urinary or hepatobiliary) AuNPs favor. TTMA AuNPs seem to heavily favor consistent excretion through the hepatobiliary system as seen in Figure 6.5a whereas TEGCOOH particles seem to be minimally excreted through the feces (Figure 6.5b). Zwitterionic particles interestingly, exhibit a spike in gold excretion through the feces between day 1 and day 4. This further confirms the longer circulation of these particles *in vivo*.

Urine analysis (Figure 6.6) provides less conclusive information regarding the excretion of particles through the urinary system and will need to be repeated. However, some preliminary experiments were conducted using previously developed AuNP stability assays,[28,29] and it was found that the ligands of TTMA intact AuNPs can be readily detected by LDI-MS (Figure 6.6). Future work could evaluate whether excreted TTMA AuNPs are in-tact over time in both urine and feces excretions. This could provide insight into if and how nanomaterials are degraded circulating *in vivo*.

Additionally, MSI experiments can be conducted to determine how the AuNPs distribute in the sub-organ regions of tissues over time. Preliminary LA-ICP-MS experiments have been conducted to assess the changes in sub-organ gold distribution in liver, kidney, and spleen tissues. Combining this imaging modality with LDI-MS,[30] the stability of AuNP particles within sub-organ regions of various tissue types over time can be evaluated. Finally, MALDI-MSI methods can be utilized to evaluate how biochemical markers, such as lipids, peptides, and proteins, are changing in response to the circulation over time. In combination, this data will thoroughly examine the effect AuNP surface charge has on circulation, accumulation, stability, and excretion over time.

6.3 References

(1)   Verma, A.; Uzun, O.; Hu, Y.; Hu, Y.; Han, H.-S.; Watson, N.; Chen, S.; Irvine, D. J.; Stellacci, F. Surface-Structure-Regulated Cell-Membrane Penetration by Monolayer-Protected Nanoparticles. *Nat. Mater.* **2008**, *7* (7), 588–595.

(2)   Hartmann, R.; Weidenbach, M.; Neubauer, M.; Fery, A.; Parak, W. J. Stiffness-Dependent In Vitro Uptake and Lysosomal Acidification of Colloidal Particles. *Angew. Chemie Int. Ed.* **2015**, *54* (4), 1365–1368.

(3)   Sokolov, K.; Follen, M.; Aaron, J.; Pavlova, I.; Malpica, A.; Lotan, R.; Richards-Kortum, R. Real-Time Vital Optical Imaging of Precancer Using Anti-Epidermal Growth Factor Receptor Antibodies Conjugated to Gold Nanoparticles. *Cancer Res.* **2003**, *63* (9), 1999–2004.

(4)   Semmling, M.; Kreft, O.; Muñoz Javier, A.; Sukhorukov, G. B.; Käs, J.; Parak, W. J. A Novel Flow-Cytometry-Based Assay for Cellular Uptake Studies of Polyelectrolyte Microcapsules. *Small* **2008**, *4* (10), 1763–1768.

(5)   Kim, J. A.; Åberg, C.; Salvati, A.; Dawson, K. A. Role of Cell Cycle on the Cellular Uptake and Dilution of Nanoparticles in a Cell Population. *Nat. Nanotechnol.* **2012**, *7* (1), 62–68.

(6)   Cooper, R. A. Iodine Revisited. *Int. Wound J.* **2007**, *4* (2), 124–137.

(7)   Chithrani, B. D.; Ghazani, A. A.; Chan, W. C. W. Determining the Size and Shape Dependence of Gold Nanoparticle Uptake into Mammalian Cells. *Nano Lett.* **2006**, *6* (4), 662–668.

(8)   Greulich, C.; Diendorf, J.; Geßmann, J.; Simon, T.; Habijan, T.; Eggeler, G.; Schildhauer, T. A.; Epple, M.; Köller, M. Cell Type-Specific Responses of Peripheral Blood Mononuclear Cells to Silver Nanoparticles. *Acta Biomater.* **2011**, *7* (9), 3505–3514.

(9)   Epa, V. C.; Burden, F. R.; Tassa, C.; Weissleder, R.; Shaw, S.; Winkler, D. A. Modeling Biological Activities of Nanoparticles. *Nano Lett.* **2012**, *12* (11), 5808–5812.

(10)   Lai, Z. W.; Yan, Y.; Caruso, F.; Nice, E. C. Emerging Techniques in Proteomics for Probing Nano–Bio Interactions. *ACS Nano* **2012**, *6* (12), 10438–10448.

(11)   Hofmann, D.; Tenzer, S.; Bannwarth, M. B.; Messerschmidt, C.; Glaser, S.-F.; Schild, H.; Landfester, K.; Mailänder, V. Mass Spectrometry and Imaging Analysis of Nanoparticle-Containing Vesicles Provide a Mechanistic Insight into Cellular Trafficking. *ACS Nano* **2014**, *8* (10), 10077–10088.

(12)	Guo, N. L.; Poh, T. Y.; Pirela, S.; Farcas, M. T.; Chotirmall, S. H.; Tham, W. K.; Adav, S. S.; Ye, Q.; Wei, Y.; Shen, S.; et al. Integrated Transcriptomics, Metabolomics, and Lipidomics Profiling in Rat Lung, Blood, and Serum for Assessment of Laser Printer-Emitted Nanoparticle Inhalation Exposure-Induced Disease Risks. *Int. J. Mol. Sci.* **2019**, *20* (24), 6348.

(13)	Dailey, L. A.; Hernández-Prieto, R.; Casas-Ferreira, A. M.; Jones, M.-C.; Riffo-Vasquez, Y.; Rodríguez-Gonzalo, E.; Spina, D.; Jones, S. A.; Smith, N. W.; Forbes, B.; et al. Adenosine Monophosphate Is Elevated in the Bronchoalveolar Lavage Fluid of Mice with Acute Respiratory Toxicity Induced by Nanoparticles with High Surface Hydrophobicity. *Nanotoxicology* **2015**, *9* (1), 106–115.

(14)	Veiseh, O.; Gunn, J. W.; Zhang, M. Design and Fabrication of Magnetic Nanoparticles for Targeted Drug Delivery and Imaging. *Adv. Drug Deliv. Rev.* **2010**, *62* (3), 284–304.

(15)	Jain, P. K.; Huang, X.; El-Sayed, I. H.; El-Sayed, M. A. Noble Metals on the Nanoscale: Optical and Photothermal Properties and Some Applications in Imaging, Sensing, Biology, and Medicine. *Acc. Chem. Res.* **2008**, *41* (12), 1578–1586.

(16)	Verma, A.; Stellacci, F. Effect of Surface Properties on Nanoparticle-Cell Interactions. *Small* **2010**, *6* (1), 12–21.

(17)	Jensen, T. R.; Malinsky, M. D.; Haynes, C. L.; Van Duyne, R. P. Nanosphere Lithography: Tunable Localized Surface Plasmon Resonance Spectra of Silver Nanoparticles. *J. Phys. Chem. B* **2000**, *104* (45), 10549–10556.

(18)	Gao, X.; Cui, Y.; Levenson, R. M.; Chung, L. W. K.; Nie, S. In Vivo Cancer Targeting and Imaging with Semiconductor Quantum Dots. *Nat. Biotechnol.* **2004**, *22* (8), 969–976.

(19)	Medintz, I. L.; Uyeda, H. T.; Goldman, E. R.; Mattoussi, H. Quantum Dot Bioconjugates for Imaging, Labelling and Sensing. *Nat. Mater.* **2005**, *4* (6), 435–446.

(20)	Cheng, Y.; Meyers, J. D.; Broome, A.-M.; Kenney, M. E.; Basilion, J. P.; Burda, C. Deep Penetration of a PDT Drug into Tumors by Noncovalent Drug-Gold Nanoparticle Conjugates. *J. Am. Chem. Soc.* **2011**, *133* (8), 2583–2591.

(21)	Rivera-Guevara, C.; Camacho, J. Tamoxifen and Its New Derivatives in Cancer Research. *Recent Pat. Anticancer. Drug Discov.* **2011**, *6* (2), 237–245.

(22)	Végvári, Á.; Shavkunov, A. S.; Fehniger, T. E.; Grabau, D.; Niméus, E.; Marko-Varga, G. Localization of Tamoxifen in Human Breast Cancer Tumors by MALDI Mass Spectrometry Imaging. *Clin. Transl. Med.* **2016**, *5* (1), 10.

(23)   Lyon, E.; Gastier Foster, J.; Palomaki, G. E.; Pratt, V. M.; Reynolds, K.; Sábato, M. F.; Scott, S. A.; Vitazka, P. Laboratory Testing of CYP2D6 Alleles in Relation to Tamoxifen Therapy. *Genet. Med.* **2012**, *14* (12), 990–1000.

(24)   Squirewell, E. J.; Qin, X.; Duffel, M. W. Endoxifen and Other Metabolites of Tamoxifen Inhibit Human Hydroxysteroid Sulfotransferase 2A1 (HSULT2A1). *Drug Metab. Dispos.* **2014**, *42* (11), 1843–1850.

(25)   Zhu, Z. J.; Wang, H.; Yan, B.; Zheng, H.; Jiang, Y.; Miranda, O. R.; Rotello, V. M.; Xing, B.; Vachet, R. W. Effect of Surface Charge on the Uptake and Distribution of Gold Nanoparticles in Four Plant Species. *Environ. Sci. Technol.* **2012**, *46* (22), 12391–12398.

(26)   Elci, S. G.; Jiang, Y.; Yan, B.; Kim, S. T.; Saha, K.; Moyano, D. F.; Yesilbag Tonga, G.; Jackson, L. C.; Rotello, V. M.; Vachet, R. W. Surface Charge Controls the Suborgan Biodistributions of Gold Nanoparticles. *ACS Nano* **2016**, *10* (5), 5536–5542.

(27)   Butcher, N. J.; Mortimer, G. M.; Minchin, R. F. Unravelling the Stealth Effect. *Nat. Nanotechnol.* **2016**, *11* (4), 310–311.

(28)   Zhu, Z. J.; Tang, R.; Yeh, Y.-C.; Miranda, O. R.; Rotello, V. M.; Vachet, R. W. Determination of the Intracellular Stability of Gold Nanoparticle Monolayers Using Mass Spectrometry. *Anal. Chem.* **2012**, *84* (10), 4321–4326.

(29)   Zhu, Z. J.; Yeh, Y.-C.; Tang, R.; Yan, B.; Tamayo, J.; Vachet, R. W.; Rotello, V. M. Stability of Quantum Dots in Live Cells. *Nat. Chem.* **2011**, *3* (12), 963–968.

(30)   Elci, S. G.; Yesilbag Tonga, G.; Yan, B.; Kim, S. T.; Kim, C. S.; Jiang, Y.; Saha, K.; Moyano, D. F.; Marsico, A. L. M.; Rotello, V. M.; et al. Dual-Mode Mass Spectrometric Imaging for Determination of in Vivo Stability of Nanoparticle Monolayers. *ACS Nano* **2017**, *11* (7), 7424–7430.

BIBLIOGRAPHY

Abrams, M. T.; Koser, M. L.; Seitzer, J.; Williams, S. C.; DiPietro, M. A.; Wang, W.; Shaw, A. W.; Mao, X.; Jadhav, V.; Davide, J. P.; et al. Evaluation of Efficacy, Biodistribution, and Inflammation for a Potent SiRNA Nanoparticle: Effect of Dexamethasone Co-Treatment. *Mol. Ther.* **2010**, *18* (1), 171–180.

Albanese, A.; Tang, P. S.; Chan, W. C. W. The Effect of Nanoparticle Size, Shape, and Surface Chemistry on Biological Systems. *Annu. Rev. Biomed. Eng.* **2012**, *14* (1), 1–16.

Alkilany, A. M.; Lohse, S. E.; Murphy, C. J. The Gold Standard: Gold Nanoparticle Libraries To Understand the Nano–Bio Interface. *Acc. Chem. Res.* **2013**, *46* (3), 650–661.

Angel, L. A.; Majors, L. T.; Dharmaratne, A. C.; Dass, A. Ion Mobility Mass Spectrometry of Au 25 (SCH 2 CH 2 Ph) 18 Nanoclusters. *ACS Nano* **2010**, *4* (8), 4691–4700.

Arvizo, R. R.; Miranda, O. R.; Moyano, D. F.; Walden, C. A.; Giri, K.; Bhattacharya, R.; Robertson, J. D.; Rotello, V. M.; Reid, J. M.; Mukherjee, P. Modulating Pharmacokinetics, Tumor Uptake and Biodistribution by Engineered Nanoparticles. *PLoS One* **2011**, *6* (9), 3–8.

Attia, A. S.; Schroeder, K. A.; Seeley, E. H.; Wilson, K. J.; Hammer, N. D.; Colvin, D. C.; Manier, M. L.; Nicklay, J. J.; Rose, K. L.; Gore, J. C.; et al. Monitoring the Inflammatory Response to Infection through the Integration of MALDI IMS and MRI. *Cell Host Microbe* **2012**, *11* (6), 664–673.

Babu, A.; Templeton, A. K.; Munshi, A.; Ramesh, R. Nanodrug Delivery Systems: A Promising Technology for Detection, Diagnosis, and Treatment of Cancer. *AAPS PharmSciTech* **2014**, *15* (3), 709–721.

Bajaj, A.; Rana, S.; Miranda, O. R.; Yawe, J. C.; Jerry, D. J.; Bunz, U. H. F.; Rotello, V. M. Cell Surface-Based Differentiation of Cell Types and Cancer States Using a Gold Nanoparticle-GFP Based Sensing Array. *Chem. Sci.* **2010**, *1* (1), 134.

Bermúdez-López, M.; Arroyo, D.; Betriu, À.; Masana, L.; Fernández, E.; Valdivielso, J. M. New Perspectives on CKD-Induced Dyslipidemia. *Expert Opin. Ther. Targets* **2017**, *21* (10), 967–976.

Berry, K. A. Z.; Li, B.; Reynolds, S. D.; Barkley, R. M.; Gijón, M. A.; Hankin, J. A.; Henson, P. M.; Murphy, R. C. MALDI Imaging MS of Phospholipids in the Mouse Lung. *J. Lipid Res.* **2011**, *52* (8), 1551–1560.

Böhme, S.; Stärk, H.-J.; Kühnel, D.; Reemtsma, T. Exploring LA-ICP-MS as a Quantitative Imaging Technique to Study Nanoparticle Uptake in Daphnia Magna and Zebrafish (Danio Rerio) Embryos. *Anal. Bioanal. Chem.* **2015**, *407* (18), 5477–5485.

Boisselier, E.; Astruc, D. Gold Nanoparticles in Nanomedicine: Preparations, Imaging, Diagnostics, Therapies and Toxicity. *Chem. Soc. Rev.* **2009**, *38* (6), 1759.

Borges Da Silva, H.; Fonseca, R.; Pereira, R. M.; Cassado, A. A.; Álvarez, J. M.; D'Império Lima, M. R. Splenic Macrophage Subsets and Their Function during Blood-Borne Infections. *Front. Immunol.* **2015**, *6*, 480.

Brannon-Peppas, L.; Blanchette, J. O. Nanoparticle and Targeted Systems for Cancer Therapy. *Adv. Drug Deliv. Rev.* **2012**, *64*, 206–212.

Braun, G. B.; Friman, T.; Pang, H.-B.; Pallaoro, A.; de Mendoza, T. H.; Willmore, A.-M. A.; Kotamraju, V. R.; Mann, A. P.; She, Z.-G.; Sugahara, K. N.; et al. Etchable Plasmonic Nanoparticle Probes to Image and Quantify Cellular Internalization. *Nat. Mater.* **2014**, *13* (9), 904–911.

Brust, M.; Walker, M.; Bethell, D.; Schiffrin, D. J.; Whyman, R. Synthesis of Thiol-Derivatised Gold Nanoparticles in a Two-Phase Liquid–Liquid System. *J. Chem. Soc., Chem. Commun.* **1994**, No. 7, 801–802.

Buchberger, A. R.; DeLaney, K.; Johnson, J.; Li, L. Mass Spectrometry Imaging: A Review of Emerging Advancements and Future Insights. *Anal. Chem.* **2018**, *90* (1), 240-265.

Butcher, N. J.; Mortimer, G. M.; Minchin, R. F. Unravelling the Stealth Effect. *Nat. Nanotechnol.* **2016**, *11* (4), 310–311.

Castellana, E. T.; Russell, D. H. Tailoring Nanoparticle Surface Chemistry to Enhance Laser Desorption Ionization of Peptides and Proteins. *Nano Lett.* **2007**, *7* (10), 3023–3025.

Castellanos-García, L. J.; Gokhan Elci, S.; Vachet, R. W. Reconstruction, Analysis, and Segmentation of LA-ICP-MS Imaging Data Using Python for the Identification of Sub-Organ Regions in Tissues. *Analyst* **2020,** *145* (10), 3705-3712.

Cawthorn, W. P.; Sethi, J. K. TNF-α and Adipocyte Biology. *FEBS Lett.* **2008**, *582* (1), 117–131.

Cecile Martel; Davide Degli Esposti; Antonin Bouchet; Catherine Brenner; Antoinette Lemoine. Non-Alcoholic Steatohepatitis: New Insights from OMICS Studies. *Curr. Pharm. Biotechnol.* **2012**, *13* (5), 726-735.

Cesta, M. F. Normal Structure, Function, and Histology of the Spleen. *Toxicol. Pathol.* **2006**, *34* (5), 455-465.

Chan, W. C. W. Quantum Dot Bioconjugates for Ultrasensitive Nonisotopic Detection. *Science (80-.).* **1998**, *281* (5385), 2016–2018.

Chen, C.-T.; Chen, Y.-C. Fe 3 O 4 /TiO 2 Core/Shell Nanoparticles as Affinity Probes for the Analysis of Phosphopeptides Using TiO 2 Surface-Assisted Laser Desorption/Ionization Mass Spectrometry. *Anal. Chem.* **2005**, *77* (18), 5912–5919.

Chen, S.; Xiong, C.; Liu, H.; Wan, Q.; Hou, J.; He, Q.; Badu-Tawiah, A.; Nie, Z. Mass Spectrometry Imaging Reveals the Sub-Organ Distribution of Carbon Nanomaterials. *Nat. Nanotechnol.* **2015**, *10* (2), 176–182.

Cheng, Y.; Meyers, J. D.; Broome, A.-M.; Kenney, M. E.; Basilion, J. P.; Burda, C. Deep Penetration of a PDT Drug into Tumors by Noncovalent Drug-Gold Nanoparticle Conjugates. *J. Am. Chem. Soc.* **2011**, *133* (8), 2583–2591.

Chithrani, B. D.; Ghazani, A. A.; Chan, W. C. W. Determining the Size and Shape Dependence of Gold Nanoparticle Uptake into Mammalian Cells. *Nano Lett.* **2006**, *6* (4), 662–668.

Cho, E. C.; Xie, J.; Wurm, P. A.; Xia, Y. Understanding the Role of Surface Charges in Cellular Adsorption versus Internalization by Selectively Removing Gold Nanoparticles on the Cell Surface with a I 2 /KI Etchant. *Nano Lett.* **2009**, *9* (3), 1080–1084.

Cillero-Pastor, B.; Heeren, R. M. A. Matrix-Assisted Laser Desorption Ionization Mass Spectrometry Imaging for Peptide and Protein Analyses: A Critical Review of On-Tissue Digestion. *J. Proteome Res.* **2014**, *13* (2), 325–335.

Cooper, R. A. Iodine Revisited. *Int. Wound J.* **2007**, *4* (2), 124–137.

Creran, B.; Yan, B.; Moyano, D. F.; Gilbert, M. M.; Vachet, R. W.; Rotello, V. M. Laser Desorption Ionization Mass Spectrometric Imaging of Mass Barcoded Gold Nanoparticles for Security Applications. *Chem. Commun.* **2012**, *48* (38), 4543.

Dailey, L. A.; Hernández-Prieto, R.; Casas-Ferreira, A. M.; Jones, M.-C.; Riffo-Vasquez, Y.; Rodríguez-Gonzalo, E.; Spina, D.; Jones, S. A.; Smith, N. W.; Forbes, B.; et al. Adenosine Monophosphate Is Elevated in the Bronchoalveolar Lavage Fluid of Mice with Acute Respiratory Toxicity Induced by Nanoparticles with High Surface Hydrophobicity. *Nanotoxicology* **2015**, *9* (1), 106–115.

Daniel, M.-C.; Astruc, D. Gold Nanoparticles: Assembly, Supramolecular Chemistry, Quantum-Size-Related Properties, and Applications toward Biology, Catalysis, and Nanotechnology. *Chem. Rev.* **2004**, *104* (1), 293–346.

Dass, A.; Dubay, G. R.; Fields-Zinna, C. A.; Murray, R. W. FAB Mass Spectrometry of Au 25 (SR) 18 Nanoparticles. *Anal. Chem.* **2008**, *80* (18), 6845–6849.

Dass, A.; Holt, K.; Parker, J. F.; Feldberg, S. W.; Murray, R. W. Mass Spectrometrically Detected Statistical Aspects of Ligand Populations in Mixed Monolayer Au 25 L 18 Nanoparticles. *J. Phys. Chem. C* **2008**, *112* (51), 20276–20283.

Dass, A.; Stevenson, A.; Dubay, G. R.; Tracy, J. B.; Murray, R. W. Nanoparticle MALDI-TOF Mass Spectrometry without Fragmentation: Au 25 (SCH 2 CH 2 Ph) 18 and Mixed Monolayer Au 25 (SCH 2 CH 2 Ph) 18− x (L) X. *J. Am. Chem. Soc.* **2008**, *130* (18), 5940–5946.

De Jong, W. H.; Hagens, W. I.; Krystek, P.; Burger, M. C.; Sips, A. J. A. M.; Geertsma, R. E. Particle Size-Dependent Organ Distribution of Gold Nanoparticles after Intravenous Administration. *Biomaterials* **2008**, *29* (12), 1912–1919.

de Vega, R. G.; Sanchez, M. L. F.; Eiro, N.; Vizoso, F. J.; Sperling, M.; Karst, U.; Medel, A. S. Multimodal Laser Ablation/Desorption Imaging Analysis of Zn and MMP-11 in Breast Tissues. *Anal. Bioanal. Chem.* **2018**, *410* (3), 913–922.

de Visser, H. M.; Mastbergen, S. C.; Ravipati, S.; Welsing, P. M. J.; Pinto, F. C.; Lafeber, F. P. J. G.; Chapman, V.; Barrett, D. A.; Weinans, H. Local and Systemic Inflammatory Lipid Profiling in a Rat Model of Osteoarthritis with Metabolic Dysregulation. *PLoS One* **2018**, *13* (4), e0196308.

De, M.; Ghosh, P. S.; Rotello, V. M. Applications of Nanoparticles in Biology. *Adv. Mater.* **2008**, *20* (22), 4225–4241.

Dreaden, E. C.; Alkilany, A. M.; Huang, X.; Murphy, C. J.; El-Sayed, M. a. The Golden Age: Gold Nanoparticles for Biomedicine. *Chem. Soc. Rev.* **2012**, *41* (7), 2740.

Drescher, D.; Giesen, C.; Traub, H.; Panne, U.; Kneipp, J.; Jakubowski, N. Quantitative Imaging of Gold and Silver Nanoparticles in Single Eukaryotic Cells by Laser Ablation ICP-MS. *Anal. Chem.* **2012**, *84* (22), 9684–9688.

Drescher, D.; Zeise, I.; Traub, H.; Guttmann, P.; Seifert, S.; Büchner, T.; Jakubowski, N.; Schneider, G.; Kneipp, J. In Situ Characterization of SiO 2 Nanoparticle Biointeractions Using BrightSilica. *Adv. Funct. Mater.* **2014**, *24* (24), 3765–3775.

Duncan, B.; Kim, C.; Rotello, V. M. Gold Nanoparticle Platforms as Drug and Biomacromolecule Delivery Systems. *J. Control. Release* **2010**, *148* (1), 122–127.

Elci, S. G.; Jiang, Y.; Yan, B.; Kim, S. T.; Saha, K.; Moyano, D. F.; Yesilbag Tonga, G.; Jackson, L. C.; Rotello, V. M.; Vachet, R. W. Surface Charge Controls the Suborgan Biodistributions of Gold Nanoparticles. *ACS Nano* **2016**, *10* (5), 5536–5542.

Elci, S. G.; Yan, B.; Kim, S. T.; Saha, K.; Jiang, Y.; Klemmer, G. A.; Moyano, D. F.; Tonga, G. Y.; Rotello, V. M.; Vachet, R. W. Quantitative Imaging of 2 Nm Monolayer-Protected Gold Nanoparticle Distributions in Tissues Using Laser Ablation Inductively-Coupled Plasma Mass Spectrometry (LA-ICP-MS). *Analyst* **2016**, *141* (8), 2418–2425.

Elci, S. G.; Yesilbag Tonga, G.; Yan, B.; Kim, S. T.; Kim, C. S.; Jiang, Y.; Saha, K.; Moyano, D. F.; Marsico, A. L. M.; Rotello, V. M.; et al. Dual-Mode Mass Spectrometric Imaging for Determination of in Vivo Stability of Nanoparticle Monolayers. *ACS Nano* **2017**, *11* (7), 7424–7430.

Epa, V. C.; Burden, F. R.; Tassa, C.; Weissleder, R.; Shaw, S.; Winkler, D. A. Modeling Biological Activities of Nanoparticles. *Nano Lett.* **2012**, *12* (11), 5808–5812.

Ernst, B.; Magnani, J. L. From Carbohydrate Leads to Glycomimetic Drugs. *Nat. Rev. Drug Discov.* **2009**, *8* (8), 661–677.

Esquenazi, E.; Yang, Y. L.; Watrous, J.; Gerwick, W. H.; Dorrestein, P. C. Imaging Mass Spectrometry of Natural Products. *Nat. Prod. Rep.* **2009**, *26* (12), 1521–1534.

Exner (Little Bear), F. Advances in Knowledge Discovery and Data Mining. *J. Am. Soc. Inf. Sci.* **1998**, *49* (4), 386–387.

Faraji, A. H.; Wipf, P. Nanoparticles in Cellular Drug Delivery. *Bioorg. Med. Chem.* **2009**, *17* (8), 2950–2962.

Flinders, B.; Huizing, L. R. S.; Van Heerden, M.; Cuyckens, F.; Neumann, U. P.; Van Der Laan, L. J. W.; Olde Damink, S. W. M.; Heeren, R. M. A.; Schaap, F. G.; Vreeken, R. J. Cross-Species Molecular Imaging of Bile Salts and Lipids in Liver: Identification of Molecular Structural Markers in Health and Disease. *Anal. Chem.* **2018**, *90* (20) 11835-11846.

Fülöp, A.; Sammour, D. A.; Erich, K.; von Gerichten, J.; van Hoogevest, P.; Sandhoff, R.; Hopf, C. Molecular Imaging of Brain Localization of Liposomes in Mice Using MALDI Mass Spectrometry. *Sci. Rep.* **2016**, *6* (1), 33791.

Gao, X.; Cui, Y.; Levenson, R. M.; Chung, L. W. K.; Nie, S. In Vivo Cancer Targeting and Imaging with Semiconductor Quantum Dots. *Nat. Biotechnol.* **2004**, *22* (8), 969–976.

García, K. P.; Zarschler, K.; Barbaro, L.; Barreto, J. A.; O'Malley, W.; Spiccia, L.; Stephan, H.; Graham, B. Zwitterionic-Coated "Stealth" Nanoparticles for Biomedical Applications: Recent Advances in Countering Biomolecular Corona Formation and Uptake by the Mononuclear Phagocyte System. *Small* **2014**, *10* (13), 2516–2529.

Gelaye, B.; Sumner, S. J.; McRitchie, S.; Carlson, J. E.; Ananth, C. V.; Enquobahrie, D. A.; Qiu, C.; Sorensen, T. K.; Williams, M. A. Maternal Early Pregnancy Serum Metabolomics Profile and Abnormal Vaginal Bleeding as Predictors of Placental Abruption: A Prospective Study. *PLoS One* **2016**, *11* (6), e0156755.

Gemoll, T.; Miroll, E.; Klein, O.; Lischka, A.; Eravci, M.; Thorns, C.; Habermann, J. K. Spatial UBE2N Protein Expression Indicates Genomic Instability in Colorectal Cancers. *BMC Cancer* **2019**, *19* (1), 710.

Glish, G. L.; Vachet, R. W. The Basics of Mass Spectrometry in the Twenty-First Century. *Nat. Rev. Drug Discov.* **2003**, *2* (2), 140–150.

Gordon, J. R.; Galli, S. J. Mast Cells as a Source of Both Preformed and Immunologically Inducible TNF-α/Cachectin. *Nature* **1990**, *346* (6281) 274-276.

Goto-Inoue, N.; Hayasaka, T.; Zaima, N.; Setou, M. Imaging Mass Spectrometry for Lipidomics. *Biochim. Biophys. Acta - Mol. Cell Biol. Lipids* **2011**, *1811* (11), 961–969.

Greulich, C.; Diendorf, J.; Geßmann, J.; Simon, T.; Habijan, T.; Eggeler, G.; Schildhauer, T. A.; Epple, M.; Köller, M. Cell Type-Specific Responses of Peripheral Blood Mononuclear Cells to Silver Nanoparticles. *Acta Biomater.* **2011**, *7* (9), 3505–3514.

Gunawan, C.; Lim, M.; Marquis, C. P.; Amal, R. Nanoparticle-Protein Corona Complexes Govern the Biological Fates and Functions of Nanoparticles. *J. Mater. Chem. B* **2014**, *2* (15), 2060–2083.

Guo, N. L.; Poh, T. Y.; Pirela, S.; Farcas, M. T.; Chotirmall, S. H.; Tham, W. K.; Adav, S. S.; Ye, Q.; Wei, Y.; Shen, S.; et al. Integrated Transcriptomics, Metabolomics, and Lipidomics Profiling in Rat Lung, Blood, and Serum for Assessment of Laser Printer-Emitted Nanoparticle Inhalation Exposure-Induced Disease Risks. *Int. J. Mol. Sci.* **2019**, *20* (24), 6348.

Gustafson, H. H.; Holt-Casper, D.; Grainger, D. W.; Ghandehari, H. Nanoparticle Uptake: The Phagocyte Problem. *Nano Today* **2015**, *10* (4), 487–510.

Haiss, W.; Thanh, N. T. K.; Aveyard, J.; Fernig, D. G. Determination of Size and Concentration of Gold Nanoparticles from UV−Vis Spectra. *Anal. Chem.* **2007**, *79* (11), 4215–4221.

Hardie, J.; Jiang, Y.; Tetrault, E. R.; Ghazi, P. C.; Tonga, G. Y.; Farkas, M. E.; Rotello, V. M. Simultaneous Cytosolic Delivery of a Chemotherapeutic and SiRNA Using Nanoparticle-Stabilized Nanocapsules. *Nanotechnology* **2016**, *27* (37), 374001.

Harkewicz, R.; Dennis, E. A. Applications of Mass Spectrometry to Lipids and Membranes. *Annu. Rev. Biochem.* **2011**, *80* (1), 301–325.

Harkness, K. M.; Balinski, A.; McLean, J. A.; Cliffel, D. E. Nanoscale Phase Segregation of Mixed Thiolates on Gold Nanoparticles. *Angew. Chemie Int. Ed.* **2011**, *50* (45), 10554–10559.

Harkness, K. M.; Cliffel, D. E.; McLean, J. A. Characterization of Thiolate-Protected Gold Nanoparticles by Mass Spectrometry. *Analyst* **2010**, *135* (5), 868.

Hartmann, R.; Weidenbach, M.; Neubauer, M.; Fery, A.; Parak, W. J. Stiffness-Dependent In Vitro Uptake and Lysosomal Acidification of Colloidal Particles. *Angew. Chemie Int. Ed.* **2015**, *54* (4), 1365–1368.

Heaven, M. W.; Dass, A.; White, P. S.; Holt, K. M.; Murray, R. W. Crystal Structure of the Gold Nanoparticle [N(C 8 H 17) 4][Au 25 (SCH 2 CH 2 Ph) 18]. *J. Am. Chem. Soc.* **2008**, *130* (12), 3754–3755.

Hoffmann, E. De; Stroobant, V. *Mass Spectrometry Principles and Applications Third Edition*; 2007.

Hofmann, D.; Messerschmidt, C.; Bannwarth, M. B.; Landfester, K.; Mailänder, V. Drug Delivery without Nanoparticle Uptake: Delivery by a Kiss-and-Run Mechanism on the Cell Membrane. *Chem. Commun.* **2014**, *50* (11), 1369–1371.

Hofmann, D.; Tenzer, S.; Bannwarth, M. B.; Messerschmidt, C.; Glaser, S.-F.; Schild, H.; Landfester, K.; Mailänder, V. Mass Spectrometry and Imaging Analysis of Nanoparticle-Containing Vesicles Provide a Mechanistic Insight into Cellular Trafficking. *ACS Nano* **2014**, *8* (10), 10077–10088.

Holzlechner, M.; Bonta, M.; Lohninger, H.; Limbeck, A.; Marchetti-Deschmann, M. Multisensor Imaging—From Sample Preparation to Integrated Multimodal Interpretation of LA-ICPMS and MALDI MS Imaging Data. *Anal. Chem.* **2018**, *90* (15), 8831–8837.

Hong, R.; Han, G.; Fernández, J. M.; Kim, B.; Forbes, N. S.; Rotello, V. M. Glutathione-Mediated Delivery and Release Using Monolayer Protected Nanoparticle Carriers. *J. Am. Chem. Soc.* **2006**, *128* (4), 1078–1079.

Hostetler, M. J.; Templeton, A. C.; Murray, R. W. Dynamics of Place-Exchange Reactions on Monolayer-Protected Gold Cluster Molecules. *Langmuir* **1999**, *15* (11), 3782–3789.

Hostetler, M. J.; Wingate, J. E.; Zhong, C.-J.; Harris, J. E.; Vachet, R. W.; Clark, M. R.; Londono, J. D.; Green, S. J.; Stokes, J. J.; Wignall, G. D.; et al. Alkanethiolate Gold Cluster Molecules with Core Diameters from 1.5 to 5.2 Nm: Core and Monolayer Properties as a Function of Core Size. *Langmuir* **1998**, *14* (1), 17–30.

Hou, S.; Sikora, K. N.; Tang, R.; Liu, Y.; Lee, Y.-W.; Kim, S. T.; Jiang, Z.; Vachet, R. W.; Rotello, V. M. Quantitative Differentiation of Cell Surface-Bound and Internalized Cationic Gold Nanoparticles Using Mass Spectrometry. *ACS Nano* **2016**, *10* (7), 6731–6736.

Ifuku, M.; Katafuchi, T.; Mawatari, S.; Noda, M.; Miake, K.; Sugiyama, M.; Fujino, T. Anti-Inflammatory/Anti-Amyloidogenic Effects of Plasmalogens in Lipopolysaccharide-Induced Neuroinflammation in Adult Mice. *J. Neuroinflammation* **2012**, *9* (1), 673.

Irie, A.; Yamamoto, K.; Miki, Y.; Murakami, M. Phosphatidylethanolamine Dynamics Are Required for Osteoclast Fusion. *Sci. Rep.* **2017**, *7* (1), 46715.

Jackson, A. M.; Hu, Y.; Silva, P. J.; Stellacci, F. From Homoligand- to Mixed-Ligand-Monolayer-Protected Metal Nanoparticles: A Scanning Tunneling Microscopy Investigation. *J. Am. Chem. Soc.* **2006**, *128* (34), 11135–11149.

Jadzinsky, P. D.; Calero, G.; Ackerson, C. J.; Bushnell, D. A.; Kornberg, R. D. Structure of a Thiol Monolayer-Protected Gold Nanoparticle at 1.1 A Resolution. *Science (80-.).* **2007**, *318* (5849), 430–433.

Jain, P. K.; Huang, X.; El-Sayed, I. H.; El-Sayed, M. A. Noble Metals on the Nanoscale: Optical and Photothermal Properties and Some Applications in Imaging, Sensing, Biology, and Medicine. *Acc. Chem. Res.* **2008**, *41* (12), 1578–1586.

Jensen, T. R.; Malinsky, M. D.; Haynes, C. L.; Van Duyne, R. P. Nanosphere Lithography: Tunable Localized Surface Plasmon Resonance Spectra of Silver Nanoparticles. *J. Phys. Chem. B* **2000**, *104* (45), 10549–10556.

Jiang, Y.; Hardie, J.; Liu, Y.; Ray, M.; Luo, X.; Das, R.; Landis, R. F.; Farkas, M. E.; Rotello, V. M. Nanocapsule-Mediated Cytosolic SiRNA Delivery for Anti-Inflammatory Treatment. *J. Control. Release* **2018**, *283* (May), 235–240.

Jiang, Y.; Tang, R.; Duncan, B.; Jiang, Z.; Yan, B.; Mout, R.; Rotello, V. M. Direct Cytosolic Delivery of SiRNA Using Nanoparticle-Stabilized Nanocapsules. *Angew. Chemie - Int. Ed.* **2015**, *54* (2), 506–510.

Jones, M. A.; Cho, S. H.; Patterson, N. H.; Van de Plas, R.; Spraggins, J. M.; Boothby, M. R.; Caprioli, R. M. Discovering New Lipidomic Features Using Cell Type Specific Fluorophore Expression to Provide Spatial and Biological Specificity in a Multimodal Workflow with MALDI Imaging Mass Spectrometry. *Anal. Chem.* **2020**, *92* (10), 7079-7086.

Kang, S.; Mauter, M. S.; Elimelech, M. Microbial Cytotoxicity of Carbon-Based Nanomaterials: Implications for River Water and Wastewater Effluent. *Environ. Sci. Technol.* **2009**, *43* (7), 2648–2653.

Khovidhunkit, W.; Kim, M.-S.; Memon, R. A.; Shigenaga, J. K.; Moser, A. H.; Feingold, K. R.; Grunfeld, C. Thematic Review Series: The Pathogenesis of Atherosclerosis. Effects of Infection and Inflammation on Lipid and Lipoprotein Metabolism Mechanisms and Consequences to the Host. *J. Lipid Res.* **2004**, *45* (7), 1169–1196.

Kievit, F. M.; Zhang, M. Surface Engineering of Iron Oxide Nanoparticles for Targeted Cancer Therapy. *Acc. Chem. Res.* **2011**, *44* (10), 853–862.

Kihara, M.; Matsuo-Tezuka, Y.; Noguchi-Sasaki, M.; Yorozu, K.; Kurasawa, M.; Shimonaka, Y.; Hirata, M. Visualization of 57 Fe-Labeled Heme Isotopic Fine Structure and Localization of Regions of Erythroblast Maturation in Mouse Spleen by MALDI FTICR-MS Imaging. *J. Am. Soc. Mass Spectr.* **2017**, *28* (11), 2469-2475.

Kim, J. A.; Åberg, C.; Salvati, A.; Dawson, K. A. Role of Cell Cycle on the Cellular Uptake and Dilution of Nanoparticles in a Cell Population. *Nat. Nanotechnol.* **2012**, *7* (1), 62–68.

Kim, S. T.; Saha, K.; Kim, C.; Rotello, V. M. The Role of Surface Functionality in Determining Nanoparticle Cytotoxicity. *Acc. Chem. Res.* **2013**, *46* (3), 681–691.

Kircher, M. F.; de la Zerda, A.; Jokerst, J. V.; Zavaleta, C. L.; Kempen, P. J.; Mittra, E.; Pitter, K.; Huang, R.; Campos, C.; Habte, F.; et al. A Brain Tumor Molecular Imaging Strategy Using a New Triple-Modality MRI-Photoacoustic-Raman Nanoparticle. *Nat. Med.* **2012**, *18* (5), 829–834.

Klein, O.; Strohschein, K.; Nebrich, G.; Fuchs, M.; Thiele, H.; Giavalisco, P.; Duda, G. N.; Winkler, T.; Kobarg, J. H.; Trede, D.; et al. Unraveling Local Tissue Changes within Severely Injured Skeletal Muscles in Response to MSC-Based Intervention Using MALDI Imaging Mass Spectrometry. *Sci. Rep.* **2018**, *8* (1), 12677.

Knochenmuss, R.; Zenobi, R. MALDI Ionization: The Role of In-Plume Processes. *Chem. Rev.* **2003**, *103* (2), 441–452.

Kpegba, K.; Spadaro, T.; Cody, R. B.; Nesnas, N.; Olson, J. A. Analysis of Self-Assembled Monolayers on Gold Surfaces Using Direct Analysis in Real Time Mass Spectrometry. *Anal. Chem.* **2007**, *79* (14), 5479–5483.

Kumar, B.; Jalodia, K.; Kumar, P.; Gautam, H. K. Recent Advances in Nanoparticle-Mediated Drug Delivery. *J. Drug Deliv. Sci. Technol.* **2017**, *41* (6), 260–268.

Lai, Z. W.; Yan, Y.; Caruso, F.; Nice, E. C. Emerging Techniques in Proteomics for Probing Nano–Bio Interactions. *ACS Nano* **2012**, *6* (12), 10438–10448.

Law, S.-H.; Chan, M.-L.; Marathe, G. K.; Parveen, F.; Chen, C.-H.; Ke, L.-Y. An Updated Review of Lysophosphatidylcholine Metabolism in Human Diseases. *Int. J. Mol. Sci.* **2019**, *20* (5), 1149.

Lesniak, A.; Salvati, A.; Santos-Martinez, M. J.; Radomski, M. W.; Dawson, K. A.; Åberg, C. Nanoparticle Adhesion to the Cell Membrane and Its Effect on Nanoparticle Uptake Efficiency. *J. Am. Chem. Soc.* **2013**, *135* (4), 1438–1444.

Lewis, J. K.; Wei, J.; Siuzdak, G. Matrix-Assisted Laser Desorption/Ionization Mass Spectrometry in Peptide and Protein Analysis. *Encyclopedia of Analytical Chemistry* **2006**, 5880–5894.

Li, M.; Luo, Z.; Yan, Y.; Wang, Z.; Chi, Q.; Yan, C.; Xing, B. Arsenate Accumulation, Distribution, and Toxicity Associated with Titanium Dioxide Nanoparticles in Daphnia Magna. *Environ. Sci. Technol.* **2016**, *50* (17), 9636–9643.

Li, Z.; Barnes, J. C.; Bosoy, A.; Stoddart, J. F.; Zink, J. I. Mesoporous Silica Nanoparticles in Biomedical Applications. *Chem. Soc. Rev.* **2012**, *41* (7), 2590.

Li, Z.; Tan, S.; Li, S.; Shen, Q.; Wang, K. Cancer Drug Delivery in the Nano Era: An Overview and Perspectives. *Oncol. Rep.* **2017**, *38* (2), 611–624.

Lin, S.; Reppert, J.; Hu, Q.; Hudson, J. S.; Reid, M. L.; Ratnikova, T. A.; Rao, A. M.; Luo, H.; Ke, P. C. Uptake, Translocation, and Transmission of Carbon Nanomaterials in Rice Plants. *Small* **2009**, *5* (10), 1128–1132.

Liu, J.; Stace-Naughton, A.; Jiang, X.; Brinker, C. J. Porous Nanoparticle Supported Lipid Bilayers (Protocells) as Delivery Vehicles. *J. Am. Chem. Soc.* **2009**, *131* (4), 1354–1355.

Liu, W.; Howarth, M.; Greytak, A. B.; Zheng, Y.; Nocera, D. G.; Ting, A. Y.; Bawendi, M. G. Compact Biocompatible Quantum Dots Functionalized for Cellular Imaging. *J. Am. Chem. Soc.* **2008**, *130* (4), 1274–1284.

Love, J. C.; Estroff, L. A.; Kriebel, J. K.; Nuzzo, R. G.; Whitesides, G. M. Self-Assembled Monolayers of Thiolates on Metals as a Form of Nanotechnology. *Chem. Rev.* **2005**, *105* (4), 1103–1170.

Lukowski, J. K.; Weaver, E. M.; Hummon, A. B. Analyzing Liposomal Drug Delivery Systems in Three-Dimensional Cell Culture Models Using MALDI Imaging Mass Spectrometry. *Anal. Chem.* **2017**, *89* (16), 8453–8458.

Lyon, E.; Gastier Foster, J.; Palomaki, G. E.; Pratt, V. M.; Reynolds, K.; Sábato, M. F.; Scott, S. A.; Vitazka, P. Laboratory Testing of CYP2D6 Alleles in Relation to Tamoxifen Therapy. *Genet. Med.* **2012**, *14* (12), 990–1000.

Mahmoud, N. N.; Alkilany, A. M.; Dietrich, D.; Karst, U.; Al-Bakri, A. G.; Khalil, E. A. Preferential Accumulation of Gold Nanorods into Human Skin Hair Follicles: Effect of Nanoparticle Surface Chemistry. *J. Colloid Interface Sci.* **2017**, *503*, 95–102.

Mahmoudi, M.; Hosseinkhani, H.; Hosseinkhani, M.; Boutry, S.; Simchi, A.; Journeay, W. S.; Subramani, K.; Laurent, S. Magnetic Resonance Imaging Tracking of Stem Cells in Vivo Using Iron Oxide Nanoparticles as a Tool for the Advancement of Clinical Regenerative Medicine. *Chem. Rev.* **2011**, *111* (2), 253–280.

Manova, R. K.; Joshi, S.; Debrassi, A.; Bhairamadgi, N. S.; Roeven, E.; Gagnon, J.; Tahir, M. N.; Claassen, F. W.; Scheres, L. M. W.; Wennekes, T.; et al. Ambient Surface Analysis of Organic Monolayers Using Direct Analysis in Real Time Orbitrap Mass Spectrometry. *Anal. Chem.* **2014**, *86* (5), 2403–2411.

Marsico, A. L. M.; Elci, G. S.; Moyano, D. F.; Yesilbag Tonga, G.; Duncan, B.; Landis, R. F.; Rotello, V. M.; Vachet, R. W. Enhanced Laser Desorption/Ionization Mass Spectrometric Detection of Gold Nanoparticles in Biological Samples Using the Synergy between Added Matrix and the Gold Core. *Anal. Chem.* **2015**, *87* (24), 12145–12150.

Mattoussi, H.; Rotello, V. M. Inorganic Nanoparticles in Drug Delivery. *Adv. Drug Deliv. Rev.* **2013**, *65* (5), 605–606.

Medintz, I. L.; Uyeda, H. T.; Goldman, E. R.; Mattoussi, H. Quantum Dot Bioconjugates for Imaging, Labelling and Sensing. *Nat. Mater.* **2005**, *4* (6), 435–446.

Meyer, D. E.; Shin, B. C.; Kong, G. A.; Dewhirst, M. W.; Chilkoti, A. Drug Targeting Using Thermally Responsive Polymers and Local Hyperthermia. *J. Control. Release* **2001**, *74* (1–3), 213–224.

Miranda, O. R.; Chen, H.-T.; You, C.-C.; Mortenson, D. E.; Yang, X.-C.; Bunz, U. H. F.; Rotello, V. M. Enzyme-Amplified Array Sensing of Proteins in Solution and in Biofluids. *J. Am. Chem. Soc.* **2010**, *132* (14), 5285–5289.

Nagahori, N.; Nishimura, S.-I. Direct and Efficient Monitoring of Glycosyltransferase Reactions on Gold Colloidal Nanoparticles by Using Mass Spectrometry. *Chem. - A Eur. J.* **2006**, *12* (25), 6478–6485.

Nie, S. Probing Single Molecules and Single Nanoparticles by Surface-Enhanced Raman Scattering. *Science (80-.).* **1997**, *275* (5303), 1102–1106.

Niehoff, A.-C.; Kettling, H.; Pirkl, A.; Chiang, Y. N.; Dreisewerd, K.; Yew, J. Y. Analysis of Drosophila Lipids by Matrix-Assisted Laser Desorption/Ionization Mass Spectrometric Imaging. *Anal. Chem.* **2014**, *86* (22), 11086–11092.

Niehoff, A.-C.; Schulz, J.; Soltwisch, J.; Meyer, S.; Kettling, H.; Sperling, M.; Jeibmann, A.; Dreisewerd, K.; Francesconi, K. A.; Schwerdtle, T.; et al. Imaging by Elemental and Molecular Mass Spectrometry Reveals the Uptake of an Arsenolipid in the Brain of Drosophila Melanogaster. *Anal. Chem.* **2016**, *88* (10), 5258–5263.

Osae, E. A.; Steven, P.; Redfern, R.; Hanlon, S.; Smith, C. W.; Rumbaut, R. E.; Burns, A. R. Dyslipidemia and Meibomian Gland Dysfunction: Utility of Lipidomics and Experimental Prospects with a Diet-Induced Obesity Mouse Model. *Int. J. Mol. Sci.* **2019**, *20* (14), 3505.

Pacardo, D. B.; Ligler, F. S.; Gu, Z. Programmable Nanomedicine: Synergistic and Sequential Drug Delivery Systems. *Nanoscale* **2015**, *7* (8), 3381–3391.

Patterson, N. H.; Tuck, M.; Van De Plas, R.; Caprioli, R. M. Advanced Registration and Analysis of MALDI Imaging Mass Spectrometry Measurements through Autofluorescence Microscopy. *Anal. Chem.* **2018**, *90* (21), 12395-12403.

Payne, C. K.; Jones, S. A.; Chen, C.; Zhuang, X. Internalization and Trafficking of Cell Surface Proteoglycans and Proteoglycan-Binding Ligands. *Traffic* **2007**, *8* (4), 389–401.

Peer, D.; Karp, J. M.; Hong, S.; Farokhzad, O. C.; Margalit, R.; Langer, R. Nanocarriers as an Emerging Platform for Cancer Therapy. *Nat. Nanotechnol.* **2007**, *2* (12), 751–760.

Prats-Mateu, B.; Ertl, P.; Toca-Herrera, J. L. Influence of HepG2 Cell Shape on Nanoparticle Uptake. *Microsc. Res. Tech.* **2014**, *77* (8), 560–565.

Raederstorff, D.; Pantze, M.; Bachmann, H.; Moser, U. Anti-Inflammatory Properties of Docosahexaenoic and Eicosapentaenoic Acids in Phorbol-Ester-Lnduced Mouse Ear Inflammation. *Int. Arch. Allergy Immunol.* **1996**, *111* (3), 284–290.

Rivera-Guevara, C.; Camacho, J. Tamoxifen and Its New Derivatives in Cancer Research. *Recent Pat. Anticancer. Drug Discov.* **2011**, *6* (2), 237–245.

Rodenak-Kladniew, B.; Islan, G. A.; de Bravo, M. G.; Durán, N.; Castro, G. R. Design, Characterization and in Vitro Evaluation of Linalool-Loaded Solid Lipid Nanoparticles as Potent Tool in Cancer Therapy. *Colloids Surfaces B Biointerfaces* **2017**, *154*, 123–132.

Saha, K.; Kim, S. T.; Yan, B.; Miranda, O. R.; Alfonso, F. S.; Shlosman, D.; Rotello, V. M. Surface Functionality of Nanoparticles Determines Cellular Uptake Mechanisms in Mammalian Cells. *Small* **2013**, *9* (2), 300–305.

Sapsford, K. E.; Algar, W. R.; Berti, L.; Gemmill, K. B.; Casey, B. J.; Oh, E.; Stewart, M. H.; Medintz, I. L. Functionalizing Nanoparticles with Biological Molecules: Developing Chemistries That Facilitate Nanotechnology. *Chem. Rev.* **2013**, *113* (3), 1904–2074.

Schaaff, T. G. Laser Desorption and Matrix-Assisted Laser Desorption/Ionization Mass Spectrometry of 29-KDa Au:SR Cluster Compounds. *Anal. Chem.* **2004**, *76* (21), 6187–6196.

Semmling, M.; Kreft, O.; Muñoz Javier, A.; Sukhorukov, G. B.; Käs, J.; Parak, W. J. A Novel Flow-Cytometry-Based Assay for Cellular Uptake Studies of Polyelectrolyte Microcapsules. *Small* **2008**, *4* (10), 1763–1768.

Sikora, K. N.; Hardie, J. M.; Castellanos-García, L. J.; Liu, Y.; Reinhardt, B. M.; Farkas, M. E.; Rotello, V. M.; Vachet, R. W. Dual Mass Spectrometric Tissue Imaging of Nanocarrier Distributions and Their Biochemical Effects. *Anal. Chem.* **2020**, *92* (2), 2011–2018.

Singh, R.; Lillard, J. W. Nanoparticle-Based Targeted Drug Delivery. *Exp. Mol. Pathol.* **2009**, *86* (3), 215–223.

Smith, A. M.; Duan, H.; Mohs, A. M.; Nie, S. Bioconjugated Quantum Dots for in Vivo Molecular and Cellular Imaging. *Adv. Drug Deliv. Rev.* **2008**, *60* (11), 1226–1240.

Sokolov, K.; Follen, M.; Aaron, J.; Pavlova, I.; Malpica, A.; Lotan, R.; Richards-Kortum, R. Real-Time Vital Optical Imaging of Precancer Using Anti-Epidermal Growth Factor Receptor Antibodies Conjugated to Gold Nanoparticles. *Cancer Res.* **2003**, *63* (9), 1999–2004.

Squirewell, E. J.; Qin, X.; Duffel, M. W. Endoxifen and Other Metabolites of Tamoxifen Inhibit Human Hydroxysteroid Sulfotransferase 2A1 (HSULT2A1). *Drug Metab. Dispos.* **2014**, *42* (11), 1843–1850.

Stanford, T. E.; Bagley, C. J.; Solomon, P. J. Informed Baseline Subtraction of Proteomic Mass Spectrometry Data Aided by a Novel Sliding Window Algorithm. *Proteome Sci.* **2016**, *14* (1), 19.

Stanley, P.; Caillibot, V.; Siminovitch, L. Selection and Characterization of Eight Phenotypically Distinct Lines of Lectin-Resistant Chinese Hamster Ovary Cells. *Cell* **1975**, *6* (2), 121–128.

Stoeckli, M.; Staab, D.; Schweitzer, A. Compound and Metabolite Distribution Measured by MALDI Mass Spectrometric Imaging in Whole-Body Tissue Sections. *Int. J. Mass Spectrom.* **2007**, *260* (2–3), 195–202.

Sun, S. Monodisperse FePt Nanoparticles and Ferromagnetic FePt Nanocrystal Superlattices. *Science (80-.).* **2000**, *287* (5460), 1989–1992.

Sun, Y.; Yin, M.; Zhang, L.; Pan, J. Characterization of the Cytokine Expression Profiles of the Aorta and Liver of Young Tumor Necrosis Factor Alpha Mutant Mice. *Mol. Cell. Biochem.* **2012**, *366* (1–2), 59–67.

Sussulini, A.; Becker, J. S.; Becker, J. S. Laser Ablation ICP-MS: Application in Biomedical Research. *Mass Spectrom. Rev*. **2017**, *36* (1), 47-57.

Susumu, K.; Uyeda, H. T.; Medintz, I. L.; Pons, T.; Delehanty, J. B.; Mattoussi, H. Enhancing the Stability and Biological Functionalities of Quantum Dots via Compact Multifunctional Ligands. *J. Am. Chem. Soc.* **2007**, *129* (45), 13987–13996.

Svatoš, A. Mass Spectrometric Imaging of Small Molecules. *Trends Biotechnol.* **2010**, *28* (8), 425–434.

Tang, R.; Kim, C. S.; Solfiell, D. J.; Rana, S.; Mout, R.; Velázquez-Delgado, E. M.; Chompoosor, A.; Jeong, Y.; Yan, B.; Zhu, Z.-J.; et al. Direct Delivery of Functional Proteins and Enzymes to the Cytosol Using Nanoparticle-Stabilized Nanocapsules. *ACS Nano* **2013**, *7* (8), 6667–6673.

Tang, R.; Moyano, D. F.; Subramani, C.; Yan, B.; Jeoung, E.; Tonga, G. Y.; Duncan, B.; Yeh, Y.-C.; Jiang, Z.; Kim, C.; et al. Rapid Coating of Surfaces with Functionalized Nanoparticles for Regulation of Cell Behavior. *Adv. Mater.* **2014**, *26* (20), 3310–3314.

Tao, A. R.; Habas, S.; Yang, P. Shape Control of Colloidal Metal Nanocrystals. *Small* **2008**, *4* (3), 310–325.

Templeton, A. C.; Wuelfing, W. P.; Murray, R. W. Monolayer-Protected Cluster Molecules. *Acc. Chem. Res.* **2000**, *33* (1), 27–36.

Titushkin, I.; Cho, M. Regulation of Cell Cytoskeleton and Membrane Mechanics by Electric Field: Role of Linker Proteins. *Biophys. J.* **2009**, *96* (2), 717–728.

Tracy, J. B.; Crowe, M. C.; Parker, J. F.; Hampe, O.; Fields-Zinna, C. A.; Dass, A.; Murray, R. W. Electrospray Ionization Mass Spectrometry of Uniform and Mixed Monolayer Nanoparticles: Au 25 [S(CH 2) 2 Ph] 18 and Au 25 [S(CH 2) 2 Ph] 18 - x (SR) X. *J. Am. Chem. Soc.* **2007**, *129* (51), 16209–16215.

Tracy, J. B.; Kalyuzhny, G.; Crowe, M. C.; Balasubramanian, R.; Choi, J.-P.; Murray, R. W. Poly(Ethylene Glycol) Ligands for High-Resolution Nanoparticle Mass Spectrometry. *J. Am. Chem. Soc.* **2007**, *129* (21), 6706–6707.

Végvári, Á.; Shavkunov, A. S.; Fehniger, T. E.; Grabau, D.; Niméus, E.; Marko-Varga, G. Localization of Tamoxifen in Human Breast Cancer Tumors by MALDI Mass Spectrometry Imaging. *Clin. Transl. Med.* **2016**, *5* (1), 10.

Veiseh, O.; Gunn, J. W.; Zhang, M. Design and Fabrication of Magnetic Nanoparticles for Targeted Drug Delivery and Imaging. *Adv. Drug Deliv. Rev.* **2010**, *62* (3), 284–304.

Verma, A.; Stellacci, F. Effect of Surface Properties on Nanoparticle-Cell Interactions. *Small* **2010**, *6* (1), 12–21.

Verma, A.; Uzun, O.; Hu, Y.; Hu, Y.; Han, H.-S.; Watson, N.; Chen, S.; Irvine, D. J.; Stellacci, F. Surface-Structure-Regulated Cell-Membrane Penetration by Monolayer-Protected Nanoparticles. *Nat. Mater.* **2008**, *7* (7), 588–595.

Wallace, M.; Morris, C.; O'Grada, C. M.; Ryan, M.; Dillon, E. T.; Coleman, E.; Gibney, E. R.; Gibney, M. J.; Roche, H. M.; Brennan, L. Relationship between the Lipidome, Inflammatory Markers and Insulin Resistance. *Mol. BioSyst.* **2014**, *10* (6), 1586–1595.

Weiskirchen, R.; Meurer, S. K.; Liedtke, C.; Huber, M. Mast Cells in Liver Fibrogenesis. *Cells* **2019**, *8* (11), 1429.

Wen, X.; Dagan, S.; Wysocki, V. H. Small-Molecule Analysis with Silicon-Nanoparticle-Assisted Laser Desorption/Ionization Mass Spectrometry. *Anal. Chem.* **2007**, *79* (2), 434–444.

Whetten, R. L.; Khoury, J. T.; Alvarez, M. M.; Murthy, S.; Vezmar, I.; Wang, Z. L.; Stephens, P. W.; Cleveland, C. L.; Luedtke, W. D.; Landman, U. Nanocrystal Gold Molecules. *Adv. Mater.* **1996**, *8* (5), 428–433.

Whitehead, K. A.; Langer, R.; Anderson, D. G. Knocking down Barriers: Advances in SiRNA Delivery. *Nat. Rev. Drug Discov.* **2009**, *8* (2), 129–138.

Whitesides, G. M.; Laibinis, P. E. Wet Chemical Approaches to the Characterization of Organic Surfaces: Self-Assembled Monolayers, Wetting, and the Physical-Organic Chemistry of the Solid-Liquid Interface. *Langmuir* **1990**, *6* (1), 87–96.

Wilhelm, S.; Tavares, A. J.; Dai, Q.; Ohta, S.; Audet, J.; Dvorak, H. F.; Chan, W. C. W. Analysis of Nanoparticle Delivery to Tumours. *Nat. Rev. Mater.* **2016**, *1* (5), 16014.

Wu, B.; Becker, J. S. Imaging of Elements and Molecules in Biological Tissues and Cells in the Low-Micrometer and Nanometer Range. *Int. J. Mass Spectrom.* **2011**, *307* (1–3), 112–122.

Yan, B.; Jeong, Y.; Mercante, L. A.; Tonga, G. Y.; Kim, C.; Zhu, Z. J.; Vachet, R. W.; Rotello, V. M. Characterization of Surface Ligands on Functionalized Magnetic Nanoparticles Using Laser Desorption/Ionization Mass Spectrometry (LDI-MS). *Nanoscale* **2013**.

Yan, B.; Jeong, Y.; Mercante, L. a; Tonga, G. Y.; Kim, C.; Zhu, Z.-J.; Vachet, R. W.; Rotello, V. M. Characterization of Surface Ligands on Functionalized Magnetic Nanoparticles Using Laser Desorption/Ionization Mass Spectrometry (LDI-MS). *Nanoscale* **2013**, *5* (11), 5063–5066.

Yan, B.; Kim, S. T.; Kim, C. S.; Saha, K.; Moyano, D. F.; Xing, Y.; Jiang, Y.; Roberts, A. L.; Alfonso, F. S.; Rotello, V. M.; et al. Multiplexed Imaging of Nanoparticles in Tissues Using Laser Desorption/Ionization Mass Spectrometry. *J. Am. Chem. Soc.* **2013**, *135* (34), 12564–12567.

Yan, B.; Zhu, Z.-J.; Miranda, O. R.; Chompoosor, A.; Rotello, V. M.; Vachet, R. W. Laser Desorption/Ionization Mass Spectrometry Analysis of Monolayer-Protected Gold Nanoparticles. *Anal. Bioanal. Chem.* **2010**, *396* (3), 1025–1035.

Yang, X. C.; Samanta, B.; Agasti, S. S.; Jeong, Y.; Zhu, Z. J.; Rana, S.; Miranda, O. R.; Rotello, V. M. Drug Delivery Using Nanoparticle-Stabilized Nanocapsules. *Angew. Chem. Int. Ed.* **2011**, *50* (2), 477–481.

Yih, T. C.; Al-Fandi, M. Engineered Nanoparticles as Precise Drug Delivery Systems. *J. Cell. Biochem.* **2006**, 97(6), 1184-1190.

You, C. C.; Chompoosor, A.; Rotello, V. M. The Biomacromolecule-Nanoparticle Interface. *Nano Today* **2007**, *2* (3), 34–43.

You, C. C.; Miranda, O. R.; Gider, B.; Ghosh, P. S.; Kim, I.-B.; Erdogan, B.; Krovi, S. A.; Bunz, U. H. F.; Rotello, V. M. Detection and Identification of Proteins Using Nanoparticle–Fluorescent Polymer 'Chemical Nose' Sensors. *Nat. Nanotechnol.* **2007**, *2* (5), 318–323.

Yu, X.; Trase, I.; Ren, M.; Duval, K.; Guo, X.; Chen, Z. Design of Nanoparticle-Based Carriers for Targeted Drug Delivery. *J. Nanomater.* **2016**, 1087250.

Zemski Berry, K. A.; Hankin, J. A.; Barkley, R. M.; Spraggins, J. M.; Caprioli, R. M.; Murphy, R. C. MALDI Imaging of Lipid Biochemistry in Tissues by Mass Spectrometry. *Chem. Rev.* **2011**, *111* (10), 6491–6512.

Zhang, J.; Yuan, Z.-F.; Wang, Y.; Chen, W.-H.; Luo, G.-F.; Cheng, S.-X.; Zhuo, R.-X.; Zhang, X.-Z. Multifunctional Envelope-Type Mesoporous Silica Nanoparticles for Tumor-Triggered Targeting Drug Delivery. *J. Am. Chem. Soc.* **2013**, *135* (13), 5068–5073.

Zhang, Y.; Cai, K.; Li, C.; Guo, Q.; Chen, Q.; He, X.; Liu, L.; Zhang, Y.; Lu, Y.; Chen, X.; et al. Macrophage-Membrane-Coated Nanoparticles for Tumor-Targeted Chemotherapy. *Nano Lett.* **2018**, *18* (3), 1908–1915.

Zhou, H.; Li, X.; Lemoff, A.; Zhang, B.; Yan, B. Structural Confirmation and Quantification of Individual Ligands from the Surface of Multi-Functionalized Gold Nanoparticles. *Analyst* **2010**, *135* (6), 1210.

Zhu, Z. J.; Carboni, R.; Quercio, M. J.; Yan, B.; Miranda, O. R.; Anderton, D. L.; Arcaro, K. F.; Rotello, V. M.; Vachet, R. W. Surface Properties Dictate Uptake, Distribution, Excretion, and Toxicity of Nanoparticles in Fish. *Small* **2010**, *6* (20), 2261–2265.

Zhu, Z. J.; Ghosh, P. S.; Miranda, O. R.; Vachet, R. W.; Rotello, V. M. Multiplexed Screening of Cellular Uptake of Gold Nanoparticles Using Laser Desorption/Ionization Mass Spectrometry. *J. Am. Chem. Soc.* **2008**, *130* (43), 14139–14143.

Zhu, Z. J.; Rotello, V. M.; Vachet, R. W. Engineered Nanoparticle Surfaces for Improved Mass Spectrometric Analyses. *Analyst* **2009**, *134* (11), 2183–2188.

Zhu, Z. J.; Tang, R.; Yeh, Y. C.; Miranda, O. R.; Rotello, V. M.; Vachet, R. W. Determination of the Intracellular Stability of Gold Nanoparticle Monolayers Using Mass Spectrometry. *Anal. Chem.* **2012**, *84* (10), 4321–4326.

Zhu, Z. J.; Tang, R.; Yeh, Y.-C.; Miranda, O. R.; Rotello, V. M.; Vachet, R. W. Determination of the Intracellular Stability of Gold Nanoparticle Monolayers Using Mass Spectrometry. *Anal. Chem.* **2012**, *84* (10), 4321–4326.

Zhu, Z. J.; Wang, H.; Yan, B.; Zheng, H.; Jiang, Y.; Miranda, O. R.; Rotello, V. M.; Xing, B.; Vachet, R. W. Effect of Surface Charge on the Uptake and Distribution of Gold Nanoparticles in Four Plant Species. *Environ. Sci. Technol.* **2012**, *46* (22), 12391–12398.

Zhu, Z. J.; Yeh, Y.-C.; Tang, R.; Yan, B.; Tamayo, J.; Vachet, R. W.; Rotello, V. M. Stability of Quantum Dots in Live Cells. *Nat. Chem.* **2011**, *3* (12), 963–968.